Investigating atmospheric blocking in a series of downscaling experiments with the regional climate model WRF ARW

Master's Thesis

Faculty of Science
University of Bern

Presented by
Daniel Regenass
2017

Supervisor:
Prof. Dr. Christoph C. Raible

Climate and Environmental Physics
and Oeschger Centre for Climate Change Research
University of Bern

In this thesis, the underestimation of atmospheric blocking in the European Atlantic sector in the Community Earth System Model is quantified and potential causes are systematically addressed with a new downscaling approach. To this end, the regional climate model WRF ARW is driven over a large domain covering the North American continent, the North Atlantic and Europe. The two-way nesting capability of WRF ARW is used to systematically enhance horizontal resolution over the North American coast and over the Rocky mountains, as these regions play an important role for blocking formation. Furthermore, one experiment is driven with ERA-Interim sea surface temperature fields in the lower boundaries. It is found that CESM underestimates atmospheric blocking in the mid-latitudes, whereas blocking frequencies north of 65-70° N are found to be too high. Evidence from other meteorological fields further points towards a too zonal behavior of the mean flow in CESM. Increasing horizontal resolution over the aforementioned key areas is found to alter the mid-latitude dynamics with associated impacts on blocking frequencies. Even more realistic blocking frequencies are obtained, when replacing CESM sea surface temperature fields with corresponding ERA-Interim fields in the lower boundaries, leading to the conclusion that blocking frequencies in the European Atlantic sector are to a considerable part steered by the state of the Northern Atlantic and more specifically by processes associated with energy exchange between ocean and atmosphere.

Contents

1. Introduction **1**

1.1. Linkages between atmospheric blocking and climate . . . 1
1.2. Atmospheric blocking in climate models . . . 2
1.3. Aim of this thesis . . . 2

2. Theoretical background **5**

2.1. Phenomenology . . . 5
2.2. Meteorological fields and blocking indices . . . 6
2.2.1. Indices based on the geopotential height field . . . 6
2.2.2. Potential vorticity . . . 7
2.2.3. Physical mechanisms for blocking formation . . . 9
2.2.4. Low wavenumber Rossby waves . . . 11
2.2.5. Baroclinic instability . . . 11
2.3. Recent research on the importance of horizontal model resolution for blocking formation 12

3. Climate models and experimental design **15**

3.1. The Community Earth System Model (CESM) v. 1.0.1 . . . 15
3.2. Weather Research and Forecasting Model (WRF ARW) v3.8 . . . 17
3.2.1. Introduction and purpose . . . 17
3.2.2. Preprocessing and model chain . . . 17
3.2.3. Dynamical core . . . 18
3.2.4. Map projections . . . 20
3.2.5. Physics and parameterizations . . . 20
3.2.6. Domain boundaries and nesting . . . 22
3.2.7. Two-way nesting . . . 23
3.2.8. Nudging . . . 23
3.3. ERA-Interim reanalysis data . . . 24
3.4. Experimental design . . . 24
3.4.1. General design for all experiments and work flow . . . 24
3.4.2. Domain properties . . . 25
3.4.3. Description and motivation of the different experiments . . . 26

4. Methods **31**

4.1. Expanded Tibaldi Molteni blocking index . . . 31
4.2. Lagrangian anticyclone tracking . . . 31

4.3. Latitude of the low level jet . . . 33
4.4. Principal component analysis . . . 34

5. Results and discussion **37**
5.1. Blocking frequencies . . . 37
5.1.1. ERA-Interim, CESM and unnested WRF runs: A first comparison . . . 37
5.1.2. The impact of enhanced resolution . . . 41
5.1.3. The impact of model SST biases . . . 42
5.1.4. Blocking properties . . . 43
5.2. Position and strength of the low level jet . . . 46
5.2.1. Jet position in CESM and unnested runs . . . 46
5.2.2. Jet position in selected setups . . . 47
5.3. Climatology and principal components for the time varying SST simulations . . . 51
5.4. Mechanisms for blocking formation in ERASSTtVar . . . 55
5.4.1. Composite analysis . . . 55
5.4.2. Case study of a blocking event . . . 58
5.5. Baroclinicity for different setups . . . 60

6. Summary and Conclusions **63**

7. Outlook **67**

A. WRF best practice **69**
A.1. Compilation on UBELIX . . . 69
A.2. Hints for WPS . . . 69
A.3. Troubles arising in real . . . 70
A.4. Running WRF . . . 70
A.5. Postprocessing . . . 71

B. Example WPS and WRF namelists **73**
B.1. WPS namelist . . . 73
B.2. WRF namelist . . . 74

List of Figures **79**

References **83**

WRF Weather Research and Forecasting Model

CESM Community Earth System Model

SST Sea Surface Temperature

PCA Principal Component Analysis

SLP Sea Level Pressure

NoN Unnested Simulation with 36 vertical levels and constant SST.

NoNVertPlus Unnested Simulation with 46 vertical levels and time-varying SST.

CoastN As NoN, but with nest over the American East Coast.

CoastNtVar As NoNVertPlus, but with nest over the American East Coast.

RockyN As NoN, but with nest over the Rocky Mountains.

BothN As NoN, but with nests over Rockies and the American east Coast.

ERASSTtVar As NoNVertPlus, but with SST input from ERA-Interim data.

ERA-Interim Reanalysis data (1979-2016) provided by the European Consortium for Medium Range Weather Forecasting.

LAGTRACK (Anti-) Cyclone tracking algorithm.

TIMO Extended (2D) Tibaldi-Molteni index.

PV Potential Vorticity

PVT Potential Vorticity Tendency

NAO North Atlantic Oscillation

1. Introduction

Atmospheric blocking -or short blocking- is a frequently found weather pattern in many regions of the Earth. In Europe, blocking events often cause extreme weather situations [*Buehler et al.*, 2011; *Pfahl and Wernli*, 2012]. During summer season, blockings cause heat waves by preventing atmospheric masses from mixing and thus exhibiting them to clear sky conditions and continental heating. Abnormally hot summers, such as in 2003 and 2015, are associated with summer blockings [*Grazzini, Frederico*, 2003]. Such events are problematic to the public, as dry regions become short of water and mortality rates increase [*Kovats et al.*, 2004].

During winter, the effects of blockings are somewhat adverse. Cold air is advected at the north-eastern border of the blocking, bringing cold continental air masses to central Europe. This results in cold and dry conditions and even cold spells [*Buehler et al.*, 2011], which are again problematic for the densely populated countries of central Europe, as they may cause crop damages and increase mortality rates [*Wang et al.*, 2016]. Moreover, the stable high pressure conditions in the lower troposphere often cause a temperature inversion in the planetary boundary layer and hence hinder the exchange of air masses between the boundary layer and the free troposphere. This is particularly problematic as it has adverse health effects due to high concentrations of atmospheric pollutants in valleys and densely populated areas [*Vardoulakis and Kassomenos*, 2008; *Largeron and Staquet*, 2016].

1.1. Linkages between atmospheric blocking and climate

In the European Atlantic sector, long lasting ($>$ 10 days) atmospheric blocking events have been shown to be related to a negative phase of the Northern Atlantic Oscillation (NAO) [*Quadrelli et al.*, 2001; *Barriopedro et al.*, 2006]. The negative phase of the NAO is associated with weaker pressure gradients between the Iceland low and the Azores high. For shorter blocking events this relationship cannot be established, pointing towards a relation between the duration of blocking events and the phase of the NAO [*Trenberth et al.*, 2007; *Schwierz et al.*, 2004; *Scherrer et al.*, 2006].

No long-term trend is evident in the northern hemisphere blocking intensity [*Wiedenmann et al.*, 2002]. While *Barriopedro et al.* [2006] found significant decreases in events and days, *Davini et al.* [2012] found a significant increase in mid-latitude blocking in the European Atlantic sector in the sixty year period covered by the NCEP-NCAR reanalysis. Note that *Davini et al.* [2012] distinguished between mid-latitude blocking and blocking in the polar regions, whereas *Barriopedro et al.* [2006] considered overall blocking frequencies in the European Atlantic sector. The former approach thereby has a closer connection to mid-latitude dynamics and the associated impacts in Central Europe.

Global surface air temperature has risen by 0.78 to 0.85° C when comparing the period 1850 -1900 a.D. to 2002 - 2012 a.D. [*Collins et al.*, 2013] and the projected rise for the 21st century is likely to fall in the range between 1.1° C and 2.6° C even for the relatively moderate RCP 4.5 pathway [*Collins et al.*, 2013]. Given the magnitude of the global temperature increase, it is clear that ongoing global warming will also affect the planetary-scale circulation. Indeed, a poleward shifts of the mid-latitude jet of 1-2 degrees by the end of the 21st century is likely under the high emission RCP 8.5 scenario [*Collins et al.*, 2013]. For lower emission scenarios, the signal is not as clear as a global increase in zonal wind speed is concurred by thermal forcing of the Arctic amplification [*Collins et al.*, 2013]. A shift in jet latitude would of course also induce a shift in the spatial distribution of blocking frequencies.

In the study of *Matsueda et al.* [2009] a decrease in blocking frequency for the European Atlantic sector was projected for the 21st century, however with reservations as their models revealed shortcomings in reproducing the present-day state for this sector. A more recent study by *Masato et al.* [2014] found a slight increase in Atlantic blocking in the 21st century under a high emission scenario, while blocking frequencies over Europe remain relatively stable. Clearly, more research on this subject is to be expected, once climate models accurately capture the present day state of atmospheric blocking.

1.2. Atmospheric blocking in climate models

The high impacts associated with blocking events highlight the importance of accurate projections for blocking events in a changing climate. However, to this day climate models do not accurately capture atmospheric blocking in the European Atlantic sector. In fact, the underrepresentation of atmospheric blocking in climate models is a long standing problem in atmospheric modeling [*Randall et al.*, 2007; *D'Andrea et al.*, 1998; *Pelly and Hoskins*, 2003]. After almost 20 years of research, neither the phenomenon nor its underrepresentation in climate models are fully understood [*Matsueda et al.*, 2009; *Masato et al.*, 2013; *Davini and D'Andrea*, 2016]. Given the high impacts on society, the atmospheric dynamics community still thrives toward a better representation of atmospheric blocking in climate models.

1.3. Aim of this thesis

This thesis aims at systematically track down potential sources for the underrepresentation of atmospheric blocking in the Community Earth System Model (CESM) v. 1.0.1, a state of the art global climate model. The influence of horizontal resolution and representation of sea surface temperature fields are thereby in the scope of the analyses.

The thesis is organized as follows: The theoretical background for this work is set in chapter 2. This includes the definition of atmospheric blocking in a qualitative and quantitative way, the discussion of blocking indices and relevant meteorological fields as well as a short overview on the current state of research. Then the models and analysis tools used during the course of this work are explained in

chapters 3 and 4. Results and discussion are presented in chapter 5. Finally, the work is summarized in chapter 6 and we will also give a short outlook as to where further research on this topic could be directed in chapter 7.

2. Theoretical background

2.1. Phenomenology

Atmospheric blocking is defined as a full or partial interruption of the predominant westerly flow in the mid-latitudes [*American Meteorological Society*, 2017]. The westerly flow in the troposphere is thereby either shifted from its preferred position, or depending on the definition of the phenomenon, even split into two branches [*Rex*, 1950].

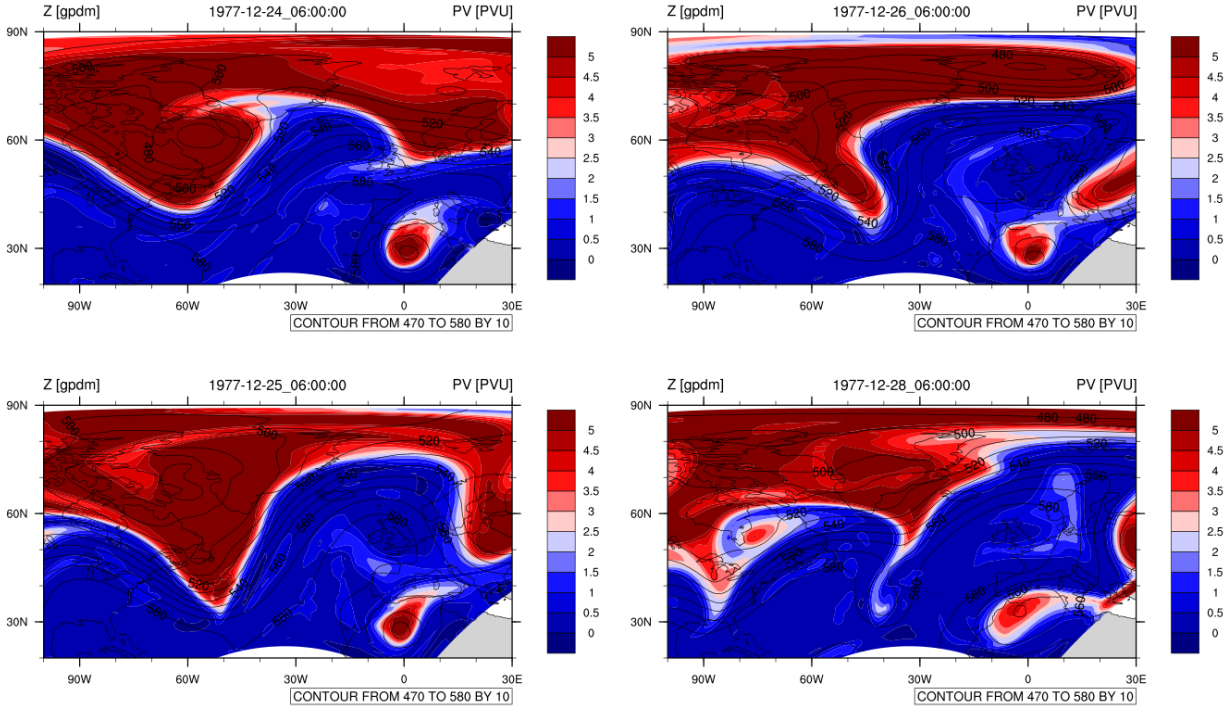

Figure 2.1.: *Blocking event as found in a simulation for late December 1977. Potential vorticity (blue and red) and geopotential height (contours) on the 500 hPa isobaric surface. The anticyclonic flow regime is eminent in both fields. After its buildup, the center of the blocking is located over the British Isles.*

This flow regime can be seen in different meteorological fields, some are discussed in section 2.2. In common weather charts, blocking events are identified as stable, quasi-stationary high pressure systems. Even though blockings are well-known to meteorologists, coming up with a more quantitative description is still subject of ongoing research [*Pelly and Hoskins*, 2003; *Schwierz et al.*, 2004; *Scherrer et al.*, 2006].

2.2. Meteorological fields and blocking indices

For two reasons, it is evident that a more quantitative description of blocking events is required:

- An exact definition of blocking events facilitates the comparison of blocking frequencies amongst different models, time periods, etc. This is not possible, if the counting depends on more subjective criteria.
- A quantitative description may be written as an algorithm. Blockings may then efficiently be counted, even in very large datasets.

Subsequently, some of the most important blocking indices and their advantages and disadvantages are discussed. Two classes of indices are distinguished, one class is based on the geopotential height field, the other on potential vorticity. We will briefly introduce geopotential height and potential vorticity. A more in depth discussion is found in the textbooks on dynamic meteorology, e.g. [*Holton and Hakim*, 2012].

2.2.1. Indices based on the geopotential height field

The geopotential $\Phi(z)$ is the gravitational potential of earth's gravity field with acceleration $g(z)$ at height z, given by

$$\Phi(z) = \int_0^z g(z')\, dz'. \tag{2.1}$$

We retrieve the geopotential height as $z_{GP} = \Phi(z)/g_0$, where $g_0 = 9.81 m/s^2$ is the mean gravitational acceleration on earth's surface. Note, that $g(z)$ also depends on latitude as the centrifugal acceleration arising from earth's rotation is often included in $g(z)$. This effect is strongest at the equator and exactly zero at the poles. Furthermore, earth is not a perfect sphere, but corresponding effects in the gravitational field are typically neglected.

In meteorology, the geopotential height is typically given on pressure surfaces. As cold air is denser than warm air, isobaric surfaces lie closer together in cold air and further apart in warm air. On a pressure surface, z_{GP} is higher in regions of warm air, than in regions of cold air. Similarly, z_{GP} lies higher above a high pressure system and lower above a low pressure system. The 500 hPa pressure surface is located in the mid-troposphere at roughly $5,5$ km altitude. The geopotential height on the 500 hPa pressure surface (z_{500} hereafter) is to some extent free from micro- and mesoscale disturbances found closer to the surface and therefore better suited to investigate planetary-scale phenomena such as blockings and the propagation of troughs and ridges.

Early efforts to quantify atmospheric blocking date back to the 1980s [*Lejenäs and Økland*, 1983]. An index still widely used in different variations was introduced by *Tibaldi and Molteni* [1990]. It is based on north- and southward gradients of z_{500}. The main idea of this one-dimensional index is that a blocking always inverts the southward gradient $GHGS$ of z_{500}, which is negative under normal (not blocked) conditions. To ensure, that the center of the block is located close to a previously defined latitude (60° north in the original publication), also the northward gradient $GHGN$ must

be positive. Together the criteria read:

$$GHGS > 0 \frac{\text{gpm}}{^\circ\text{lat}}, \quad GHGN > 10 \frac{\text{gpm}}{^\circ\text{lat}}, \tag{2.2}$$

where the gradient is simply calculated as difference between z_{500} at the central latitude and two points $\pm 20^\circ$ south and north relative to the central latitude. A given longitude is defined as blocked at time t, if both of the above conditions are satisfied. The conditions are slightly relaxed to make the algorithm less sensitive to local effects. This correction is not presented here, as it is not of great importance to the general idea of the algorithm. *Scherrer et al.* [2006] extended this idea to a two-dimensional index, which we present in section 4.1.

This family of two-dimensional indices based on geopotential height gradients uses simple algorithms that run fast and that are easy to program. On the downside, these indices do not contain any further physical informations on the systems they identify as blockings.

Another idea based on gradients of z_{500} is the Lagrangian Tracking (LAGTRACK) method introduced by *Blender et al.* [1997], originally to track cyclones (depressions in geopotential height fields). It has been adapted to track high pressure systems by *Buehler* [2008]. In short, the algorithm searches for maxima in z_{500} and then checks if thresholds in the two-dimensional gradient ∇z_{500} are exceeded. It then tracks an anticyclone over time, until the thresholds are no longer exceeded. Although the algorithm is somewhat complicated, the advantage of this blocking index is the retrieval of information on the track as well as on the temporal evolution of an anticyclone. This information may then be used for further analyses. A more in depth discussion of algorithm is found in section 4.2.

2.2.2. Potential vorticity

Conservation of angular momentum is a fundamental concept in physics. By introducing vorticity, it is possible to extend this concept to a fluid rather than an accumulation of mass points. The most important quantities and concepts will be introduced in this section. For a more in-depth discussion, the reader is again referred to *Holton and Hakim* [2012]. A fluid's relative vorticity in a moving coordinate system is defined as the curl of the three-dimensional velocity field.

$$RV = \nabla \times \vec{v_3} \tag{2.3}$$

In atmospheric dynamics, two-dimensional rotations are often of greatest interest and therefore relative vorticity ζ is often referred to as the third component of the above expression:

$$\zeta = \frac{\partial v}{\partial x} - \frac{\partial u}{\partial y}. \tag{2.4}$$

As this is only the vorticity on a co-rotating coordinate system on earth, to get the absolute vorticity η, earth's rotation must be considered, resulting in $\eta = \zeta + f$, where f is the Coriolis parameter. Similar to potential temperature, potential vorticity (PV) can be introduced as the absolute vorticity

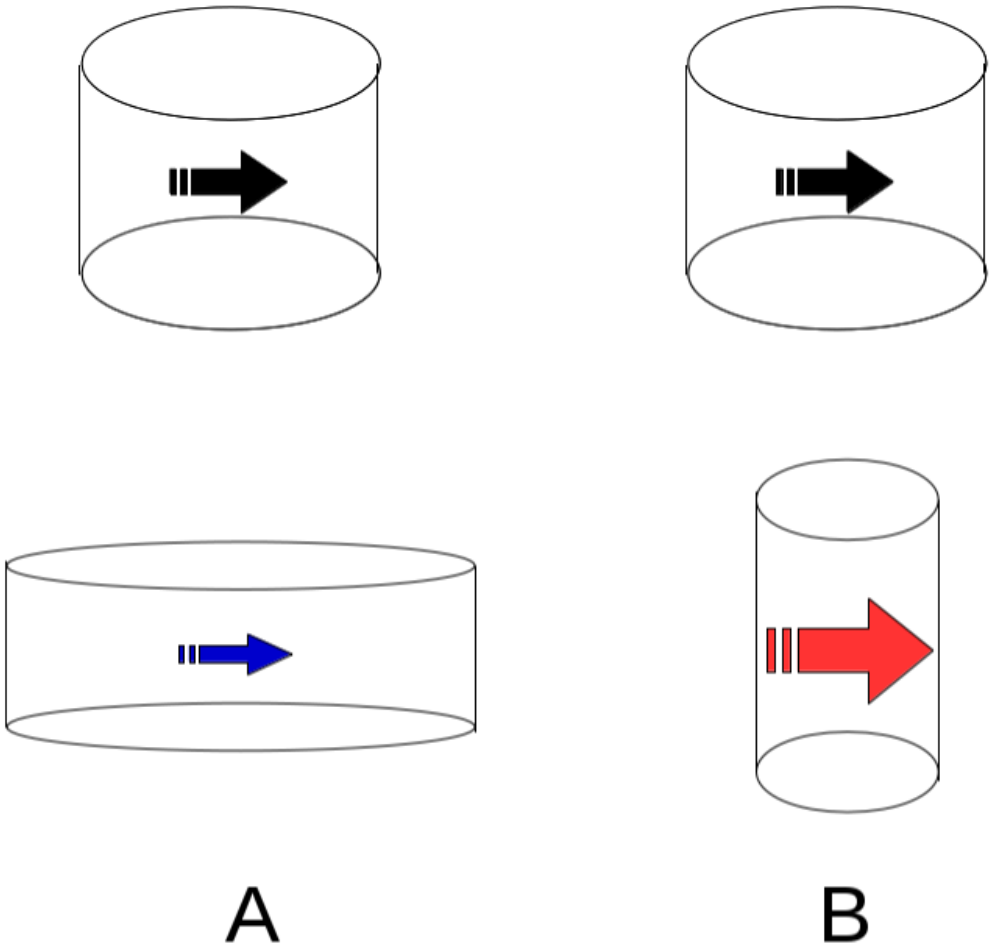

Figure 2.2.: *Effect of stretching and shrinking of air parcels on relative vorticity. Potential vorticity is conserved for both cases.*

an air parcel carries normalized to its vertical extent. This concept may be illustrated with a short thought experiment (Fig. 2.2).

Consider two identical air parcels (A, B) at the same latitude with the same vertical extent. Suppose both of them rotate counterclockwise with the same velocity at the beginning of the experiment, implying that they carry a positive relative vorticity ζ. Now we vertically shrink parcel A, while we stretch parcel B. As we did not impose torque on either of the two parcels, total angular momentum must be conserved. This in turn implies that the rotation of parcel A must decelerate, or in other words, the relative vorticity decreases. Consequently the opposite is true for parcel B. Meanwhile, the PV of parcel A and B remains the same, as the expression in the last bracket of the subsequent equation takes this stretching and shrinking of air parcels into account. In analogy to potential temperature θ, PV is a conserved quantity on isentropic surfaces, hence under adiabatic conditions, we can write

$$\frac{D}{Dt}\left[(\zeta + f)\left(\frac{\partial\theta}{\partial p}\right)\right] = 0, \tag{2.5}$$

where D/Dt is the total time derivative, θ is the potential temperature and p is pressure. It is clear that PV can only be generated or destroyed by diabatic heating and cooling. On the northern hemisphere, planetary scale high pressure systems are associated with low (even negative) PV anomalies, while low pressure systems are associated with high PV anomalies. For convenience, potential vorticity is often displayed in potential vorticity units (PVU), where 1 PVU $= \frac{10^{-6}\mathrm{Km}^2}{\mathrm{kgs}}$. It is possible to attribute the contributions of advection and differential heating to PV tendency ($\partial PV/\partial t$). We can thus determine the major mechanisms responsible for a given PV anomaly with the PV tendency equation. For hybrid σ coordinates (as used in WRF 3), the PV tendency equation reads,

$$\frac{\partial PV}{\partial t} = \underbrace{u\frac{\partial PV}{\partial x} + v\frac{\partial PV}{\partial x}}_{\mathrm{HA}} + \underbrace{\dot{\sigma}\frac{\partial PV}{\partial \sigma}}_{\mathrm{VA}} + \underbrace{\frac{g}{p_s}\left[-(\zeta+f)\frac{\partial \dot{\theta}}{\partial \sigma} - \frac{\partial u}{\partial \sigma}\frac{\partial \dot{\theta}}{\partial y} + \frac{\partial v}{\partial \sigma}\frac{\partial \dot{\theta}}{\partial x}\right]}_{\mathrm{DH}}, \tag{2.6}$$

where u,v and $\dot{\sigma}$ are the two horizontal and the vertical velocity respectively, $\dot{\theta} = \partial\theta/\partial t$ is the rate of change of potential temperature, g is gravitational acceleration and p_s is surface pressure. Note, that the different parts of the equation are labeled with under braces. HA and VA are the horizontal and vertical advection terms, respectively and DH is the differential heating term.

In the zonal mean, PV increases with latitude as the Coriolis parameter f and $-\frac{\partial\theta}{\partial p}$ increase. Furthermore, PV increases quite rapidly around the tropopause as the temperature gradient gets inverted. It is therefore possible to identify the tropopause as region, where PV increases rapidly. Since the northern hemisphere troposphere has typical PV values between 0 and 1, the dynamical tropopause is often introduced as the 2 PVU line. The distribution of PV (and hence the position of the dynamical tropopause) is best seen on upper-level isentropic surfaces. Popular choices for isentropic surfaces range from $\theta = 310$ K to $\theta = 325$ K. As we investigate the extended winter season, the dynamical tropopause is referred to as the 2 PVU line on the $\theta = 315$ K surface in this study.

A family of blocking indices is based on the folding of θ on the dynamical tropopause (2 PVU surface). The first blocking index was introduced by *Pelly and Hoskins* [2003] and a review and comparison to indices based on geopotential height gradients can be found in *Scherrer et al.* [2006]. In the aforementioned publications, it is argued that the characteristics of the flow and the large scale weather patterns are generally better visible using the PV-θ framework. However, LAGTRACK tracks anticyclones on geopotential height fields, so we use the classical Tibaldi-Molteni 4.1 index based on geopotential height as a second blocking index, as we expect the two indices to yield more similar results.

2.2.3. Physical mechanisms for blocking formation

From a theoretical point of view, the (nonlinear) interaction of waves with different wave numbers is often identified as a key element for blocking formation [*Egger*, 1978; *Benzi et al.*, 1986] and more recently also [*Christensen and Wiin-Nielsen*, 1996; *Luo*, 2005]. While these models can explain

the importance of wave-wave interaction, they cannot identify an intuitive mechanism for this interaction.

Only recently, diabatic heating is identified as an important contributor to blocking formation, even though it was speculated to play a major role from early on [*Egger*, 1978]. *Pfahl et al.* [2015] showed, that indeed 60 to 70% of air masses entering a European blocking system were subject to latent heating within a time span of seven days prior to their arrival in the system. A very recent study by *O'Reilly et al.* [2016] identifies the importance of sharp sea surface temperature gradients around the gulf stream as a key contributor to European blocking. The authors compare simulations with high resolution SST fields to smoothed SST fields, where the temperature gradients are not as sharp and find a significant drop in blocking frequency in the latter.

A very interesting point is raised in a numerical experiment carried out by *Walter et al.* [2001]. They use a simplified atmospheric model running on a flat and homogeneous earth (i.e. no land masses and oceans) and place static hot/cold monopoles in the mid-latitudes. The sheer existence of such hot/cold spots is sufficient to produce blocking-like structures.

The vertical extent of European blocking typically reaches up to the tropopause. When considering vertical cross sections, the dynamical tropopause is lifted, while on isentropic surfaces shifted northward. Thereby cut-off structures and anticyclonal wave-breaking are often found as typical features in the tropopause [*Weijenborg et al.*, 2012]. As such structures can only appear, when low PV air enters the upper tropopause/ troposphere region, this raises the question as to where these air masses originate. Different authors have already pointed out the simultaneous appearance of an upstream cyclone associated with an European blocking event, see e.g. *Altenhoff et al.* [2008].

A possible mechanism is the transport of lower level air to the upper troposphere with warm conveyor belts. Warm conveyor belts are triggered at the cold front of an extratropical cyclone. Warm and moist air masses from the warm sector slip upward along the cold front, where they form convective clouds and usually cause heavy precipitation. Obviously these air masses are subject to latent heating during this process, this heating is sufficient to further promote their ascent to the upper troposphere, where they continue their journey westward and hence influence the downstream circulation [*Eckhardt et al.*, 2004]. It might seem counterintuitive that air masses originating at the heart of cyclones contribute to low PV air in the upper troposphere. However, these air masses are advected at very low levels and completely dry out on their journey to the upper troposphere. This mechanism seems plausible to at least explain the amplification of standing ridges. Furthermore we can identify a positive feedback mechanism, as an already existing blocking event slows down westward traveling cyclones and pushes them north- or southward. During their journey around the block, they can push additional air masses to the upper troposphere in the blocking region. If this mechanism is found to be true, the model's ability to correctly represent the occurrence of deep convection in extratropical cyclones would also play a key role in the model's ability to correctly reproduce European blocking.

Two major drivers for blocking formation may be derived from the theory of atmospheric dynamics

and from recent literature. The first one is the formation of stationary (or even eastward traveling) Rossby waves with very low wavenumbers ($k = 1, 2, 3$) along the planetary front. The second one is the activity of synoptic scale disturbances, which may interact with stationary and quasi-stationary waves. It should be stressed that the relative contribution of the two is still under discussion.

2.2.4. Low wavenumber Rossby waves

In their most general form, Rossby waves [*Rossby*, 1940] may be seen as potential vorticity conserving motions. The existence of a mean isentropic PV gradient acts as a restoring force for any meridional displacement of an air parcel. Hence, any meridional displacement of air masses will result in wave motion [*Holton and Hakim*, 2012].

A little more intuitive is the consideration of a strictly barotropic atmosphere with constant height. These two simplifications are justified when qualitatively discussing planetary-scale wave activity in the mid-latitudes. In such an atmosphere, absolute vorticity $\eta = \zeta + f$ is conserved. When displacing an air parcel southward (northward), the Coriolis parameter f decreases (increases) and hence relative vorticity ζ must increase (decrease). This will induce a counterclockwise (clockwise) rotation of the air parcel and thus push the air parcel back towards its original position. In this case, the conservation of absolute vorticity acts as a restoring force on the meridional displacement of air parcels.

Using linear perturbation theory, one can show that free Rossby waves travel westward relative to the mean wind speed $\bar{u}$. For mid-latitude cyclones the difference between phase velocity and mean wind speed $c - \bar{u}$ is approximately -8 m/s, therefore cyclones travel eastward, but slower than the mean flow. By equating $c = \bar{u}$ and solving the dispersion relation of free Rossby waves for the wavenumber k, it is possible to find a critical wavenumber k_s, for which free Rossby waves become stationary. Free Rossby waves with zonal wave numbers smaller than the critical wavenumber k_s travel westward. Such stationary or quasi-stationary Rossby waves can then interact with synoptic scale eastward traveling waves [*Eady*, 1949].

By adding an orographic forcing term to the barotropic Rossby wave equation, *Charney and Eliassen* [1949] showed that the stationary wave pattern in the 500 hPa geopotential height field can almost completely be explained by orographically forced Rossby waves. On the northern hemisphere, the Rockies and the Himalayas are the two main North - South barriers in the mid-latitudes. The position of these mountain ranges is therefore the key factor for the mean distribution of the 500 hPa geopotential height field.

2.2.5. Baroclinic instability

In the view presented above (see section 2.2.3), the contribution of synoptic scale disturbances to blocking formation arises most likely from the interaction of eastward migrating cyclones with low wavenumber Rossby waves. A mathematical framework to estimate the growth of cyclones was derived by *Eady* [1949]. In this framework, cyclones are considered unstable modes in the atmosphere, which may be subject to exponential growth. *Eady* [1949] showed that all waves with

a wavelength greater than 3500 km are unstable, with maximal instability at wavelengths around 5500 km.

Furthermore, it is possible to derive a growth factor for the most unstable wave, which is given by

$$\sigma_{BI} = 0.31 \frac{f}{N} \frac{\partial |v|}{\partial p} = 0.31 \frac{1}{T} \left(\frac{1}{g\theta} \frac{\partial \theta}{\partial z} \right) |\nabla T| \,, \tag{2.7}$$

where f is the Coriolis parameter, N the Brunt Väisällä frequency, $|v|$ horizontal wind speed, p pressure, T and θ temperature and potential temperature respectively and g mean gravitational acceleration on earth's surface [*Lindzen and Farrell*, 1980]. Essentially this measure contains two factors which may contribute to instability: The first one is atmosphere's "stiffness" or more accurately its vertical stratification, described by the Brunt Väisällä frequency. The smaller N is, the weaker is the restoring force acting on a vertically displaced air parcel. For any $N \leq 0$, the air parcel will not return to its original state, which means that a present disturbance can grow freely. The second contributor is the horizontal temperature gradient ∇T. The stronger it is, the more energy is available for horizontal advection of air masses.

The Eady growth rate is an intuitive measure of the atmosphere's baroclinic instability. For cyclones traveling through the European Atlantic sector, the major region for cyclogenesis is located along the coastal regions of North America in the mid-latitudes [*Miller*, 1946].

2.3. Recent research on the importance of horizontal model resolution for blocking formation

As introduced in chapter 1, atmospheric blocking is underestimated in most climate models and the underlying mechanisms for this bias are not fully understood. Given the above picture, in which the wave-wave interaction between low wavenumber Rossby waves and cyclones is identified as key element for blocking formation, it should be evident that model resolution plays an important role in the correct representation of atmospheric blocking. Neither orographic forcing nor zones of cyclogenesis will be captured correctly, if the resolution of the model is too low.

Despite increasing model resolution over the last two decades, GCMs still severely underestimate blocking frequencies [*Davini and D'Andrea*, 2016]. Moreover, while higher model resolution is expected to enhance blocking frequencies from a theoretical point of view, two studies [*Scaife et al.*, 2010, 2011] seem to negate a simple relation between resolution and blocking frequency. In the more controversial follow-up article, *Scaife et al.* [2011] showed that low blocking frequencies may at least partially be attributed to erroneous model mean states. Furthermore, they showed that the blocking frequency was enhanced when replacing the model mean state with an actual climatology of the same period. They concluded that not low resolution, but biases in the model mean states are the crucial source of error in this matter. This view is in turn challenged by a more recent study of *Berckmans et al.* [2013], where selectively increasing horizontal resolution over complex topography seemed to improve blocking frequency. There is no conclusive argument, but when

designing this study, we argue that model resolution will also affect the model mean state and not just the short-termed fluctuations, a point that might be somewhat overlooked in *Scaife et al.* [2011].

3. Climate models and experimental design

Climate models are in essence a simplified mathematical representation of the climate system or of its subsystems. With both scientific advance in the field and continuously increasing computer power, climate models have become an essential tool for the research community. The complexity of climate models ranges from relatively simple point and box models to today's fully coupled global climate models (GCMs), which include modules for atmosphere, ocean and land surface. Almost all climate models are based on sets of equations that are too complicated to solve analytically, so that the calculations are done on discretized space and time using sophisticated numerical methods.

The coupling of individual parts of the climate change is a particularly difficult task, because time and length scales of subsystems may differ by several orders of magnitude. It is apparent, that a global, fully coupled model including all parts of the climate system requires a tremendous computational effort. The effort scales nonlinearly with the resolution of the model, making the trade-off between reasonable resolution and affordable computational effort a central problem in climate modeling.

In this thesis, two different types of climate models are used. CESM is a global climate model and we use the output of a fully coupled model simulation. WRF ARW is a regional climate model, which we will use to investigate areas of interest with a significantly higher resolution. A description of both models can be found in sections 3.1 and 3.2.

3.1. The Community Earth System Model (CESM) v. 1.0.1

CESM 1 was developed at the National Center for Atmospheric Research (NCAR) in Boulder Colorado and first released in 2010 [*Hurrell et al.*, 2013]. It is a comprehensive model, containing modules for atmosphere, ocean, land, sea ice and land ice. The model is quite flexible in its usage, as the user is free to choose, which modules to include and couple.

For this study, we use a transient simulation from 850 to 2100 AD ran by *Lehner et al.* [2015]. In this study, CESM version 1.0.1, with a horizontal resolution of $1.25° \times 0.9°$ in the atmosphere and land components is used. The simulation features fully coupled modules for atmosphere, ocean, land and sea ice as well as an interactive carbon cycle.

CESM's atmosphere component is CAM4, the Community Atmosphere Model running on a finite volume core with 26 vertical levels on hybrid σ coordinates reaching up to the mid-stratosphere at 3.545 hPa [*Neale*, 2010]. The model's ocean component is the Parallel Ocean Program version 2 (POP2) with 60 depth levels [*Smith et al.*, 2010]. The horizontal resolution varies and is higher at the equator and around the model's north pole located in Greenland. The nominal horizontal

resolution is $1° \times 1°$. The Community Sea Ice Code version 4 (CICE 4) [*Bailey et al.*, 2011] runs on the same horizontal resolution as POP2, but it contains a subgrid-scale ice thickness distribution. The model also includes the Community Land Module version 4 (CLM4) [*Lawrence et al.*, 2011] with prognostic carbon and nitrogen cycles.

The transient CESM simulation used in this study features reconstructions of total solar irradiance by *Vieira and Solanki* [2010] and *Lean et al.* [2005], greenhouse gas forcing as used in the Paleo Model Intercomparison Project 3 (PMIP3) protocol [*Schmidt et al.*, 2011] and a volcanic forcing time series by *Gao et al.* [2008]. For more details, the reader is again referred to *Lehner et al.* [2015].

The simulation was extensively used to find the imprints of forced and internal variability in the climate system [*Lehner et al.*, 2015]. More recently, Sandro Blumer and Christoph Raible investigated extreme events in the atmospheric component of the model (personal conversation with Sandro Blumer, January 2016). Their findings reveal an almost complete lack of blocking events in the Euro-Atlantic sector. Similar problems were already reported for one of its precursors, CCSM 2.0.1 by *Buehler et al.* [2011]. It is worthwhile to note that the resolution increased from $3.6° \times 1.8°$ in CCSM 2.0.1 to $1.25° \times 0.9°$ in CESM 1.0.1 while the more recent model still does not show an improved blocking frequency. This might indicate either threshold effects in horizontal resolution and/ or one could argue that horizontal resolution in the atmosphere model alone is not the critical quantity to simulate realistic blocking frequencies.

3.2. Weather Research and Forecasting Model (WRF ARW) v3.8

3.2.1. Introduction and purpose

WRF is an open source tool for meteorological research and numerical weather forecasting [*Skamarock et al.*, 2008]. In its Non-hydrostatic mesoscale model (NMM) version it is used as an operational weather forecasting model by the US governmental weather services such as the US National Center for Environmental Prediction (NCEP) and by private weather services.

In the academia the Advanced Research WRF ARW core is widely used for a number of reasons:

- The open source code allows for adaptations suited for a given research question.
- The large global community and community support.
- Although originally designed as a mesoscale forecasting model, WRF ARW is rather flexible in its usage and it is possible to resolve large scale $\mathcal{O}(10^2$ km) as well as regional $\mathcal{O}(10^0$ km) processes.
- The implemented two-way nesting is a powerful tool for dynamical downscaling (see section 1.1.1). In short, two-way nesting is the usage of sub domains - called nests - which may differ from their parent domain in resolution and parameterizations. In contrast to one-way nesting, the solution is transported back to the parent domain.

We use version 3.8, which was released in April 2016. In the following sections we describe some of the main features of the model and particularly features that are of importance to the experiments carried out in this study.

3.2.2. Preprocessing and model chain

WRF ARW has a sophisticated preprocessing package, the WRF Preprocessing Program (WPS), which assimilates input data and horizontally interpolates the data to the chosen WRF computational domain. Its main constituents are three programs:

- **Geogrid:** Generates geographical fields for the chosen domains based on data provided by the US National Oceanic and Atmospheric Administration (NOAA). Those fields include e.g. terrain height, landmasks, vegetation cover, etc.
- **Ungrib:** Reads in mandatory (and also additional, if provided) input files in GRIB format and saves them to an intermediate file format, which can then be read by the metgrid program. Mandatory fields are: temperature (3D), horizontal wind speeds (3D), geopotential height (3D), relative humidity (3D), 2-m temperature (2D), 2-m relative humidity (2D), 10-m horizontal wind speeds (2D), skin temperature (2D), surface pressure (2D) and mean sea level pressure (2D).
- **Metgrid:** Horizontally interpolates the fields obtained from geogrid and ungrib to the chosen domains (i.e. to their grid points).

Once WPS ran successfully, the data needs to be interpolated to the chosen WRF ARW vertical levels (eta coordinates, see section 3.2.3). This task is executed by the program **real**, which is not part of the WPS. After this step, the actual WRF ARW model is ready to be executed by the user.

3.2.3. Dynamical core

The ARW solver integrates a set of non-hydrostatic, fully compressible Euler equations using a 3rd order Runge-Kutta scheme. It is possible to run the model using the hydrostatic approximation, which is reasonable when running the model with coarse resolution, as it is the case in our experiments. The full set of equations will not be given here, but the individual prognostic and diagnostic equations are enumerated in the following.

Prognostic equations:

1. Horizontal and vertical momentum conservation equations,
2. mass conservation (continuity) equation,
3. advection equation for potential temperature,
4. advection equation for water mixing ratios,
5. prognostic equation for the geopotential.

Diagnostic equations:

1. Equation of state for moist air,
2. Diagnostic equation for dry inverse density.

If the model runs in hydrostatic mode, the vertical momentum equation simplifies to the hydrostatic approximation.

The equations are formulated using hydrostatic pressure coordinates η following the definition of *Laprise* [1992],

$$\eta := \frac{p - p_{top}}{\mu}, \mu = p_s - p_{top}, \tag{3.1}$$

where p denotes the pressure at the given η level, p_s denotes surface pressure and p_{top} the pressure at the chosen model top. These are terrain following coordinates, which smoothen out towards the top. As it is straightforward to see, η coordinates range from 1 at the surface to 0 at the model top. A sketch of the terrain following η coordinates can be found in Fig. 3.1.

For small grids it would be sufficient, to formulate the prognostic equations on a three dimensional euclidean (flat) grid, however for mesoscale size domains, curvature effects cannot be neglected. In WRF ARW this problem is tackled by introducing map factors. Let Δx and Δy be the horizontal

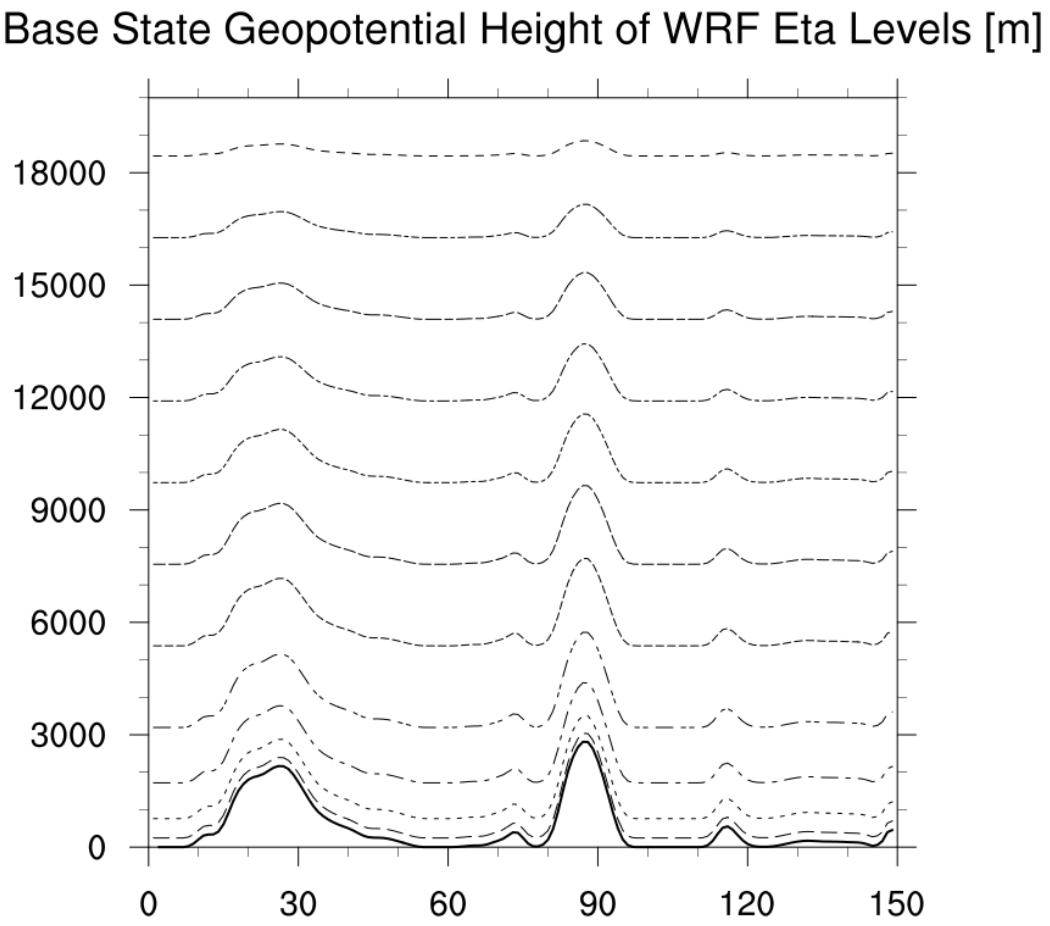

Figure 3.1.: *WRF ARW vertical terrain following coordinates, in WRF ARW denoted with η, more commonly known as σ-coordinates. West-east cross-section along the Greenland ice sheet with several η-levels (dashed lines) and the surface (solid line).*

increments on the model plane in both directions and D_s the real distance between two grid points on earth's surface, then the pair of map factors is given by

$$(m_x, m_y) \coloneqq \frac{(\Delta x, \Delta y)}{D_s}. \tag{3.2}$$

Map factors are incorporated into the governing equations, ensuring that curvature effects are accounted for. While in theory the governing equations can be solved for any domain size, the map factors have some impact on the CFL criterion and shall therefore not differ too much from 1.

3.2.4. Map projections

As mentioned in the previous section, the curved surface of the earth has to be projected to the computational plane of the WRF ARW model. The user has the choice between three different map projections: latitude-longitude (anisotropic), Lambert conformal and Mercator (both isotropic). For all projections center latitude and longitude as well as the center of the computational domain (x_0, y_0) have to be chosen.

Using the Mercator projection, which projects the earth onto a cylinder, the user has to define the so-called true latitude, where the cylinder surface intersects with earth's surface. When using the Lambert projection, two true latitudes may be chosen, since earth's surface is projected onto a cone, which may intersect the surface twice.

As it is easy to imagine, the Mercator projection is subject to poleward distortion, therefore the map factor will grow towards the poles and it is thus best suited for simulations with a large zonal extent. With a subtle choice of true latitudes, the Mercator projection has less poleward distortions, but there are of course also zonal distortions. The Lambert projection is therefore the projection of choice for domains in the mid to high latitudes with a moderate zonal extent.

Since ARW version 3.0, the so-called latitude-longitude projection is implemented. In this projection, latitudes and longitudes are assumed to be equidistant for the entire domain and the distances $\Delta x, \Delta y$ are given by the chosen angular resolution $\Delta\phi, \Delta\lambda$ in the center of the domain. The map factor will again grow towards the borders of the domain. Also note that the map factors $(m_x, m_y) \to \infty$ for $\phi \to -90°$ and for $\phi \to 90°$, because the distance on earth's surface vanishes towards the poles. The computational pole should therefore be rotated as far away as possible from the center of the domain, to keep the map factors in a reasonable range.

Given the fact, that our domain has a large zonal and meridional extent, we use a lat-lon projection for our simulations.

3.2.5. Physics and parameterizations

In any numerical weather predcition or climate model, processes occurring on a sub-grid scale are not resolved. In order to be still considered, these processes have to be parameterized. Clearly, a suitable parameterization for a given simulation depends on spatial and temporal resolution.

Because of its wide range in applications, WRF ARW provides many different parameterizations for a given process and a suitable one has to be chosen by the user. In the following, we will briefly discuss the physics options chosen for our experiments, a summary can be found in 3.2 and for the full choice of parameterizations, the reader is referred to the WRF namelist in the appendix.

Processes on the planetary scale are in the scope of this thesis, therefore parameterizations are not necessarily required to capture sub-grid scale processes in great detail and in most cases, simple and fast parameterizations are sufficient. The grid spacing of both outer domain and nests is clearly not convection-resolving (see section 3.4.2 for details on the grids) and hence a cumulus scheme is required in addition to microphysics and boundary layer schemes.

The WRF eta-microphysics scheme, which is based on the older Ferrier microphysics [*Schoenberg Ferrier*, 1994] scheme, is used to parameterize cloud processes in the outer domain. Some parameters within the scheme depend on resolution and the coarse resolution option is chosen in our case. The scheme features diagnosed mixed-phases and it is appreciated for its simplicity and efficiency. It is the operational microphysics scheme for WRF NMM models at NCEP. In the nests, the more sophisticated WRF Single-Moment 6-class scheme is used [*Hong et al.*, 2004], which is capable of capturing ice, snow and graupel processes. The focus of this scheme is rather on high-resolution simulations and one might argue that this choice does not necessarily fit the requirements of this study. However, in the nests, cloud processes possibly play an important role and this scheme features more variables than the eta-microphysics scheme [*Skamarock et al.*, 2008].

For all domains, convective processes are represented by the Kain-Fritsch cumulus scheme [*Kain*, 2004], which features both shallow and deep convection and relies on CAPE removal times τ_c (for a given convective event τ_c is defined as the timescale for removal of conditional instability by convection).

Radiation processes are captured with the Rapid Radiative Transfer Model (RRTM) [*Mlawer et al.*, 1997] for long wave radiation and with the Dudhia scheme [*Dudhia*, 1989] for short wave radiation.

The planetary boundary layer (PBL) is parameterized by the Yonsei University PBL scheme[*Hong et al.*, 2006], with expicit treatment of the entrainment layer (the interface between boundary layer and free atmosphere). Entrainment is set proportional to the surface buoyancy flux. The PBL top is set to the height, where the bulk Richardson number R_i becomes zero. Surface exchange coefficients are calculated by the revised MM5-similarity scheme [*Skamarock et al.*, 2008], which is based on Monin-Obhukov theory [*Monin and Obukhov*, 1954].

The Noah land surface model [*Chen et al.*, 1996] is used as a lower boundary condition for atmospheric fluxes over land. It is a one-dimensional column model with 4 vertical layers of 10 cm, 30 cm, 60 cm and 100 cm thickness. Apart from moisture and temperature within the layers, the model also features diagnostics for fractional snow cover and surface (skin) temperature.

3.2.6. Domain boundaries and nesting

From a mathematical point of view, regional modeling is a boundary value problem (regardless of whether we are interested in climate modeling or weather forecasting). In WRF ARW, boundary values for a given field are provided by the WRF Preprocessing System (WPS) and the vertical interpolation routine real.

Some care has to be taken when implementing boundaries in a regional model. To illustrate the problem, we consider the following gedankenexperiment: Consider a simple one dimensional domain between the points x_0 and x_1. Let us assume that we are interested in solving the one dimensional advection equation. With ∂_t being the derivative in time and ∂_x the spatial derivative, the equation reads,

$$\partial_t C = u \partial_x C \tag{3.3}$$

for an arbitrary quantity C and velocity u. In a first case, let us assume that u is constant. Any boundary value given at the left boundary at time t_0, $C(t_0, x_0)$ will propagate downstream according to $C(t, x) = u(t - t_0) C(t_0, x_0)$. At some point any value imposed on x_0 will reach the boundary at x_1. If the value of $C(t, x_1)$ is specified, it is immediately eminent, that the problem is ill-posed because the boundary is over-specified. In this simple case, we could just renounce on imposing a boundary value $C(t, x_1)$ and the problem would be well-posed again. However, imagine a slightly more complex problem, where advection in both directions is allowed. In this case we cannot circumvent the fact that we have to specify a boundary at x_1, possibly leading to discontinuities and numerical noise at the boundaries.

In practice, for a given field, the values at the boundaries given by the input data and the values inside the model domain will be close to each other (since both are solutions to the same physical problem) but not necessarily the same. In order for the two solutions to be sufficiently close together, it is crucial that the grid spacing of the model does not differ too much from the grid spacing of the input data. As a reasonable rule of thumb, the ratio of $1:3$ shall not be exceeded. For a more in depth discussion of the problem, the reader is referred to the work of *Staniforth* [1997].

In WRF ARW this problem is tackled by introducing a relaxation zone of a few (usually five or ten) grid points at the boundaries. Within this zone the solution for any given field Φ is given by a linear combination of the model solution and the input solution $\Phi = \alpha(x, y) \Phi_{model} + (1 - \alpha) \Phi_{input}(x, y)$, where the parameter α may be chosen to decrease linearly from 1 (inner boundary of the relaxation zone) to 0 (outer boundary) or with an exponential factor β to be specified by the user.

In principle, the same problem also emerges, when nesting one or more subdomains with higher resolution into a parent domain. The problem is less severe, since here the model has exactly the same dynamical core (WRF ARW) for both domains. The rules prescribed for the boundaries of the main domain also apply for the boundaries of the nests, where the output of the parent domain is used as input for the child.

3.2.7. Two-way nesting

In WRF ARW one or more nests may be embedded in the main domain. It is also allowed to embed a nest into a parent nest, allowing dynamical downscaling over multiple steps in resolution. This is particularly useful, if a user would like to achieve a very high resolution over a narrow region, because the ratio of input data to domain resolution shall not exceed $1:3$ (see previous section). Two different kinds of nesting may be distinguished. One-way nesting uses the parent domain to generate boundary conditions for the nest. The solution of the parent domain is independent of the solution obtained in the nested domain. When a two-way nest is generated, the solution inside the nested domain is fed back to the parent domain. Therefore, the solution of the parent domain depends on the solution obtained inside the nest, i.e. downstream relative to the nest. The feedback of the nest may be relaxed a little to better match the solution of the parent domain, increasing the stability of the model.

Nesting in WRF ARW is flexible and user-friendly. However, there are certain rules to respect:

- Two (and more) nests may share the same parent domain.
- Two nests must neither touch nor overlap. When two-way nesting is used, the nests need to be well separated in order to avoid mismatches between the solutions that are fed back to the parent domain.
- The nests shall be at least five (and better more) grid points away from the outer boundary of the parent domain. This is obvious, because inside this area, boundary conditions are imposed on the parent domain.

If nests are placed in bad positions (i.e. not according to above rules), the user might experience instabilities, noise or even segmentation faults. The user is free to choose, whether a nest shall receive input data from input files or whether it shall just depend on the parent domain. Note, that the computational effort increases dramatically when using nesting. For instance, if we increase the horizontal resolution by a factor of three, we have the ninefold amount of grid points within the same area and we have to decrease the time step by at least a factor three, over complex terrain most likely even more. It is therefore important to keep the nests as small as possible, whereas adding some extra grid points to the outer domain is not as computationally expensive.

3.2.8. Nudging

Nudging, or sometimes also referred to as Newtonian Relaxation, is a procedure to push the model state towards the state of user specified data. To this end, forcing terms proportional to a derived model error are added to the prognostic equations, where the model error denotes the difference between user specified data and model at a given point in space and time. Nudging is still widely used in Numerical Weather Prediction (NWP) models [*Skamarock et al.*, 2008; *Schraff and Hess*, 2012] and in this case the user specified data is derived from large sets of observations.

Whereas the usefulness of nudging cannot be denied for NWP, there is still ongoing debate, whether

nudging should be used in regional climate modeling and there are a few factors to consider. First, data assimilation techniques are prone to sampling errors: Any given value of a variable calculated by the model may be seen as an average over one grid cell. In contrast, the spatial and temporal correlation length of a given observation may be much smaller than the model grid spacing (think e.g. of rain gauges) [*Waller et al.*, 2014]. When using reanalysis products (e.g. ERA-Interim 3.3), this problem is less severe, however it must still be considered, when spatial and temporal scales of model and reanalysis data differ considerably (in whatever direction), as it is often the case for high resolution downscaling simulations. Second, the nudging terms clearly disturb the model dynamics and thus violate conservation laws. Conclusively, nudging is useful for regional climate modeling, if the available data is believed to be more accurate than the unperturbed model output, as it is often the case, when downscaling reanalysis data. For a more in-depth discussion of nudging in downscaling experiments see e.g. *Gomez et al.* [2015].

However, in the case of our experiments, the situation is different, as we know that the input (CESM) is biased against observations (reanalysis data) and we aim at eliminating part of that bias in our experiments, i.e. the bias in blocking frequency. On one hand, if we would nudge our simulations with CESM data, we would eliminate part of the expected improvement (or worsening). On the other hand, if we would nudge our simulations with reanalysis data, any improvement (or worsening) would not be clearly attributable to the settings of the experiments. We therefore relinquish on nudging in all of our experiments.

3.3. ERA-Interim reanalysis data

Era-Interim [*Berrisford et al.*, 2011] is a global reanalysis dataset provided by the European Consortium for Medium Range Weather Forecasting (ECMWF), covering the period from 1979 to present day. It is continously updated in real time with downloads available every one to two months. The reanalysis data is based on model output that is consistent with assimilated observations during the reanalysis period. ERA-Interim is based on a 2006 release of ECMWF's Integrated Forecasting System (IFS) with a 4D-var data assimilation scheme on 12 hour assimilation windows [*Dee et al.*, 2011]. The nominal resolution is approximately 80 km (T255 spectral) with 60 vertical levels ranging up to 0.1 hPa.

In this study, ERA-Interim reanalysis data covering a period from January 1, 1979 to April 30 2016 is used. Prior to any analyses on ERA-Interim fields, the data is interpolated, such that the grid spacing matches the resolution of CESM.

3.4. Experimental design

3.4.1. General design for all experiments and work flow

In this study, atmospheric data from a transient CESM simulation (850-2100 a.D., see section 3.1) is used to drive the WRF ARW model (see section 3.2) over a domain covering roughly the north

American continent, the Atlantic Ocean and Europe (Fig 3.2). The CESM data contains the following fields in six-hourly time resolution: temperature (3D), horizontal wind speeds (3D), geopotential height (3D), relative humidity (3D), 2-m temperature (2D), 2-m relative humidity (2D), 10-m horizontal wind speeds (2D), sea surface temperature (2D), surface pressure (2D), sea level pressure (2D), soil moisture (3D) and soil temperature (3D). The SST field used in ERASSTtVar is not part of the CESM output, but taken from 6-hourly ERA-Interim reanalysis data (see section 3.3). Note, that its horizontal resolution is considerably higher ($0.75° \times 0.75°$).

Except for ERASSTtVar, all simulations cover a period of 30 years and one month from June 1, 1970 to June 30, 2000. To further parallelize the workflow, the 30 year period is divided into chunks, each covering 5 years, starting at June 1, year x and ending on June 30, year $x + 5$, where $x = 1970, 1975, 1980, 1985, 1990, 1995$. This approach does not reduce computation time itself, but for each run, the data is generated six times faster. Note, that there is an overlap of one month between two chunks, which serves as spin-up for the follow-up chunk and may be discarded, once the simulation is terminated. The given spin-up period of one month ensures that the water content of the uppermost soil layer is in equilibrium with the atmosphere and can therefore provide a reasonable feedback to moisture and latent heat fluxes. The spin-up period is probably not long enough to equilibrate the lower soil levels with the state of the atmosphere, however this is found to be acceptable for two reasons. Firstly, our experiments mainly aim at altering planetary-scale circulation, which is less sensitive to variables requiring long spin-up times (i.e. soil temperature and soil moisture). Secondly, as our analyses cover only the extended winter season, the effective spin-up time amounts to five months (June 1 to October 31). The procedure is the same for ERASSTtVar, but it only covers 20 years from June 1, 1979 to June 30, 2000.

3.4.2. Domain properties

All experiments share the same outer domain (Fig. 3.2), which is generated according to the required spatial extent of our experiment and with respect to the suggestion that boundaries shall not contain regions with complex topography, if possible [*Skamarock et al.*, 2008]. Given the size of the domain, it is unavoidable to include some regions with complex topography in the boundaries and therefore four point average smoothing is applied to the terrain field during the preprocessing with WPS. Additional terrain smoothing is applied during the vertical interpolation with real by setting the corresponding namelist switch `smooth_cg_topo`. The zone with specified boundaries is set to one grid point and the relaxation zone of the outer domain is set to 4 grid points. Within the relaxation zone, the exponential decay factor (see section 3.2.6) is set to $\beta = 0.33$.

The pole latitude and longitude of the rotated pole projection are set to 30° and 180° respectively. The horizontal grid spacing is set to 0.75° at the reference point (60°N, 33°W) in both latitudinal and longitudinal direction. It consist of 150×90 grid points and the reference point of the model grid is set to $(x = 90, y = 50)$. At the center of the domain, the chosen grid spacing corresponds to 83'383.11 m and slightly increases towards the boundaries (map factors, see section 3.2.4. In the nests, the horizontal resolution is increased by a factor of three (0.25°, 27794.37 m).

Table 3.1.: *Summary of the most important WRF domain properties used in this simulation, for more details, the reader is referred to the WRF namelist (see appendix).*

Experiment	**Nests**	**SST input**	η **- levels**	**Control run**
NoN	None	CESM constant	36	is control run
CoastN	US East Coast	CESM constant	36	NoN
RockyN	Rocky Mountains	CESM constant	36	NoN
BothN	Rocky Mountains, US East Coast	CESM constant	36	NoN
NoNVertPlus	None	CESM time-varying	46	is control run
CoastNtVar	US East Coast	CESM time-varying	46	NoNVertPlus
ERASSTtVar	None	ERA-Interim time-varying	46	NoNVertPlus

Initially the timestep is set to $dt = 6 \cdot dx$ where dt is the time step and dx is the grid spacing in kilometers. This is the default setting and it is recommended as a staring point in the WRF documentation [*Skamarock et al.*, 2008]. During runtime, the maximum allowed ratio dt/dx under which the model tuns stably, is given by the Courant-Friedrichs-Levy (CFL) criterion. As the model is found to run unstable with the aforementioned rule of thumb for the starting point, for each simulation, the time step is gradually increased until no more vertical CFL violations occur. Our simulations probably required shorter time steps because of the relatively large map factors towards the boundaries of the domain. Note, that WRF ARW was designed as a mesoscale regional climate model and the outer domain covers length scales in the planetary scale. For CoastNtVar adaptive time stepping is activated with `cfl_target` = 1.2. A number of additional dynamics settings, such as vertical velocity damping and numerical diffusion is activated to further stabilize the simulation with minimal impact on the output fields [*Skamarock et al.*, 2008].

The location of the nests are indicated in Fig. 3.2. The smoothing options used for the nests correspond exactly to the options chosen in the outer domain. Note that unsurprisingly, the complex topography in the nest over the Rocky mountains causes strong vertical updrafts and the time step in the corresponding simulations has to be reduced to $dt = 90$ s for the nest ($dt = 360$ s for the outer domain) in order to not violate the vertical cfl criterion.

3.4.3. Description and motivation of the different experiments

With the domain setup described above, a total of seven different experiments are carried out. A first set of experiments uses constant SST input from CESM (unaltered SST after initialization on June 1, 1970) and aims at assessing the effect of systematically enhancing horizontal resolution with WRF two-way nesting. This set consists of an unnested control run (NoN hereafter), a run with a nest over the Rockies (RockyN hereafter), a run with a nest over the American east coast (CoastN hereafter) and a run with both described nests (BothN hereafter). All experiments in this set have 36 vertical levels.

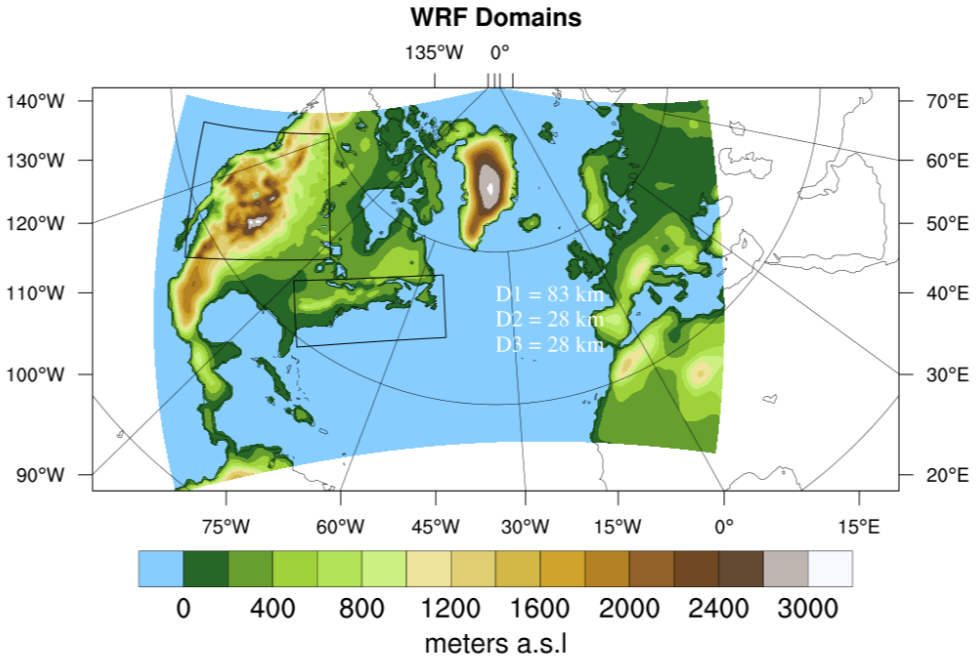

Figure 3.2.: *Model domains used in this study. The embedded domains are resolved three times higher than the outer domain.*

The enhanced resolution of the nest not only affects the calculations on the grid, but also the lower boundary condition, i.e. topographical features in the nests are better represented. Since two-way nesting transports the solution from the nest back onto the coarse domain, we expect different solutions on the coarse domain for each nesting configuration. CoastN, RockyN and BothN are designed to investigate the impact of enhanced resolution over areas we believe to be important for blocking formation. As can be derived from the theory section, these areas include the Rocky Mountains as the largest north-south barrier upstream to the impact region (Central Europe), as well as the large temperature gradients along the American east coast and Newfoundland. Thereby we assume that the coastal areas are important for eddy forcing, while the Rockies have an impact on the formation of standing waves. Analyses for these runs are carried out on the coarse domain, because we use the nesting as a mean to alter the dynamics of the atmosphere in regions of interest and analyze the downstream impact.

While the effect of time-varying SST field is completely excluded from the first set of experiments, the second set of experiments features time-varying SST fields in the lower boundary conditions. The quality of the lower boundary conditions depends solely on the accuracy and resolution of the input fields. This is particularly crucial for Atlantic sea surface temperatures (SST), where the sharp gradient in SST along the gulf stream might contribute significantly to blocking in the European Atlantic sector, as we pointed out in the theory section. ERASSTtVar and CoastNtVar are specifically designed to assess the impacts of higher resolution SST data and better representation of convective processes respectively. In CoastNtVar, we use two way nesting and dynamic SST input from CESM, in ERASSTtVar, we do not use nesting, but provide the SST input from ERA-Interim

reanalysis data. The control run (NoNVertPlus) of this set has no nests and time-varying SST fields from CESM.

The mean states of the two SST datasets are shown in Fig. 3.3. While the agreement between the

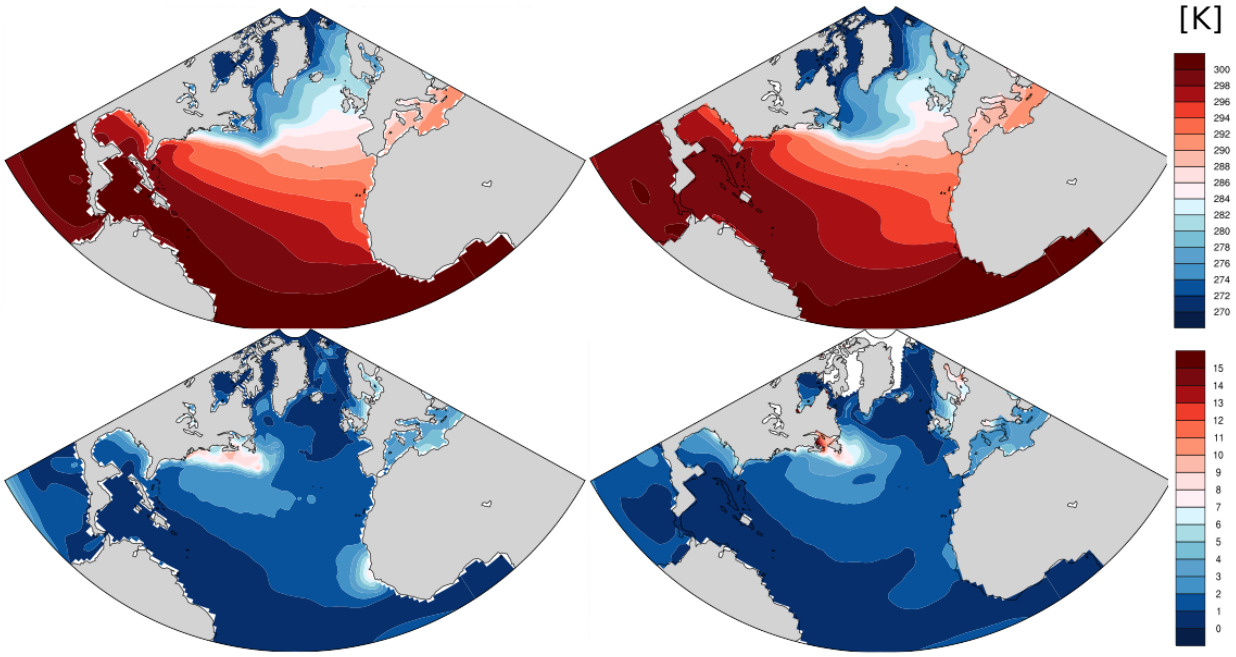

Figure 3.3.: *SST average (top) and variance (bottom) extracted from ERA-Interim (left) and CESM (right) datasets.*

two mean states is generally good, there are substantial differences that might have an impact on atmospheric circulation. Two features will be highlighted here: First, the meridional SST gradient off the northern American east coast is much higher in the ERA-Interim average than it is in the CESM average. Second, also the variance of SST differs the most in areas of high mean SST gradients, perhaps further amplifying already present gradients on the timescale of days to weeks. It must be stressed that ERASSTtVar has a major limitation. By swapping the SST fields, an inconcistency is introduced to the boundary conditions. Energy and momentum are no longer necessarily conserved. From a purely physical point of view this is highly problematic. In practice, it is assumed that sudden discontinuities in the lower temperature levels pose the bigger problem for the model. While some noise around the boundaries is inevitable, the run is found to be surprisingly stable. Conclusively, the run is acceptable as an experiment, but for potential future studies in this direction, it must be thought of a better way to assess the impact of SST representation on atmospheric dynamics.

In ERASSTtVar, CoastNtVar and NoNVertPlus, we use ten more vertical levels (hence 46 in total) than in the other runs. For these runs that are carried out later during the course of our work, we target specifically the eddy forcing contribution to blocking formation. To accurately capture the heat flux to the upper troposphere, we added η-levels to the free troposphere, where the resolution in the other runs is not as high.

The usage of WRF will itself already change the model climate compared to CESM, therefore NoNVertPlus is designed as a control run for ERASSTtVar and CoastNtVar and NoN is designed as a control run for RockyN, CoastN and BothN.

All domains are shown in Fig. 3.2 and the key properties of the experiments are summed up in Table 3.1. Note, that the resolution always refers to the reference latitude/longitude (lat, lon) pair and to the reference gridpoint (x, y) of the outer domain. The real spacing between two gridpoints might deviate substantially from these values, i.e. for grid points located close to the boundaries.

For all runs, data is preprocessed according to the chain described in section 3.2.2. Thereby, NoN, CoastN, RockyN BothN, NoNVertPlus and CoastNtVar share the same preprocessing and these runs are based on the same set of `met_em` files resulting from metgrid.

4. Methods

4.1. Expanded Tibaldi Molteni blocking index

To quantify blocking, *Tibaldi and Molteni* [1990] proposed a one-dimensional blocking index based on the gradient of the geopotential height field at the 500 hPa pressure level. Their method qualifies a given latitude as blocked, if average gradients in north- and southward direction around a central latitude of $\phi_0 = 60°\text{N}$ exceed certain thresholds. *Scherrer et al.* [2006] extended the method to a two-dimensional index by using every latitude between 35°N and 75°N with an increment (given by the grid spacing) of $\Delta\phi = 2.5°$ as central latitude. For any latitude of interest, they proceed as follows. Let Z be the geopotential height field at 500 hPa and $\Delta\phi = 15°$, a grid point at latitude ϕ is blocked if:

1. The following two gradient criteria apply:

$$\begin{aligned} \nabla_s Z(\phi) &= \frac{Z(\phi) - Z(\phi - \Delta\phi)}{\Delta\phi} > 0 \frac{gpm}{°lat} \\ \nabla_n Z(\phi) &= \frac{Z(\phi + \Delta\phi) - Z(\phi)}{\Delta\phi} < -10 \frac{gpm}{°lat} \end{aligned} \tag{4.1}$$

2. The above criteria are satisfied for at least five consecutive days.

For our analysis, we adapt the method of *Scherrer et al.* [2006], but we slightly change the second criterion by classifying a grid point as blocked, if the gradient criteria are satisfied for at least three consecutive days. By doing so, we might count some high pressure systems as blockings, a synoptician would probably not classify as such. However, depending on the simulation blocking events are rare and with our choice we expected to get statistically more robust results.
It is worthwhile to note, that while the expanded Tibaldi-Molteni index is based on intuitive criteria, it does not include any information on individual anticyclones. A shortcoming, which will be addressed by the Lagrangian tracking method presented in the next section.

4.2. Lagrangian anticyclone tracking

Originally designed to track cyclones, *Blender et al.* [1997] developed an algorithm that will locate the center of a cyclone and then follow it over its lifetime. The algorithm requires global geopotential height fields. For reference runs with ERA-Interim and CESM, data already exists on a regular latitude-longitude grid. However, this is not the case for our WRF output data, which has therefore to be interpolated to a global, regular grid. Furthermore, it is important that all data is interpolated to the same grid as gradients naturally become smoother with decreasing resolution. All model

Table 4.1.: *Parameter choice for the Lagrangian tracking algorithm.*

parameter	**value**
`gzmin`	35 gpm/°lat
`gzmax`	55 gpm/°lat
`srmax`	`= int(1.0+nlo/64*(dt/6.)**0.75)`
`agemax`	180 steps (60 days)
`agemin`	12 steps (3 days)

output fields were therefore interpolated to a regular $1.25° \times 0.9°$ grid. Since data is missing outside the WRF domain, artifacts in the geopotential height field are found close to the border of the domain. The simulations also tend to be noisier around the boundaries. Therefore, we exclude regions close to the domain boundaries from our analysis.

The algorithm was then successfully applied to anticyclones (merely sign changes in the code and adaption in magnitude) by *Buehler* [2008].
The main steps in the algorithm are:

- Detection of a sufficiently strong maximum in the 500 hPa geopotential height field.
- Tracking of the maximum over time.
- Filtering of anticyclone tracks with further criteria.

Once a maximum is found in the geopotential height field, the mean gradient around the maximum is calculated by,

$$\nabla Z_{500} = \sum_{i=-m}^{i=m} \sum_{j=-n}^{j=n} \frac{Z_0 - Z\,(i,j)}{\sqrt{(i\Delta x)^2 + (j\Delta y)^2}} \tag{4.2}$$

in a radius of approximately 1000 km. At this point a first criterion is applied, the calculated average gradient must exceed a threshold imposed by `gzmin` for the anticyclone to be tracked. The algorithm then conducts a nearest neighbor search within a radius given by the parameter `srmax`. If a close-by maximum (again exceeding the gradient threshold) is found in the consecutive step, the algorithm assumes the two maxima to belong to the same anticyclone and adds the latter to the track of the first. This way, the algorithm generates a list of anticyclone tracks of variable length. Now, three more criteria are imposed on the tracked anticyclones. The average gradient has to exceed a second threshold, `gzmax` at least once in the lifetime of the anticyclone and the system has to persist for a value greater than `agemin`. Finally, anticyclones that persist for a duration greater than `agemax` are excluded from the further analysis. This will likely exclude some artifacts arising from topography or interpolation features. If the tracked anticyclone satisfies all four criteria, we count it as a blocking event.

Table 2 summarizes our choice of parameters for the tracking algorithm. The search radius `srmax` is determined by the given formula, where `nlo` is the longitudinal grid size and `dt` is the time step in

hours. The radius calculated this way always lies in the order of $500 - 1000$ km, which corresponds roughly to the Rossby deformation radius. Note that the threshold for persistence is set to three instead of five days in order to obtain statistically more robust results, as we did for the extended Tibaldi Molteni index. We chose our parameters according to *Buehler* [2008], as they carried out multiple sensitivity studies with different parameter choices.

For each time step, the blocking event persists, a 1D Gaussian is fitted around the center of the anticyclone. More precisely, when r is the euclidean distance from the anticyclone center, the Gaussian is fitted to the geopotential height $z(r)$ as a function of r. The shape of the Gaussian anticyclone around its center is then given by

$$z(r) = \frac{z_c}{\sigma\sqrt{2\pi}} e^{-\frac{r}{2\sigma}}, \tag{4.3}$$

where z_c is the geopotential height at the anticyclone center and σ is the standard deviation (shape parameter) of the Gaussian estimated by the fitting routine. The estimated standard deviation can now be considered as a measure of anticyclone size and for a given time step, all grid points within the radius of one standard deviation ($r = \sigma$) around the anticyclone center are considered as blocked. This way, two dimensional blocking count fields are retrieved from the algorithm. To obtain frequencies, the blocking counts are then divided by the total number of time steps over which the algorithm is run.

Fig. 4.1 shows a tracked anticyclone and the radius obtained by the Gaussian fitting. and as can be seen, the Gaussian fitting is found to be rather conservative and a typical blocking event usually has a larger (i.e. zonal) extent. Nevertheless, the Gaussian fitting as it is presented here, yields a conservative and event-oriented measure of blocking frequencies.

Note that the blocking frequencies found this way are lower than the frequencies found by *Buehler* [2008], as they calculate the frequency normalized to an area of 1000 km^2. This was done in order to account for the fact that the grid point area decreases with latitude. Using the Gaussian fitting, this normalization is obsolete, as this effect is already accounted for, because the Gaussian radius is already calculated based on horizontal distances.

The Lagrangian tracking (LAGTRACK hereafter) is applied to the data for each individual extended winter season, yielding a total of 30 (20 for ERASSTtVar) blocking frequency fields. These fields are then averaged over the 30-year period. Apart from the climatological mean, a sample of 30 (20 for ERASSTtVar) frequency fields is obtained for each experiment, which may then be used for statistical testing.

4.3. Latitude of the low level jet

As we saw in the introduction, a comprehensive study by *Scaife et al.* [2010] pointed out, that the underestimation of blocking in climate models could to a major part be attributed to errors in the mean state of the models. We argue, that mean state errors could arise due to key topographic

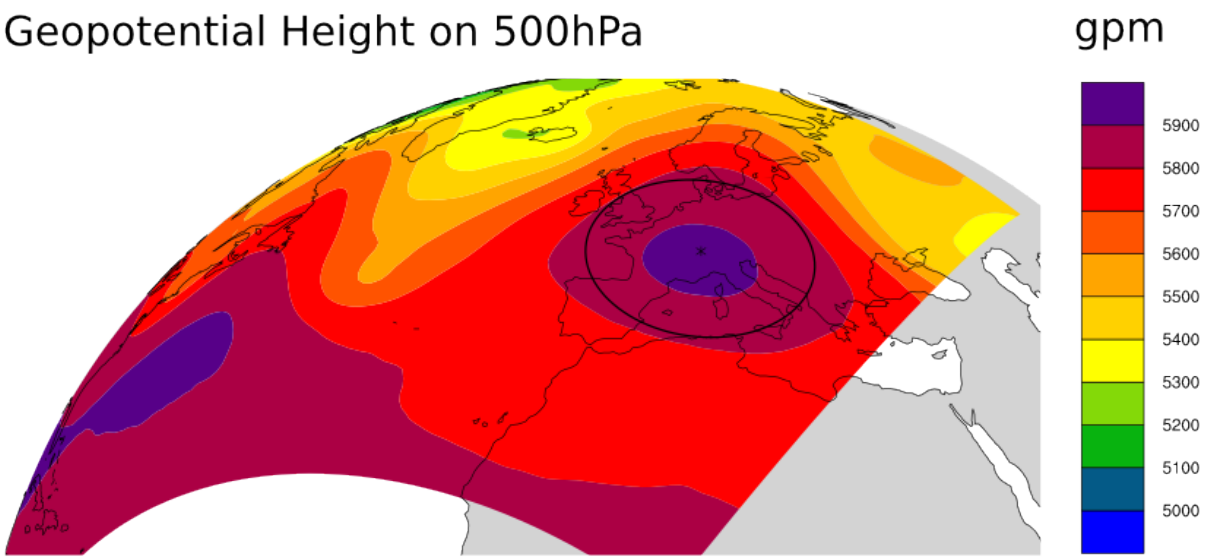

Figure 4.1.: *Tracked anticyclone in the ERASSTtVar simulation on November 5, 1979, 12:00. The local maximum in the geopotential height field detected by the LAGTRACK-algorithm is indicated with a black cross and all grid points inside the black circle were counted as blocked at that timestep.*

features such as the Rocky Mountains and the coast of Newfoundland not being resolved well enough. In a recent study, *Merz et al.* [2015] found that the distribution of the mean jet latitude over the northern Atlantic has a unimodal distribution in the CCSM4 model rather than a distinct trimodal distribution as found by *Woollings et al.* [2010] in 20th century reanalysis data. We expect the CESM mean jet latitude distribution to be similar as in the CCSM4 model. The mean latitude of the low level jet is determined by:

- Vertically averaging the zonal component of the horizontal wind speed between $p_1 = 925$ hPa and $p_2 = 700$ hPa.
- Zonally averaging the obtained low level zonal wind speed between 60°W and 0°.
- Low pass filtering with a ten-day Lanczos filter.

The obtained results are then binned with a 1° and a 5° increment respectively to get an empirical density function (EDF) of the low level jet position.

4.4. Principal component analysis

To further assess the impacts of our experiments on the lower troposphere, monthly mean sea level pressure (SLP) fields are investigated by means of a principal component analysis (PCA). Briefly summarized, the working principle of a PCA is as follows: First, eigenvectors and corresponding eigenvalues of the covariance matrix of the sample (in this case the pressure values at the individual grid points over time) are calculated and sorted in descending order of the eigenvalues. For each eigenvector λ_k, the ratio $\lambda_k / \sum_i \lambda_i$, where i is running over all eigenvalues, is the fraction of explained

variance by the eigenvector e_k. Therefore one retrieves an orthogonal system of eigenvectors (here spatial patterns of pressure anomalies) in descending order of their contribution to the overall variance of the system (here pressure anomaly over time). A detailed description of PCA (often also referred to as empirical orthogonal function (EOF) analysis) can be found in any statistics textbook, e.g. *Wilks* [2011].

To save computational effort, the field is thinned by a factor 2, meaning that only every second grid point is considered in the subsequent analysis. For each month, a 30 (20 for ERASSTtVar) year average is calculated and this climatology is subtracted from the SLP field to obtain monthly SLP anomalies. A PCA is then run along the time axis over all 30 (20 for ERASSTtVar) winter seasons in the experiment.

The vector space spanned by the principal components is truncated after $n = 20$ principal components, because we expect, that most of the variance is explained in the first few principal components. This way, the 20 (spatial) patterns that explain most of the variance in the SLP anomaly are retrieved as two dimensional pressure fields. By convention, we refer to these patterns as empirical orthogonal functions (EOFs). For each month, a relative amplitude of a given EOF is obtained, this amplitude is referred to as PC score or short PC and it is normalized, such that the variance of the PC score over time is equal to one. As any EOF has an arbitrary sign (if e_i is eigenvector of the covariance matrix, so is $-e_i$), it can only be physically interpreted (distinction between high and low pressure anomalies at a given time), if the corresponding PC score is shown.

To compare different experiments, differences in the EOF patterns of the respective experiments may nevertheless be discussed without comparing the corresponding amplitudes. For each experiment zones of high and low variability may be identified and differing locations of these zones indicate a change in the underlying model state. However, if two experiments are compared with respect to the amplitude (positive and negative) of a given EOF, the SLP anomalies of the second experiment are projected (this corresponds to a scalar multiplication for each monthly field) onto the EOF of the first experiment. By doing so, the PC score of the first experiment may directly be compared to the time series obtained by the scalar multiplication. Note that this time series is not normalized and the variance is not necessarily smaller than one, if the second experiment exhibits generally lager variance than the first one.

5. Results and discussion

First, blocking frequencies and characteristics in the different setups are compared. Then, the imprint on the location of the low level jet is investigated in the control run and in the simulations exhibiting the highest blocking frequencies. Monthly pressure anomalies are investigated with a principle component analysis. The evolution of a blocking event in different simulations is shown by means of a composite analysis and a case study, where we also discuss possible mechanisms for blocking formation in our simulations. Finally, a loser look is taken at baroclinic instability over the Atlantic. If not mentioned differently, all analyses are carried out for the extended winter season (November to April). Differences between the simulations for each quantity are discussed in the respective chapter, an overall summary and outlook will then follow in the subsequent chapters.

5.1. Blocking frequencies

5.1.1. ERA-Interim, CESM and unnested WRF runs: A first comparison

As two different measures of blocking frequency (LAGTRACK and TIMO) are used in the subsequent analyses, the two methods are first compared to find out, whether they capture blocking events in similar regions. To find differences and similarities between the two methods, we consider the spatial distribution of blocking frequencies for ERA-Interim reanalysis data (Fig. 5.1, top panels).

Foremost, note that the frequencies found with the two methods differ in magnitude, with blocking frequencies in the order of $0-1\%$ for LAGTRACK and $1-10\%$ for TIMO. Clearly, the two methods follow a fundamentally different approach and the fact that the outcome differs, is therefore not surprising. Nevertheless, the blocking frequencies found with LAGTRACK are very low (1% blocked time steps corresponds to roughly two blocked days per extended winter season). The generally very low frequencies found with LAGTRACK may at least partially be explained by the fact that the blocking extent is estimated very conservatively. In LAGTRACK, the spatial distribution of blocking frequencies reveals more details, possibly an advantage of the conservative estimation of blocking extent.

Both methods agree relatively well on the shape of the frequency distribution in the European Atlantic sector around the British isles and further west as well as further north around southern Greenland and Island. The agreement over northeastern Europe and Scandinavia is generally good although it should be noted that the analyses carried out with TIMO do not extend as far to the north as the analyses carried out with LAGTRACK. This is due to the fact, that the TIMO algorithm always requires a grid point 15° northward of the grid point, where the index is calculated. The northernmost grid point, where blocking frequencies can be calculated with TIMO is therefore

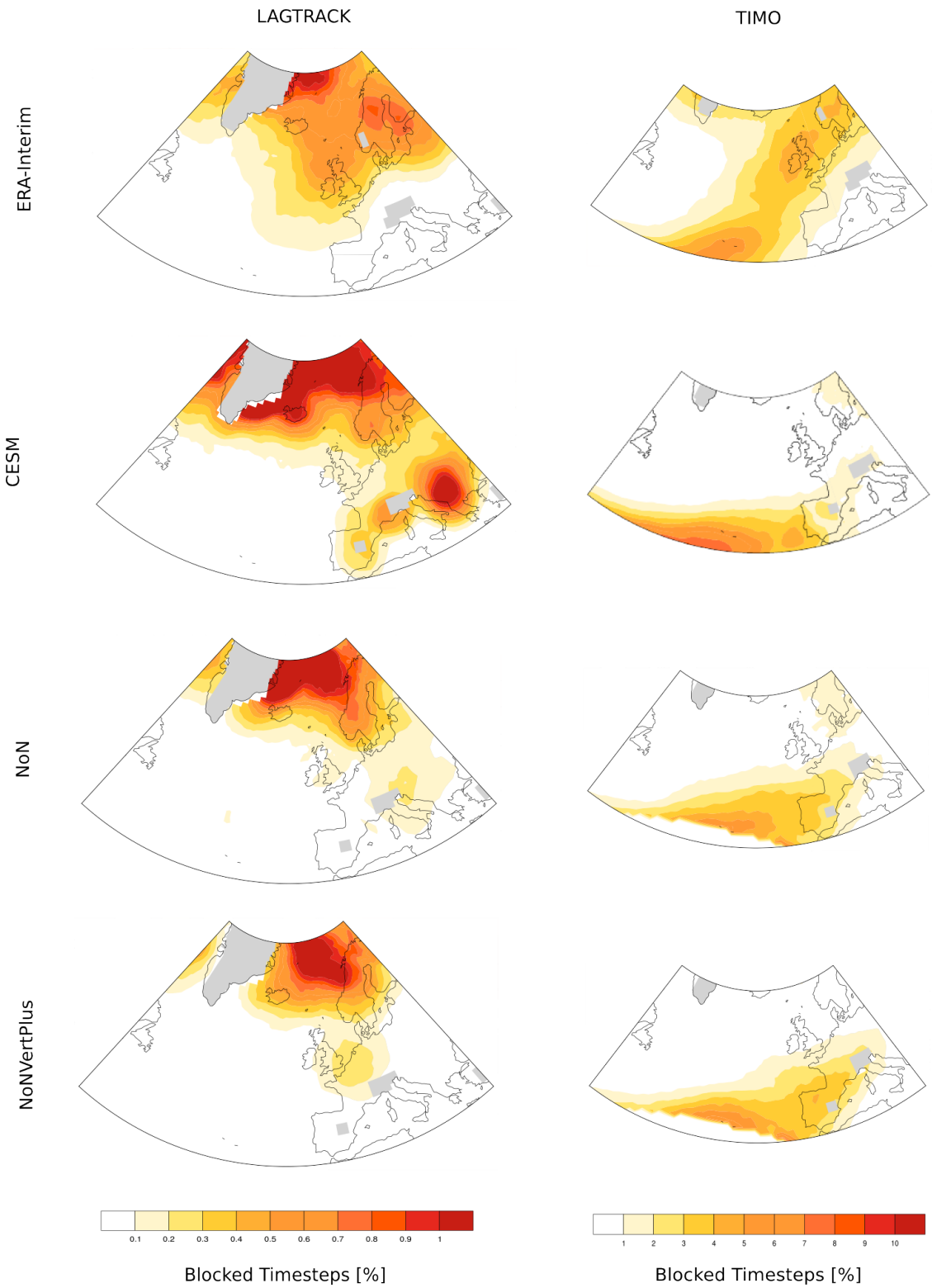

Figure 5.1.: *Blocking frequencies as found with the LAGTRACK index (left) and the TIMO index (right) for (top to bottom) ERA-Interim, CESM, NoN, NoNVertPlus. For both indices, the unit is percentage of blocked time steps with respect to the total number of time steps. Regions, where terrain elevation exceeds* 1000 *m a.s.l. are not considered in the analysis and therefore shown in grey.*

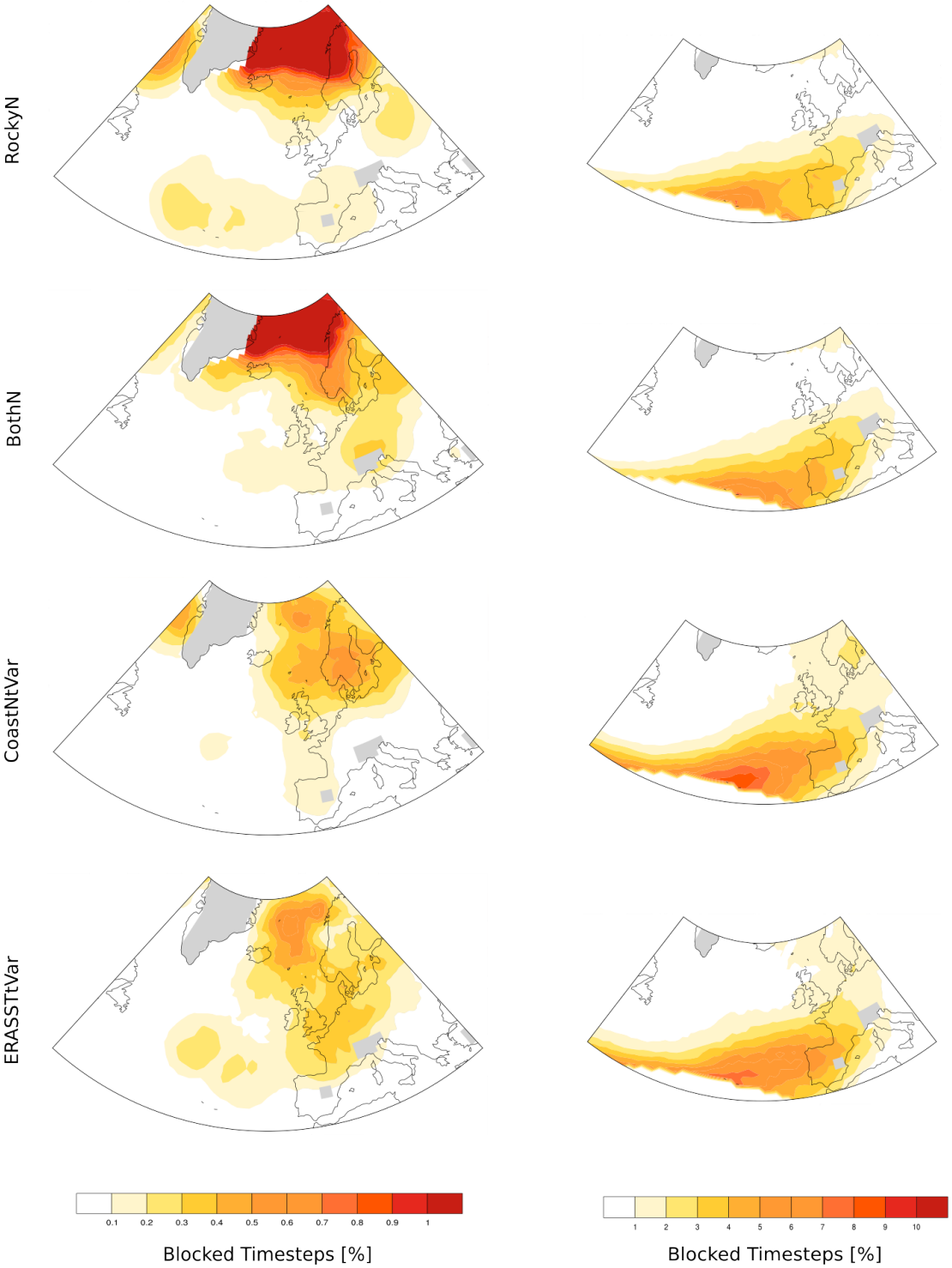

Figure 5.2.: *Blocking frequencies as found with the LAGTRACK index (left) and the TIMO index (right) for (top to bottom) RockyN, BothN, CoastNtVar, ERASSTtVar. For both indices, the unit is percentage of blocked time steps with respect to the total number of time steps. Regions, where terrain elevation exceeds* 1000 *m a.s.l. are not considered in the analysis and therefore shown in grey.*

given by the northward extent of the simulations and lies around 70°N. Note, that the TIMO algorithm detects stable high pressure systems south and west of the Iberian peninsula, which are not found with the LAGTRACK algorithm. This could be due to the fact that high pressure systems in these regions already belong to the stable subtropical high pressure belt and therefore lack distinct maxima and strong gradients. These systems are anyways too far south, to block the westerly flow and will be omitted in the further discussion. Apart from the differences in absolute frequencies, the two methods are found to agree reasonably well and both methods are used for further analyses.

State of the art climate models have been shown to underestimate blocking frequencies in the European Atlantic sector (see chapter 1). This is also true for the investigated CESM run, as has already been shown by Sandro Blumer (personal conversation, January 2016). Here, blocking frequencies in CESM are calculated using both methods, to confirm previous studies and to get a clear picture of the spatial distribution of blocking events in CESM. When compared to ERA-Interim, a clear underestimation of blocking frequencies is found around the British Isles and over the eastern Atlantic Ocean in CESM (Fig. 5.1, 2nd row from top). In contrast, CESM exhibits higher blocking frequencies further north (east of Greenland). This might imply that the climatology in CESM overestimates the strength of the subpolar high and the pressure depression along the storm track.

Interestingly, LAGTRACK shows enhanced blocking frequencies over central to southern Europe. These events are mostly too far south to be considered as blockings and they are furthermore not captured with the TIMO index. Also, note that these features coincide with the mountain ranges of the Pyrenees, the Alps and the Pindus and we speculate that these features might arise due to the underlying orography, even if grid points located higher than 1000 m a.s.l are excluded from the analysis. For the given reasons, we omit any further discussion on these events. The underestimation of blocking frequency in the CESM model is in good agreement with the findings of *Buehler et al.* [2011] for the CCSM3 model. This highlights the importance of further research in this field and motivates further analyses on our experiments.

As the misrepresentation of bocking frequencies in CESM is found to be evident, we extend the analyses on blocking frequencies to our experiments. To this end, we must first quantify the effect of using coarse resolution WRF runs instead of CESM and hence establish blocking climatologies for the unnested control runs NoN and NoNVertPlus. Recall that NoN uses SST just at initialization as an input field and has 36 η-levels, NoNVertPlus uses time varying CESM SSTs in the lower boundary condition and has 46 η-levels.

Figure 5.1, third and fourth row show blocking frequencies for NoN and NoNVertPlus runs respectively. The patterns found with the TIMO algorithm are overall similar to the corresponding pattern of the CESM run. Blocking frequencies are underestimated over the eastern Atlantic ocean. In both simulations, the blocking belt ranging from the Iberian peninsula to central Europe reaches further north and east than it does in CESM. In NoN, some events are even detected over Scandinavia.

With the LAGTRACK algorithm, similar patterns are found for both unnested simulations, with

high blocking frequencies north of about 60°N and almost no detected events over the Atlantic ocean. Compared to CESM (see Fig. 5.1), blocking frequencies are overall lover, but more concentrated around the British Isles. The pattern in NoN is more similar to the one found in CESM as more events are detected over central, southern and eastern Europe than in NoNVertPlus. The differences between CESM and the unnested WRF runs may arise from the already slightly enhanced overall resolution or the different dynamical cores and parameterizations of the two models.

Irrespective of the method, a clear underestimation of blocking frequencies is evident in both simulations, when compared to ERA-Interim and both experiments exhibit similar blocking climatologies as CESM. Conclusively, we will use both unnested WRF runs as control simulations for all further experiments.

5.1.2. The impact of enhanced resolution

The representation of both orography and convective processes is clearly resolution dependent. In chapter 2, the Rocky mountains and the region around the American east coast are identified as key regions for blocking formation. In the two nested simulations RockyN and BothN, horizontal resolution is inceased by a factor three over the Rockies and over both key areas, respectively. To assess the impact of locally enhanced resolution, blocking climatologies are also established for the nesting experiments RockyN and BothN.

The differences in frequency to NoN are checked for significance with a two-sided Mann-Whitney-U test (for each grid point separately), but no coherent regions of significant difference in frequencies are found. Two major reasons may be identified to explain, why this is the case even though the patterns look quite different. First, we state that all runs exhibit a large inter-annual variability. Second, both TIMO and LAGTRACK are binary indices and therefore sampling is not as straightforward as it would be for a continuous field (such as e.g pressure). For both methods, one extended winter season is one sample in the Mann-Whitney-U test, leading to a relatively small sample size of $N = 30$.

The results shown in Fig. 5.2 demonstrate that increasing horizontal resolution over the Rockies and the American east coast has a visible impact on blocking frequencies. While blocking frequencies are found to be similar to CESM north of about 60°N, RockyN and BothN both show a band of enhanced blocking frequencies in the eastern Atlantic when analyzed with the LAGTRACK algorithm. The band lies more northward in BothN and matches the reanalysis data (Fig. 5.1, top panel) better. This enhancement in blocking frequency is in line with the findings of *Berckmans et al.* [2013]. Nevertheless, even the enhanced LAGTRACK blocking frequency differs substantially from the one found in reanalysis data and the enhancement is not captured with the TIMO algorithm. Together, these findings indicate that in these two cases, solely increasing horizontal resolution did not have a major impact on blocking frequencies in the European-Atlantic sector.

In a next step, time-varying CESM SST input is combined with increasing horizontal resolution (CoastNtVar experiment) over the American East coast. This experiment aims at a more realistic capturing of baroclinic processes, which are important to blocking formation. CoastNtVar differs

from the other nested runs as a time-varying CESM SST field is used as lower boundary condition and the simulation has ten more η levels. The blocking frequencies found in CoastNtVar is therefore compared to the other unnested (control) simulation NoNVertPlus, which also has time-varying SST input and 46 η levels. Prior to discussing differences between CoastNtVar and NoNVertPlus, it should be mentioned that again, no regions of coherent significant differences are found when testing with a two-sided Mann-Whitney-U test. The remark on hypothesis testing given above, is also valid in this case.

With the LAGTRACK index, the zone of high blocking frequencies ($> 30\%/1000\text{km}^2$) extends further southward down to northern Scotland. Conversely, the blocking frequencies in the immediate vicinity of Greenland and Island are found to be a bit lower. Furthermore, CoastNtVar exhibits a belt of enhanced blocking frequencies ranging from the British Isles over western France and south to the Iberian peninsula. The same feature may be retrieved with the TIMO index as a belt of enhanced frequencies ranging from southern England north to Scandinavia. Note, even though weaker and slightly displaced to the east, this feature is similar to the blocking belt found in ERA-Interim data. CoastNtVar is the only simulation with CESM SST fields as lower boundary conditions exhibiting such a belt.

Despite the result not being statistically significant, it tends towards a more realistic representation of blocking frequencies. The nesting over the American east coast surely improves the way the land-sea contrast (and hence the warm-cold contrast) is represented in the simulation. This in turn is probably the major driver for the observed improvement.

5.1.3. The impact of model SST biases

We highlighted the importance of accurate SST representation in climate models to the planetary-scale circulation in section 2.3. The results found for CoastNtVar strengthen this view as a better representation of land-sea contrast leads to more realistic blocking frequencies. The idea that Atlantic SSTs are a key driver for European blocking [*O'Reilly et al.*, 2016] is investigated in more detail by replacing the CESM SST field with the ERA-Interim SST field in the lower boundary. In the following we will compare the results found for ERASSTtVar with the unnested (control) run NoNVertPlus and also with CoastNtVar as these two runs also have time-varying SST fields as lower boundary conditions.

Indeed, when comparing ERASSTtVar to NoNVertPlus, strongly enhanced blocking frequencies are observed. Using the LAGTRACK method, blocking frequencies over the eastern Atlantic and over western Europe are found to be even higher in ERASSTtVar than in CoastNtVar. The same is true for central Europe and it should be stressed that blocking frequencies are slightly overestimated for central Europe when using ERA-Interim data as a reference. This overestimation can also be interpreted as an eastward displacement (compared to ERA-Interim) of elevated blocking frequencies. In this view, we also raise the interesting question as to whether it is possible to disentangle the causes for overall frequency improvement on one hand and the causes for the displacement of regions with high blocking frequencies on the other hand.

A slight enhancement of blocking frequencies in ERASSTtVar is also captured by the TIMO index and the pattern is very similar to the one found in CoastNtVar. It seems plausible that these two simulations exhibit more realistic blocking frequencies for similar reasons. The key property distinguishing them from the other simulations, is that both runs have an improved representation of processes related to SST gradients and land-sea contrasts, such as latent heat fluxes close to the American east coast. While the enhancement might not seem as substantial as the one observed with the LAGTRACK method, ERASSTtVar and CoastNtVar also exhibit by far the largest improvement in TIMO blocking frequency.

Conclusively, switching SST fields has had a stronger impact on blocking frequencies than increased horizontal resolution. Even though this finding is again statistically not significant, we still believe it to be important for the following two reasons: First, the observed change in the spatial frequency distribution is clear and moreover, the difference to the control run is far better visible for ERASSTtVar than for any of the runs with increased horizontal resolution. Second, the sample size for hypothesis testing is even smaller for ERASSTtVar ($N = 20$) than for the other simulations ($N = 30$). Given the large inter-annual variability, it is therefore very hard to obtain statistically significant differences even if the differences between ERASSTtVar and NoNVertPlus are substantial.

5.1.4. Blocking properties

For each blocking event, descriptive quantities are stored by the LAGTRACK algorithm. While these quantities reveal valuable information on individual events, they may also be exploited for statistical considerations. Subsequently, we will investigate the climatological means of blocking properties with two main focuses. Firstly, we check whether the blocking properties are in line with the spatial distribution and secondly we look for additional information not revealed in the spatial distributions. To this end, duration, maximum Gaussian radius during the event, maximum intensity and event mean latitude are extracted from LAGTRACK output (see section 4.2) for all simulations except CoastN for events in a restricted area between 60°W to 40°E and 30°N to 75°N. Box plots are calculated and the differences between simulation and respective control simulation (NoN for RockyN and BothN, NoNVertPlus for CoastNtVar and ERASSTtVar) are checked for significance using a two-sided Mann-Whitney-U test.

While CoastNtVar and ERASSTtVar exhibited the clearest enhancement of blocking frequency over the Atlantic and Central Europe, it is worthwhile noticing that their sample sizes are considerably smaller than the other sample sizes (Table 5.1), meaning that LAGTRACK recorded overall less blockings in the considered area. This apparent contradiction may be explained at least partially, by the fact that the event mean latitude is shifted southward relative to the event mean latitude in the control run NoNVertPlus. This shift in latitude is found to be significant on a 95% confidence interval for both runs (Table 5.1). As the findings in chapter 5.1 indicate, no simulation severely underestimates blocking northward of about 60°N. However, as can be seen in Fig. 5.3, bottom right, the majority of blocking events recorded in NoN, RockyN, BothN and NoNVertPlus is captured in this region and does therefore not actively contribute to a more realistic representation of blocking

frequencies. Thus, we highlight this significant shift in blocking latitude as an important contributor to the improvement of blocking representation in CoastNtVar and ERASSTtVar.

The signal in the other blocking properties is not as clear as for the mean event latitude. The median duration seems to be a bit longer for ERASSTtVar than for the other simulations, which might further contribute to the contradiction of higher blocking frequencies with fewer recorded events. For CoastNtVar, the anticyclone radius is significantly larger than for NoNVertPlus, but as stated in section 4.2, the anticyclone radius is not necessarily a realistic measure for the spatial extent of a blocking event. No clear signal is obtained for anticyclone intensities. However, we also argue that this quantity is probably not as important to characterize large-scale blocking events, as these events do typically not exhibit strong gradients in geopotential height within 1000 km around their center.

While not much further insight is gained from the blocking properties, the observed shifts in latitude for CoastNtVar and ERASSTtVar and the enhanced duration in CoastNtVar are in line with the observed spatial distribution of blocking frequencies.

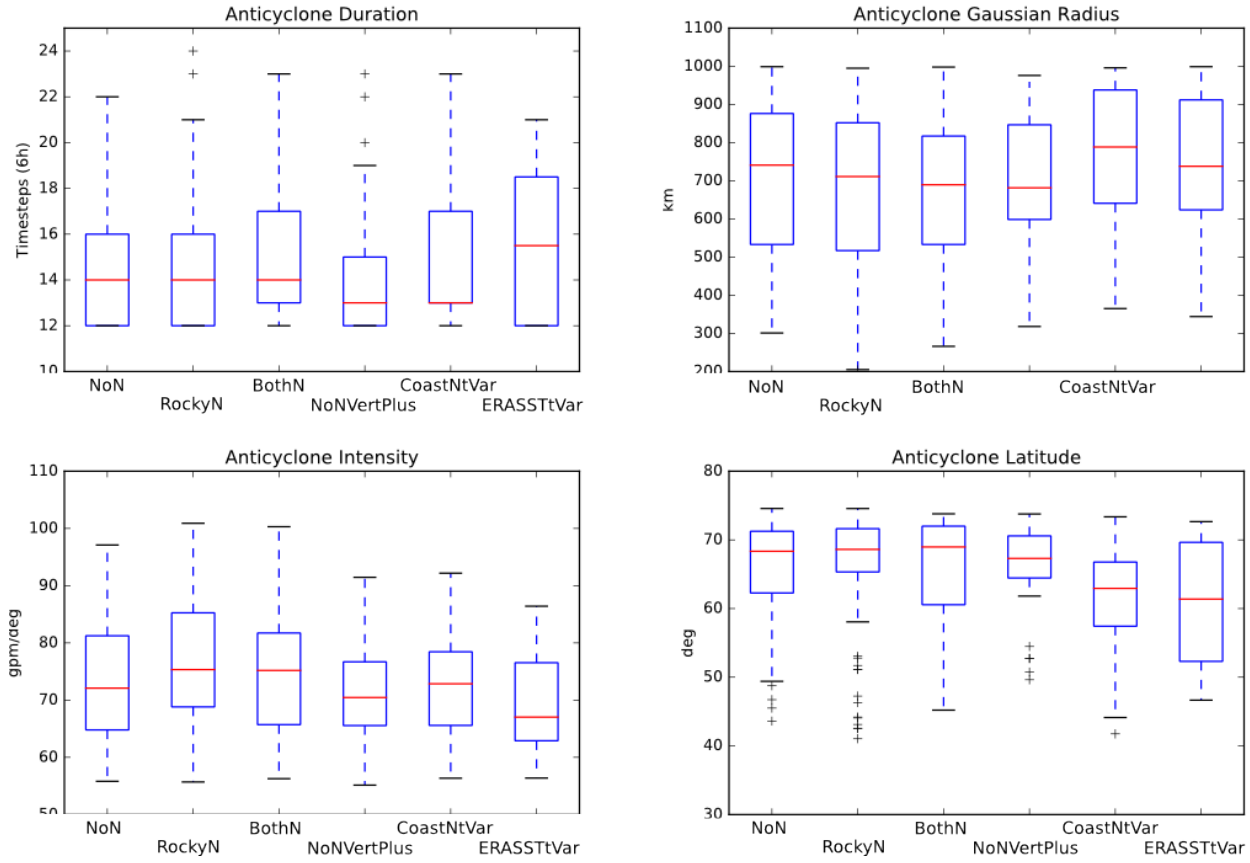

Figure 5.3.: *Boxplots of some event properties found in NoN, RockyN, BothN, NoNVertPlus, CoastNtVar and ERASSTtVar. The box contains the 25th to 75th percentile, the lines include the 5th to 95th percentile. Values outside this range are considered as outliers and shown as crosses. Considered are only events in a restricted area between 60° W to 40° E and 30° N to 75° N. Shown are event duration (top left), largest gaussian radius (top right), maximum intensity (bottom left) and event mean latitude (bottom right).*

Simulation (control simulation)	**Sample Size**	**Duration**	**Largest Gaussian Radius**	**Maximum Intensity**	**Event Latitude**
RockyN (NoN)	$N = 76$	$p = 0.82$	$p = 0.85$	$\mathbf{p = 0.02}$	$p = 0.55$
BothN (NoN)	$N = 93$	$p = 0.13$	$p = 0.69$	$p = 0.24$	$p = 0.81$
CoastNtVar (NoNVertPlus)	$N = 40$	$p = 0.35$	$\mathbf{p = 0.02}$	$p = 0.24$	$\mathbf{p = 0.0007}$
ERASSTtVar (NoNVertPlus)	$N = 28$	$p = 0.13$	$p = 0.19$	$p = 0.64$	$\mathbf{p = 0.03}$

Table 5.1.: *P-Values for RockyN, BothN, CoastNtVar and ERASSTtVar event property distributions compared to the distributions of the control runs NoN and NoNVertPlus. P-values indicating significance on the 95% confidence interval are bold. The control runs have sample sizes of $N = 62$ for NoN and $N = 48$ for WRF tropo. All p values are obtained with the non-parametric Mann-Whitney-U test.*

5.2. Position and strength of the low level jet

In the previous section, we have shown that blocking frequencies in the European Atlantic sector are underestimated by CESM and that the spatial distribution of blocking frequencies differs substantially in the different models. For both LAGTRACK and TIMO, blocking events are defined by gradients in the geopotential height field. Clearly, the presence of meridional gradients in the 500-hPa geopotential height field has an impact on zonal wind speeds in the lower troposphere. In the presence of a blocking event, the westerly flow is interrupted around the center of the blocking and then shifted north- or southward around the blocking. We would therefore expect that a change in the spatial distribution of blocking events also has an impact on the position of the low-level zonal wind. The low level jet is defined and calculated according to the Woollings algorithm [*Woollings et al.*, 2010] presented in section 4.3. This analysis is restricted to the winter season (December - February), to have as little seasonal variation as possible.

5.2.1. Jet position in CESM and unnested runs

Given the above finding that blocking frequencies in CESM and in the unnested control runs are severely underestimated around the British isles and overestimated further north, we expect to see a clear imprint on the low-level jet, when we compare the corresponding jet position histograms to ERA-Interim.

Consider the position histograms of ERA-Interim (Fig. 5.6, left) as a reference and note that in agreement with *Woollings et al.* [2010], a clear trimodal structure in the low level jet position histogram is found. The main maximum lies around 45° N with two smaller maxima $\approx$ 10°N and 10°S of the main maximum. The northern (southern) maximum is associated with blocking events over southern (northern) Europe. To facilitate the visual comparison between the histogram structure in ERA-Interim and the experiments, the northernmost peak and the northern tail are highlighted in green.

Coherent with the underestimation of blocking frequency, this trimodal structure is not retrieved for CESM in Fig. 5.6. The histograms from NoN and NoNVertPlus are checked for significant deviations from CESM with a paired, two-sided non-parametric Mann-Whitney-U test. No significant deviation was found and the distributions all are similar to the one shown in Fig. 5.6. We therefore relinquish on showing the histograms retrieved from NoN and NoNVertPlus data. There is a small maximum at around 33°N, possibly associated with high-latitude blocking events. But some care has to be taken when interpreting the maximum as it vanishes, when binning to five degree latitude bins (not shown). Note, that the northernmost peak and the northern tail are practically absent in the CESM histogram. This finding indicates, that the variability in the zonal position of the low level jet is too small in CESM, NoN and NoNVertPlus.

Consider the difference in mean low level jet strength between ERA-I and CESM in Fig. 5.4. Clearly, the average low level zonal wind is overestimated in CESM around the main jet latitude of around 45°N. Note, that this does not necessarily mean, that the modeled wind is too strong in this region.

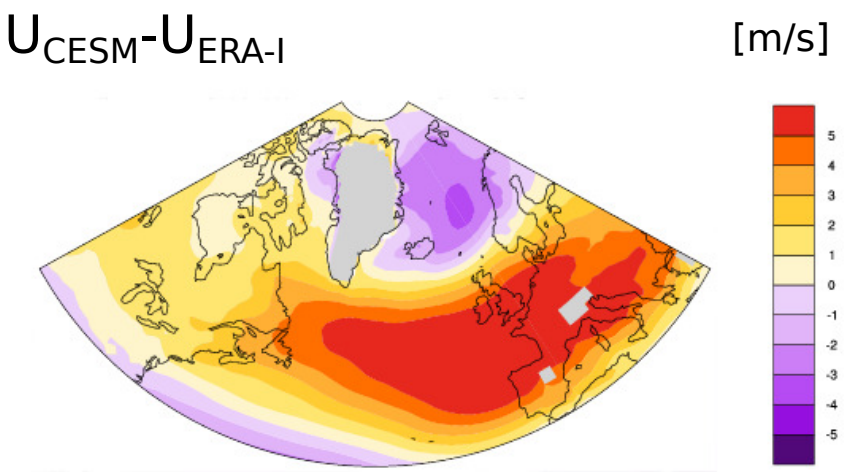

Figure 5.4.: *Difference in average zonal low level (925 to 700 hPa) wind speed between CESM and ERA-I. The low level wind speed is determined the same way as for the histograms in figure 5.6.*

The synoptic situations (i.e. blocking), where the jet is displaced northward (southward) to the main latitude are probably just underestimated in CESM and do thus not contribute to the overall average. The same is true in the opposite direction for the underestimation of the low level jet speed eastward of Greenland.

The fact that the zonal wind does not exhibit a trimodal structure is certainly a result of under-represented atmospheric blocking around the mean jet latitude. However, it is possible, that the unimodal wind distribution is not only an effect caused by the absence of blocking in CESM, but it could in turn also further contribute to it. Figure 5.5 shows the first principal component of the daily mean sea level pressure anomaly and the corresponding time series with daily resolution. A positive amplitude in the time series shows the signature of a high pressure system with center over the British Isles. It is remarkable that this signature (here shown for winter 1970/71) is found in the PCA despite the absence of blocking events according to LAGTRACK and TIMO.

It seems plausible that the model produces high pressure systems, but they are probably to unstable and short-lived to be detected by LAGTRACK and TIMO. This relative instability compared to the blockings in the reanalysis data can also be due to the overestimation of the low level jet strength at these latitudes. This view is supported by the fact that blocking frequencies are very sensitive to the duration criteria in both analyses [*Buehler*, 2008].

5.2.2. Jet position in selected setups

As ERASSTtVar and BothN exhibit the most prominent changes in blocking frequencies, the Woollings algorithm described in section 4.3 was also applied to these experiments. It must be noted, that ERASSTtVar contains ten less winter seasons than BothN (and all other simulations). In ERASSTtVar and BothN the distribution of the lower level jet maxima are slightly broader than in NoN and NoNVertPlus (Fig. 5.7). The shifts are not significant ($p = 0.98$ for BothN and $p = 0.06$

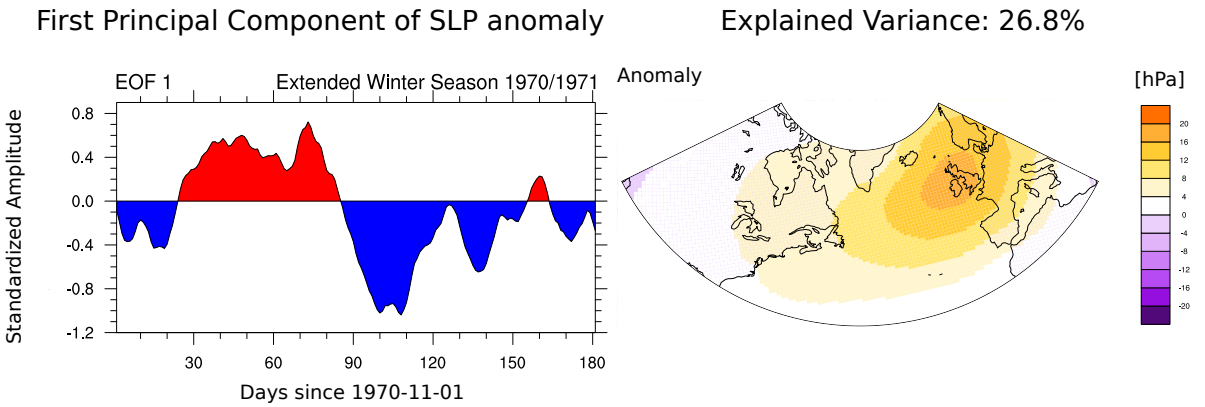

Figure 5.5.: *First EOF of extended winter daily mean sea level pressure from NoN and corresponding PC score time series.*

for ERASSTtVar). It should be mentioned that ERASSTtVar does only contain 20 extended winter season and as the p-value is close to significant, a statistically significant result may be expected for larger sample sizes. Note that for ERASSTtVar, the distribution broadens in the higher latitudes, while for BothN it broadens in the south. This is in line with the findings from section 5.1. BothN has an enhanced blocking frequency in the north, while the enhancement extends down to central Europe in ERASSTtVar.

It remains however unclear as to why the shift is directed towards different directions for the two simulations. We conclude that the enhancement in blocking frequency also has a weak imprint on the distribution of low level jet maxima.

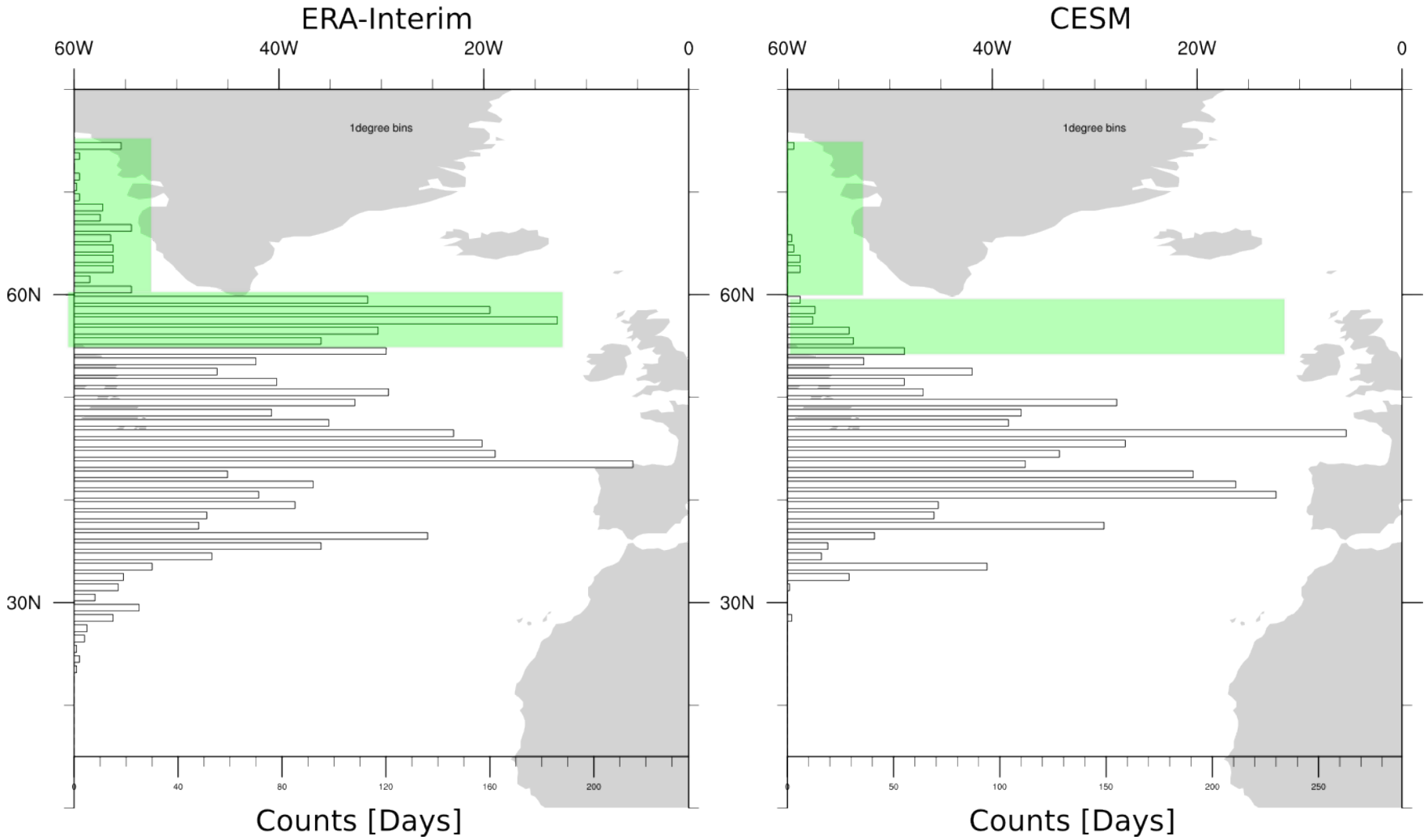

Figure 5.6.: *Histogram plot for low level (925 to 700 hPa) jet maximum as retrieved by the Woollings algorithm [Woollings et al., 2010]. The unit is absolute counts in the simulation (30 years). Magnitude and position of the northern peak and tail of the ERA-Interim histogram are highlighted in green.*

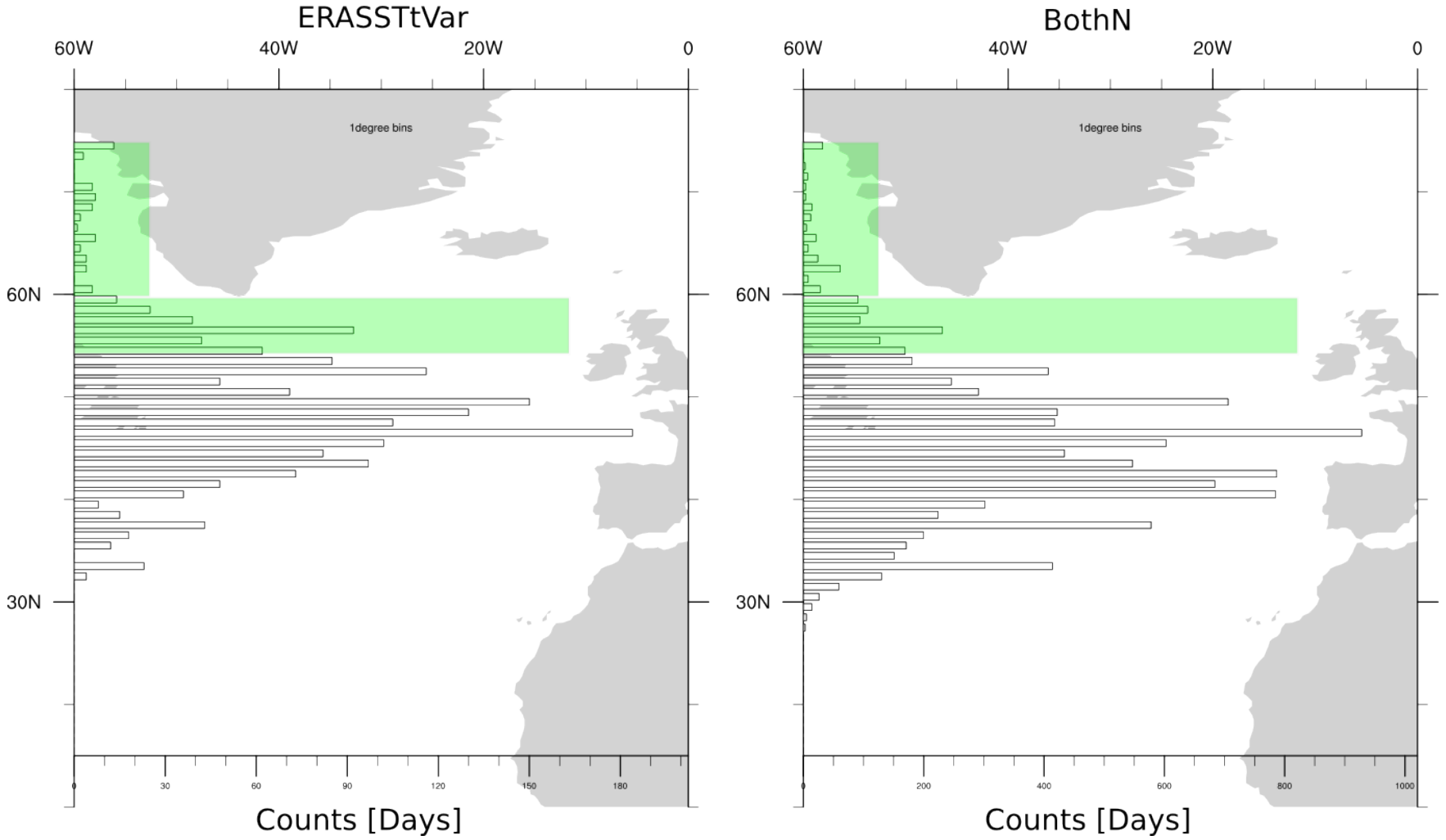

Figure 5.7.: *Low level (925 to 700 hPa) jet maximum histogram plots as retrieved by the Woollings algorithm for ERASSTtVar (left) and BothN (right). The unit is absolute counts in each simulation. For convenience, magnitude and position of the northern peak and tail of the ERA-Interim histogram are again highlighted in green.*

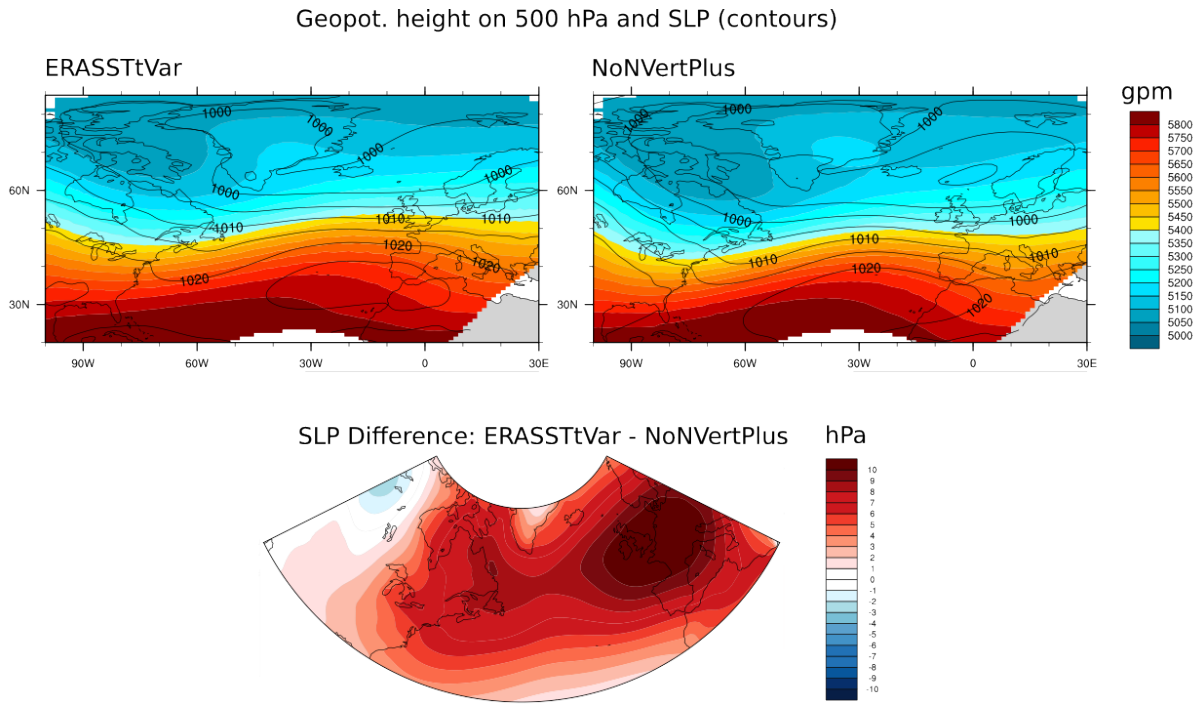

Figure 5.8.: *Top: Mean states (climatologies) in geopotential height at 500 hPa and sea level pressure for ERASSTtVar(left) and NoNVertPlus (right). Bottom: Difference in climatological sea level pressure between ERASSTtVar and the unnested control run NoNVertPlus.*

5.3. Climatology and principal components for the time varying SST simulations

As shown in section 5.1.3, the highest impact on blocking frequency was observed for ERASSTtVar. Higher blocking frequencies should in principle also imply more frequent periods of high pressure in the lower troposphere. We therefore decided to extend our analysis on ERASSTtVar, CoastNtVar and the reference simulation NoNVertPlus by comparing climatologies and variance of the sea level pressure (SLP) fields. The climatology is referred to as the 30 (20 for ERASSTtVar) year mean state of our simulations and an empirical orthogonal function (EOF) analysis on monthly SLP anomalies is carried out in order to find the spatial patterns that explain most of the variance on a monthly timescale.

Imprints of an altered circulation are already visible in the climatologies (Fig. 5.8). In ERASSTtVar, the ridge-like structure in the geopotential height field is broader and extends further northward than in NoNVertPlus (top panels). The ERASSTtVar climatology exhibits overall considerably higher values in the SLP field (bottom panel) and the differences are particularly large around the British Isles and over central Europe. The distribution of pressure and geopotential height in the ERASSTtVar climatology also seems to be somewhat smoother. This signature can be explained by more frequent high pressure systems in the storm track and would then be in line with the findings from section 5.1.3. For CoastNtVar, the climatology is found to be strikingly similar than the one in ERASSTtVar (not shown). Interestingly, it is much closer to the climatology of ERASSTtVar

Simulation	PC 1	PC 2
NoNVertPlus	36.7%	23.6%
CoastNtVar	32.4%	22.5%
ERASSTtVar	33.0%	21.4%

Table 5.2.: *Fraction of explained variance by the first two principle components for all three investigated simulations.*

than to the climatology of the control run NoNVertPlus, even though the runs use different SST fields as lower boundary conditions.

As the climatology does not reveal information on spatial variability, the first two EOF are shown in Fig. 5.9. For each simulation, the fractions of explained variance are given in Table 5.2. The cumulative fraction of explained variance of the first two principal components (PCs) is around 60% for NoNVertPlus and around 55% for CoastNtVar and ERASSTtVar. A sharp drop below 10% fraction of explained variance was found after the first two PCs for all simulations.

The first noticeable feature in all simulations (Fig. 5.9) is the fact that the first EOF does not resemble the typical pattern of the Northern Atlantic Oscillation (NAO) found e.g. by *Hurrell et al.* [2003], with a pressure dipole along the axis Iceland - Azores. This pattern was also retrieved for the boundary driving CESM simulation for the ERA-Interim period by Moritz Pickl (personal conversation, February 2017). In our simulations however, we find monopole structures over the Northern Atlantic and Scandinavia in CoastNtVar and ERASSTtVar and a variability band across the North Atlantic in NoNVertPlus.

The most important difference between our EOF analysis and the one carried out by *Hurrell et al.* [2003] is that our analysis covers the whole outer domain which is not rectangular and covers longitudes between roughly 125°W and 30°E and has a southward extent to 10°N in the easternmost and westernmost regions, whereas their analysis is confined to a rectangular box covering the Atlantic region from 90°W to 40°E and from 20°N to 70°N. When using the same rectangular box as *Hurrell et al.* [2003], the characteristic NAO pattern is retrieved for all simulations (not shown), despite the fact that the box contains missing values in the south-eastern corner. As a PCA within the boundaries set by *Hurrell et al.* [2003] would contain missing values on one hand and would not capture the full SLP variability on the other hand, the analysis is continued with PCAs over the full model domain.

The first two EOFs reveal remarkable differences between ERASSTtVar and CoastNtVar (Fig. 5.9, top left and middle left panels) on one hand and NoNVertPlus (control run, Fig. 5.9, bottom left) on the other hand. For the control run, the first EOF exhibits a monopole structure with large zonal extent ranging from the American east coast to northeastern Europe. This pressure monopole is associated with variability along the storm track. Combined with the information of the PC time series (Fig. 5.9, bottom right), it is found that for NoNVertPlus, the storm track switches from low to high pressure states on a monthly timescale. While the pattern of the first EOFs in

ERASSTtVar and CoastNtVar is still mono-polar, the pressure monopole is more confined to a region over the northeastern Atlantic and Scandinavia. Moreover, the pattern of the first EOF is similar in ERASSTtVar and NoNVertPlus.

For a more direct comparison of the simulations over time, we consider projections of the SLP fields from ERASSTtVar and CoastNtVar to the first EOF of NoNVertPlus rather than the PC time series corresponding to the first EOFs of ERASSTtVar and CoastNtVar. Those projections yield the time series shown in Fig. 5.9, top and middle right. The time series of the projection to CoastNtVar looks similar to the time series of NoNVertPlus, exhibiting high frequency alteration between positive and negative states. The overall high pressure period in the beginning (months one to about twenty) is also present for both CoastNtVar and NoNVertPlus. This high pressure period is not found in ERASSTtVar, but there is a high pressure period from month 70 to 95, which is not found in the other two time series. The relative similarity between CoastNtVar and NoNVertPlus and the difference of the two to ERASSTtVar shows that a noticeable part of SLP variability is steered by Atlantic SST.

More insights may be gained, when considering the second PC loadings. The time series are omitted for the second PC loadings as they revealed fairly balanced positive and negative deviations for all simulations and the amplitudes were comparable to the ones found for the first PC loadings. For ERASSTtVar (CoastNtVar), a negative (positive) state of the second PC does clearly favor the development of blocking events over central Europe. Particularly the large zonal extent may then be interpreted as a large ridge over the North Atlantic, which is one precondition for the formation of blocking events (see section 2.3). For NoNVertPlus, a negative state would rather enhance the strength of the Azores high and shift the low pressure belt a little northward. Hence, the state of the second PC loading would not have such a clear impact on blocking development.

Finally, the time series of both PC loadings for all simulations were found to be virtually uncorrelated amongst each other (which is already visible when considering Fig. 5.9, even though they share the same lateral boundaries). Apart from the potential impacts on blocking frequency, it can therefore be concluded that altering the lower boundaries over the Northern Atlantic has a substantial impact on the structure and amplitude of SLP in the European Atlantic sector and hence on European weather and climate.

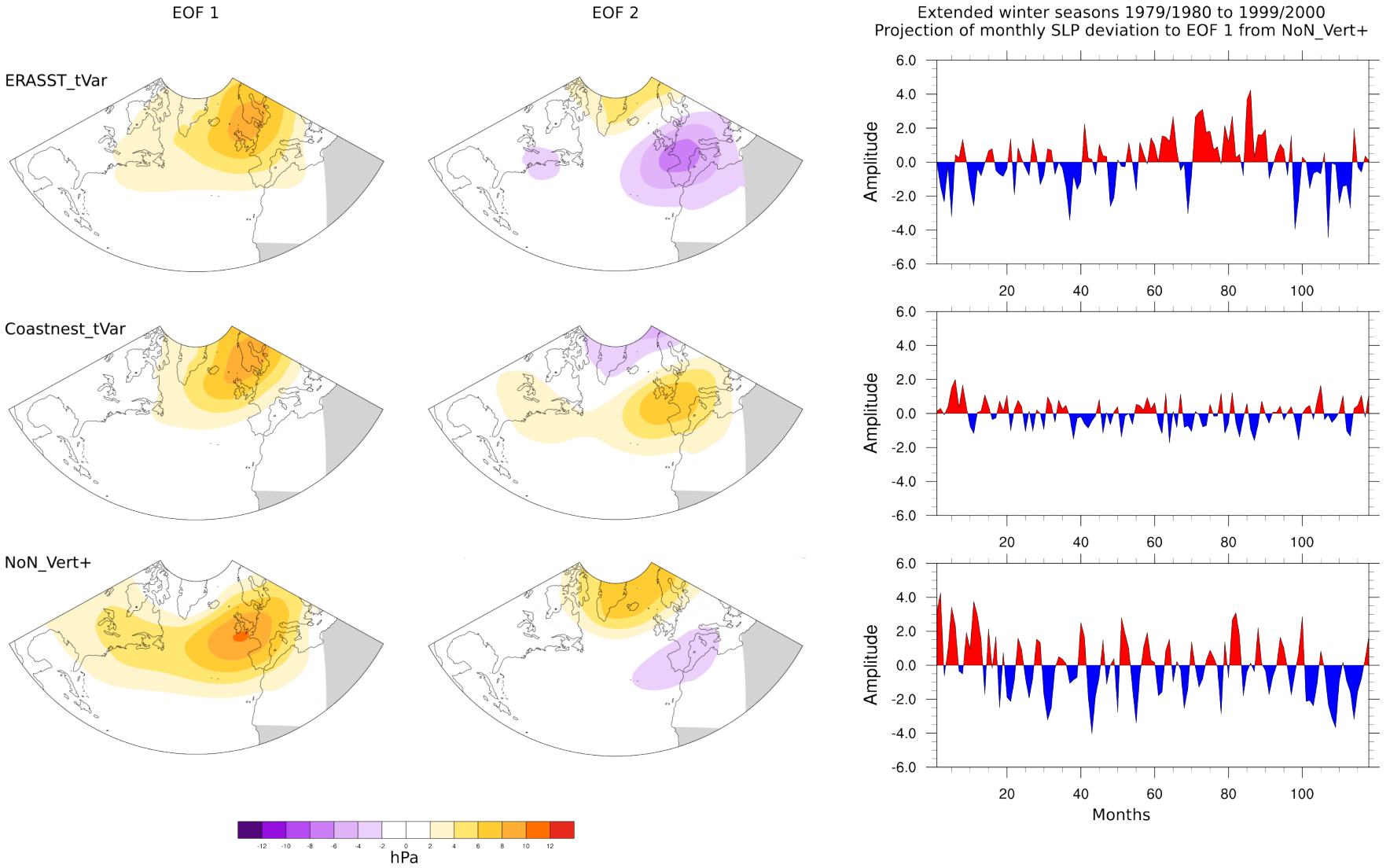

Figure 5.9.: *First two EOFs of monthly SLP (left and middle) of ERASSTtVar, CoastNtVar and NoNVertPlus. Time series (right) for the projection of monthly SLP to the first EOF for NoNVertPlus. For NoNVertPlus (bottom) this corresponds directly to the first PC.*

5.4. Mechanisms for blocking formation in ERASSTtVar

As stated in section 2.3, there is an ongoing debate on the importance of sharp SST gradients for blocking formation. Connected to it, is the question as to how latent heating is connected to blocking events. We aim at specifically addressing this question in the subsequent sections. Two simulations with time-varying SST fields are considered in this section, NoNVertPlus with CESM (1970-2000) SST fields and ERASSTtVar with ERA-Interim (1979-2000) SST fields. Differences in the SST fields are briefly described in section 3.4, particularly in Fig. 3.3. At this point, we recall that the two SST fields were overall in good agreement with each other, but that regionally substantial differences are found. The differences are found to be particularly strong around Newfoundland and the Labrador Sea, as well as in the meridional temperature gradients in the mid-Atlantic region. In the following, we aim at showing the importance of non-adiabatic processes linked to SST for blocking formation.

5.4.1. Composite analysis

To get an idea of the spatial structure and temporal evolution of blocking events in ERASSTtVar and the control run NoNVertPlus, we decided to construct composite events for these two simulations and then compare the composites amongst each other. As the blocking events were tracked over the full WRF domain, we confined the event composites to a smaller area.

Eighteen events detected and tracked by the LAGTRACK algorithm, whose centers remain in a rectangle between 20°W and 20°E and between 40°N and 75°N are selected out of ERASSTtVar. For every selected event, the entire period of the event as well as a period of eight days prior to its first appearance are extracted from the data. For simplicity and to exclude artifacts introduced by diurnal cycles, the time step at 00:00 hour on the day of first appearance was set to time step 0 for each event. This step facilitates an inter comparison of events and/or the calculation of composite means along the new time axis.

As the control run contains substantially more events in the chosen region, the size of the control run composite has to be reduced in order to allow for a reasonable comparison of the two composites. This reduction of composite size is carried out to exclude the possibility that the composite of NoNVertPlus exhibits weaker signals solely due to the fact that it contains more events. To this end, ten composites of $N = 18$ different events were sampled (using the bash random number generator) out of a total of $N_{tot} = 32$ events found in NoNVertPlus. The ten composites obtained this way are compared amongst each other and they do not exhibit large differences (not shown). Finally, out of the ten sampled composites, one is chosen randomly and this composite is subsequently referred to as the control composite or the composite of NoNVertPlus.

For both ERASSTtVar and NoNVertPlus, an extended winter climatology (the mean state over this time period) is calculated. For latent heat flux and 500 hPa geopotential height, the climatology was subtracted from the composite mean to get a clearer picture of the anomalies involved in the events. The 500 hPa and PV fields of the NoNVertPlus composite are compared to the fields of the ERASSTtVar composite. The top two panels of Fig. 5.10 show the composite means on the

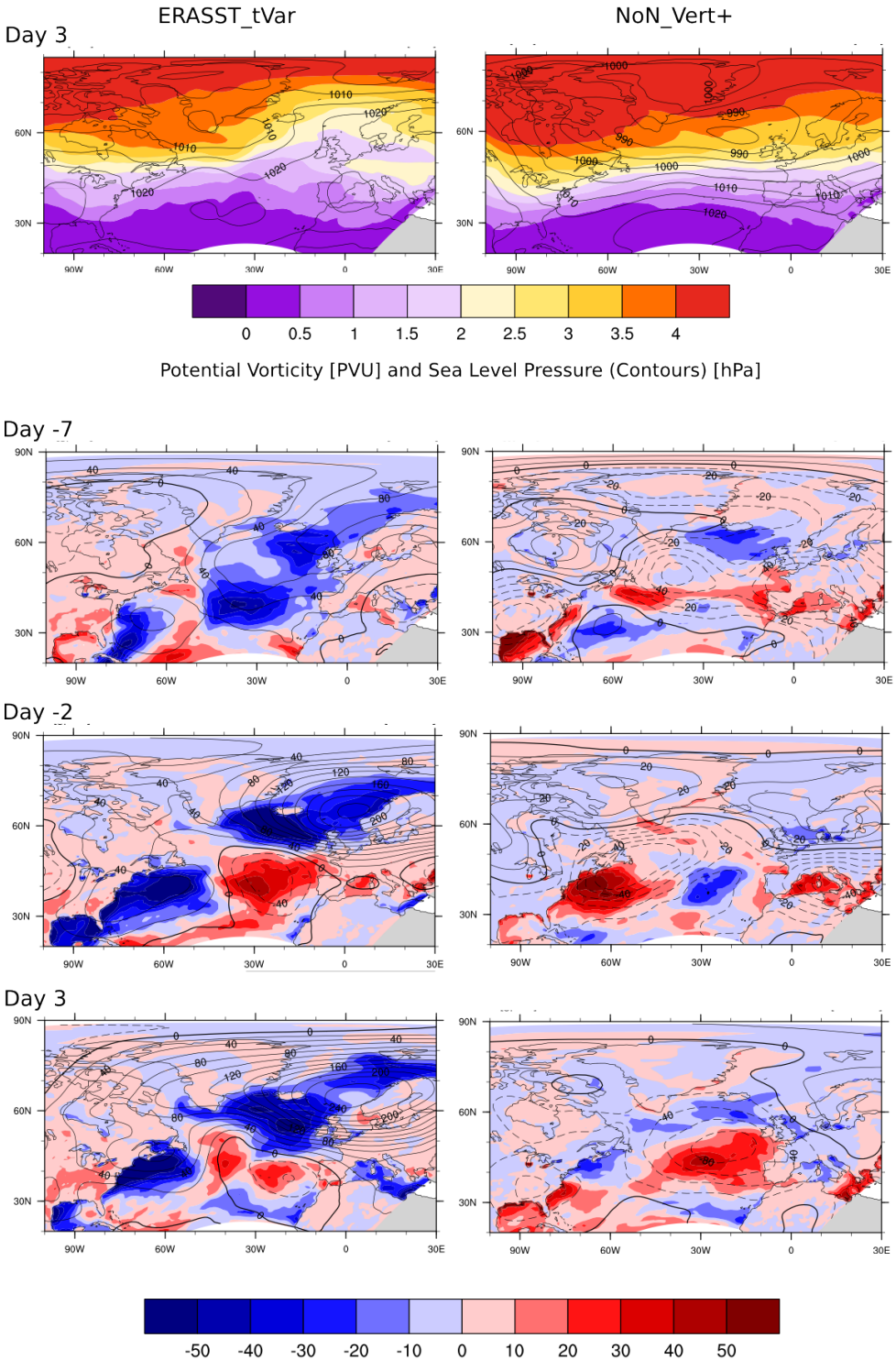

Figure 5.10.: *Composites of ERASSTtVar (left) and NoNVertPlus (right). The top two panels show the composite three days after the blocking onset. The lower six panels show the deviations of the composites from their respective climatologies. In these six panels, the temporal evolution is shown from top to bottom at days seven and two prior to the blocking onset and day three after its onset.*

third day after onset at 12:00 UTC. The imprint of the blocking event on potential vorticity and 500 hPa geopotential height is evident for both composites, but the imprint on potential vorticity is stronger for the ERASSTtVar composite. The lower six panels show the temporal evolution of the two composites during the onset period and on the third day after the events were first captured by the LAGTRACK algorithm.

Interestingly, we observe a strong latent heating anomaly in ERASSTtVar slightly upstream to the forming high pressure system during the onset period (i.e. on day -2). The heating coincides with a weak low pressure anomaly. It is not evident from the data alone, whether the low pressure anomaly (and the corresponding heating) is an artifact of the highly meridional flow pattern or whether it contributes actively to the formation and stability of the blocking event. Recalling the findings of *Pfahl et al.* [2015], we speculate that the heating anomaly has a strong impact on the downstream blocking event. This does of course not exclude the possibility that there might be a feedback mechanism, where an emerging block amplifies an upstream low, which in turn amplifies the block by intrusion of low PV air to the upper troposphere. The described mechanism will be further investigated in the case study following in the next section. Note, that the heating anomaly is weaker and not clearly located upstream in the NoNVertPlus composite.

Although the center of the high pressure anomaly in the 500 hPa field is located at similar points for both simulations (Fig. 5.10, bottom panels), the composites exhibit strong differences in their strength and character. Most strikingly, the composite anomaly in ERASSTtVar has a center strength of 240 gpm compared to about 20 gpm in NoNVertPlus. This could be due to three reasons: Either the blocking events in NoNVertPlus are weaker, they are more evenly distributed in the investigated area or a combination of the two. Another key difference is the imprint of the blocking events on the dynamical tropopause (here the intersection of the 2 PVU line with the $\theta = 315$K surface) shown in the top two panels. In the ERASSTtVar composite, the dynamical tropopause is shifted far northward at $\approx$0 degrees longitude and it even exhibits a cutoff-like structure. In NoNVertPlus, there is no such feature found in the dynamical tropopause. This is evidence for different underlying mechanisms in the events that form the two respective composites. On one hand, in NoNVertPlus, the events detected are lower level features that are just strong enough to leave their imprint on the 500 hPa surface. On the other hand, in ERASSTtVar we see a clear upper level feature, where there must have been production or advection of low PV air in the upper troposphere. This is particularly interesting as for the events found in NoNVertPlus, tails of the Polar (and Siberian) high are sufficient to produce the observed imprint, whereas for the events in ERASSTtVar this is clearly not the case.

A further feature to be shown at this point, is the impact of the altered SST field on the extended winter climatology. Consider the mean distribution of latent heating (Fig. 5.11). Surprisingly, the heating seems to be somewhat stronger in NoNVertPlus than in ERASSTtVar for most areas. In a very heuristic view, this would imply more available energy for instabilities to grow and hence more intense high- and low pressure systems. However, more blocking events are found in ERASSTtVar (Fig. 5.2). There are other striking differences in the mean distribution of latent heating when

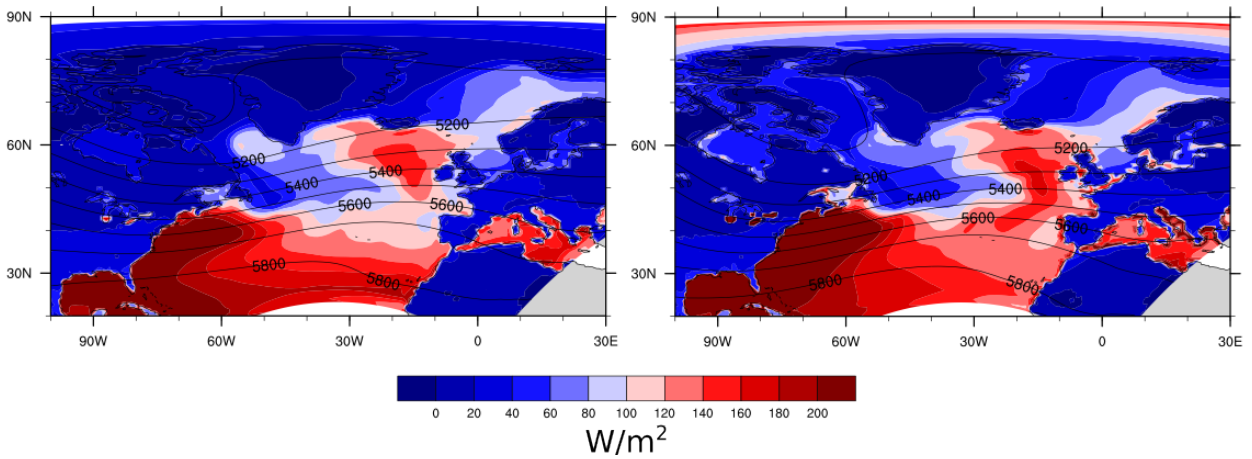

Figure 5.11.: *Average latent heating and geopotential height (contours) calculated from ERASSTtVar (left) and NoNVertPlus (right). Geopotential height contours are given in meters.*

comparing ERASSTtVar to NoNVertPlus. In the former, the gradient seems to be more meridional oriented, in particular between 35°N and 45°N. Additionally, the belt of strong latent heating offshore the American east coast is more confined in ERASSTtVar than in NoNVertPlus. We argue that the strong meridional gradient described above is located too far south, to be important to the blocking itself. But when comparing the composites in Fig. 5.10, the upstream cyclone in the ERASSTtVar composite forms exactly, where the mean latent heating in ERASSTtVar exhibits a strong meridional gradient and NoNVertPlus does not. The formation of an upstream anticyclone is presumably a crucial feature of European blocking, as we already discussed in section 2.3.

5.4.2. Case study of a blocking event

The co-appearance of a cyclone upstream to the blocking in ERASSTtVar raises the question, whether there is an interaction between the cyclone and the blocking and what the nature of this interaction might look like in terms of potential vorticity advection to the blocking. As a the signal of the interaction may be somewhat blurred in the composite, we decided to carry out a case study on an individual event extracted from the composite.

A three day event with a center over Central Europe was identified by the LAGTRACK (section 4.2) algorithm in the ERASSTtVar simulation, this event is also part of the ERASSTtVar composite in the previous section. In the simulation, it lasted from April 5 at 18:00 to April 8 at 18:00. Over this period, the center of the blocking traveled slowly westward from 7.5°E to 6.25°W. Thereby the center stayed at relatively constant latitude between roughly 46°N to 50°N. The cumulative gradient (equation 4.2) of the 500-hPa geopotential height field intensifies up to a maximum of 55 gpm per degree latitude.

A quasi-stationary upstream low goes along with the event. Note, that this low pressure system is already present prior to the event (Fig. 5.12). Considering the temporal evolution over the last 18 hours prior to the event, the contribution of this low pressure system to the formation of the block is evident. Starting from a meridional flow, the strong low pressure system further advects low PV

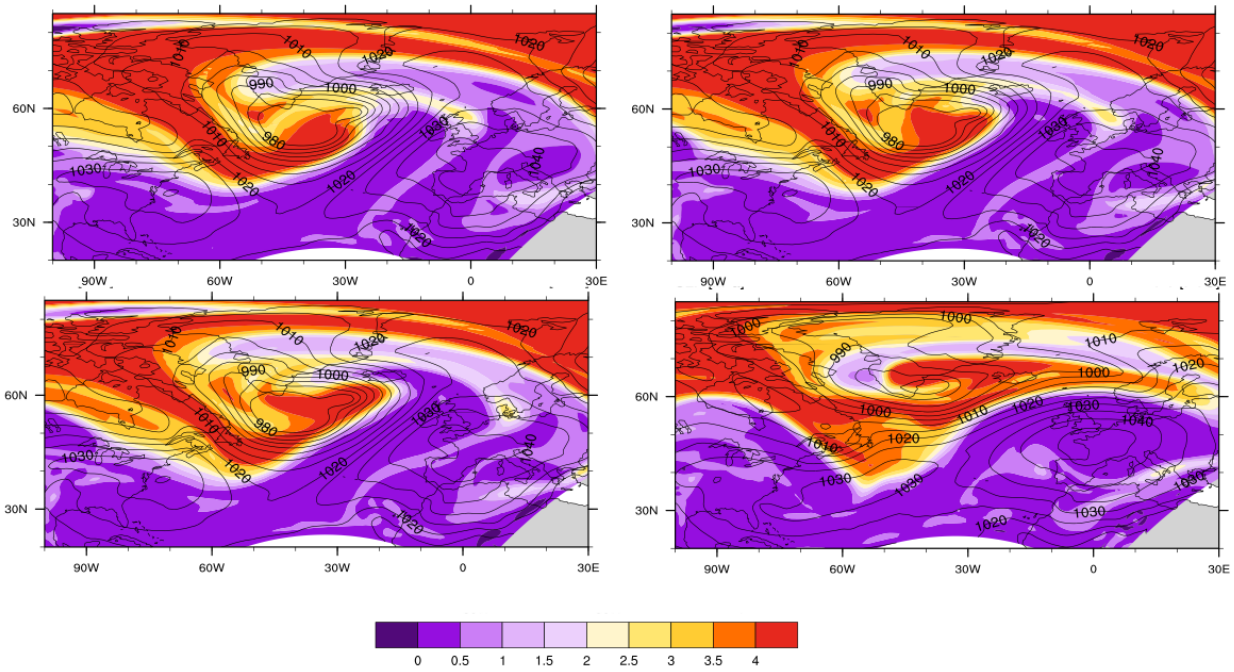

Figure 5.12.: *Synoptic situation during a blocking event found in ERASSTtVar. PV distribution on the $\theta = 315$ K surface and sea level pressure. The first three panels (top left to bottom right) show part of the evolution during the onset on April 5, from 00:00 UTC to 12:00 UTC in six hour steps. In the bottom right panel, the mature event is shown 30 hours later on April 6, 18:00 UTC.*

air to the ridge and causes an amplification. This is clearly seen in the top three panels on the left of Fig. 5.12, where the northwestward flow of low PV air in the upper troposphere ($\theta = 315$ K) is shown. This flow causes anticlyclonal wave breaking and with it the formation of the block, as can be seen in the bottom right panel, where the imprint of the mature blocking event on geopotential height and potential vorticity is shown. The location of the dynamical tropopause (2 PVU line) indicates a highly meridional flow during the onset and over the lifetime of the event.

The transport of low PV air does not happen mainly due to horizontal advection, but it is rather found that vertical advection plays a major role. The cross section on the left panel of Fig. 5.13 shows a warming of the upper troposphere at around 15°W. On the cyclone's front, high vertical velocities reveal the transport of warm, low PV air masses to the upper troposphere. The dynamical tropopause is thereby already lifted to about $\theta = 330 - 340$ K. Fig. 5.13, right panel reveals the vertical transport of low PV air at that height. It is found that the major contribution to total PV tendency (not shown) is due to the strong vertical advection of up to -2 PVU/hr. This finding further supports the view, that latent heating and the subsequent vertical transport of low PV air is crucial to the formation of blocking events. Hence, the ability of a model, to reproduce the high baroclinicity found offshore the American east coast is likely to be connected to its ability to accurately capture blocking in the Euro-Atlantic sector.

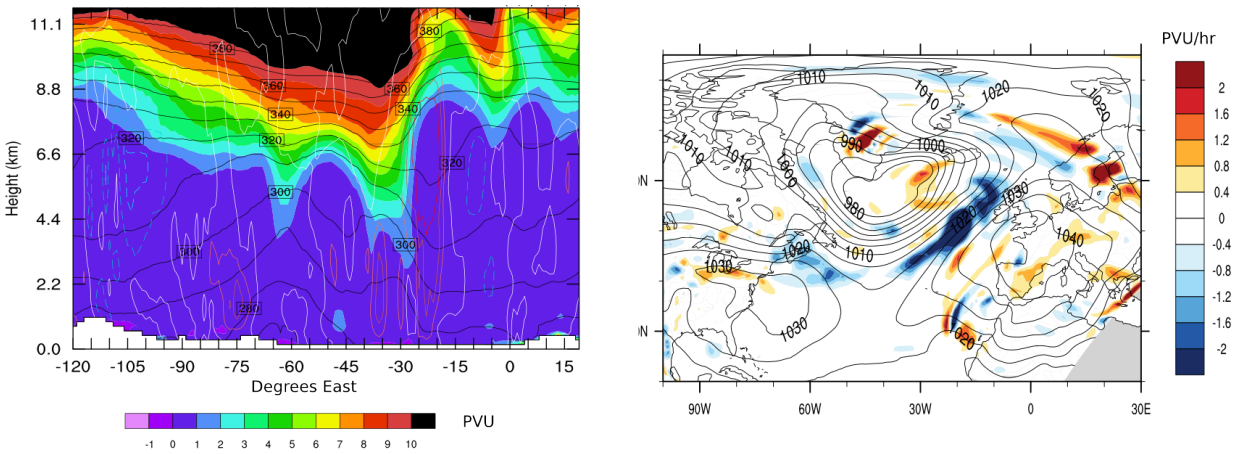

Figure 5.13.: *Left: Vertical cross-section of potential vorticity and potential temperature along 50° N on April 5, 12:00 UTC. (top right panel) reveals the heating in the upper troposphere downstream to the cyclone located south of Greenland and the lifting of the dynamical tropopause. Right: Vertical PV advection to the $\theta = 330$ K surface which coincides roughly with the dynamical tropopause at around 15° W at that instance.*

5.5. Baroclinicity for different setups

In the previous two sections, we identify baroclinic processes as an important contributor to blocking formation. Conversely increased blocking frequencies would cause increased static stability in a climatological sense. To investigate the baroclinic instability in our experiments, eady growth rates (see equation 2.2.5) are calculated and averaged over a thirty (twenty for ERASSTtVar) years period. As introduced in section 2, Eady growth rate is a suitable measure for the growth of baroclinic disturbances.

A selection of experiments is shown in Fig. 5.14. While in principle, the simulations on the left should not be compared to the simulations on the right (time-varying vs. constant SST fields), it is nevertheless stressed that the EGR magnitude differs substantially. This difference is likely to be attributed to time-varying SST input. We will hereafter discuss the differences ERASSTtVar - NoNVertPlus and BothN - NoN.

The storm track at the 850-hPa level is substantially less baroclinic in ERASSTtVar than in NoNVertPlus (Fig. 5.14, left). This difference can partially be attributed to a change in the Brunt-Vaisälä frequency N^2, as the unstably stratified region is slightly larger in NoNVertPlus. It is also assumed that horizontal temperature gradients have an impact on EGR, especially off the American coast and in the mid-Atlantic. On the 850 hPa level, SST contribute substantially to air temperature and it therefore seems plausible, that an altered SST field has a dramatic impact on horizontal temperature gradients and hence on Eady growth rates.

Increasing horizontal resolution increases Eady growth rates at the 850-hPa level (Fig. 5.14, right) in and downstream to the nested regions in BothN. It can only be speculated about possible reasons for this behavior. The higher resolution of about 30 km in the nests is closer to the length scale, for which the model was originally designed. It is therefore possible that convective processes are not

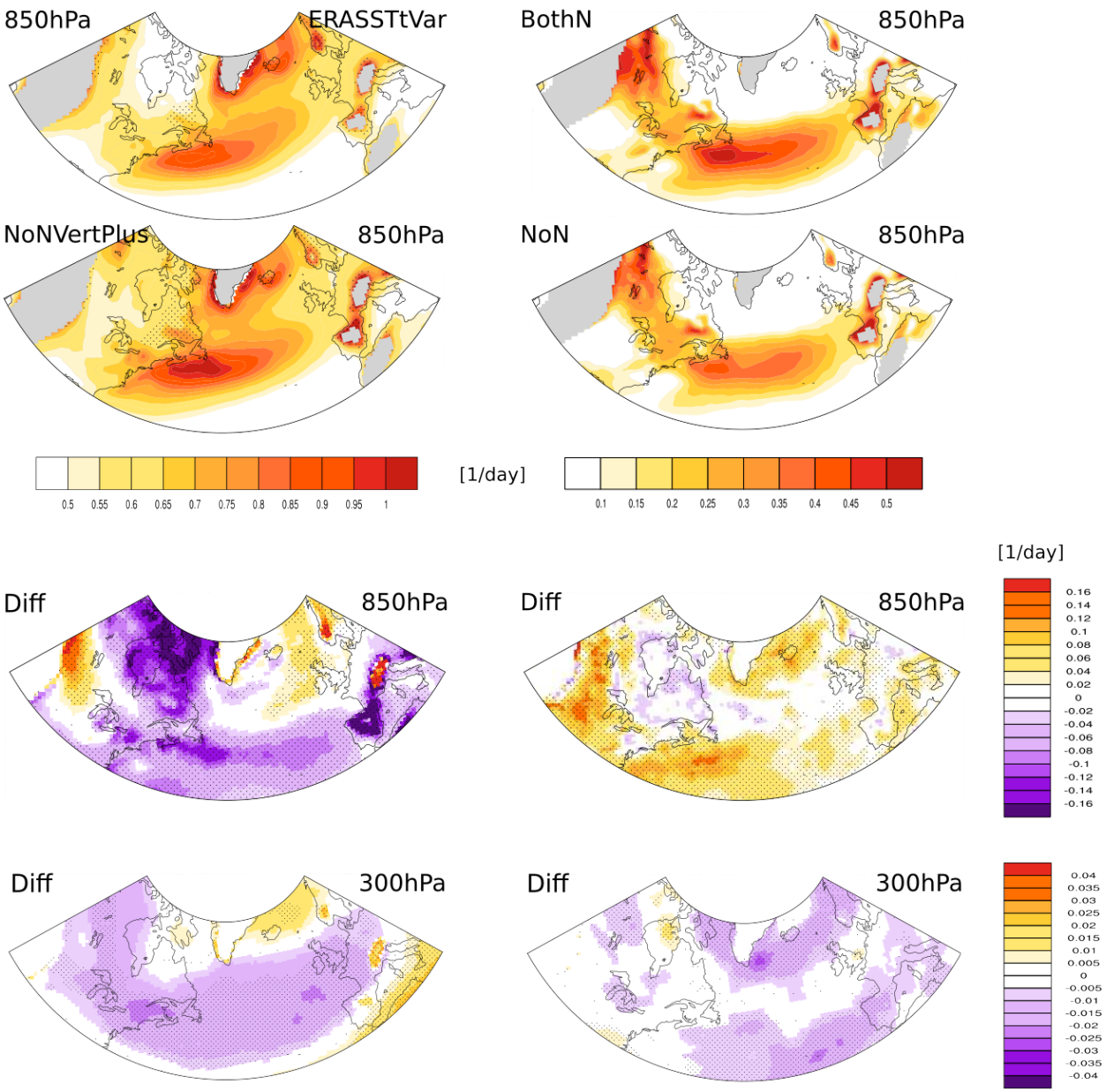

Figure 5.14.: *Top four panels: Eady growth rates for ERASSTtVar, BothN, NoNVertPlus and NoN, stippling indicates regions, where the atmosphere is unstably stratified ($N^2 < 0$). Bottom four plots: Differences (ERASSTtVar - NoNVertPlus, left) and (BothN - NoN, right) at 850 hPa and 300 hPa. Stippling indicates regions, where the differences are significant on a 95% significance interval (Two-sided Mann-Whitney-U test). Note that in the top four panels, the scales for left and the right panels are different.*

only better resolved, but the model physics might as well work better in this range.

Changes at the 300 hPa level are found to be smaller in magnitude, but they are nevertheless coherent over large spatial extents. Eady growth rates are lower in ERASSTtVar than in NoNVertPlus for both 850 hPa and 300 hPa. This indicates increased stability along the storm track in the climatological mean. Note, that this seems to be somewhat contradictory to the statements in sections 5.4.1 and 5.4.2, where cyclone activity upstream to a blocking is identified as an important contributor to blocking formation. It should be stressed that there is not necessarily a direct connection between Eady growth rates and blocking events, as blocking events have a typical length scale of $\mathcal{O}(10^4)$ m, while the Eady growth rate is a measure for the growth of the most unstable mode in the mid-latitudes, which lies around 5500 km [*Lindzen and Farrell*, 1980]. Therefore, two possible connections between Eady growth rates and atmospheric blocking are suggested: On one hand, elevated Eady growth rates can be an indication of stronger cyclones, which can in turn provide low PV air to upstream blocking events. On the other hand, lower Eady growth rates are an indication of increased stability and might point towards more frequent anticylonic flow regimes.

For the difference between BothN and NoN, the differences in the respective pressure levels yield opposing signs. Compared to NoN, BothN exhibits higher Eady growth rates in the lower troposphere, but lower Eady growth rates in the upper troposphere. Hence, the baroclinic stability of the upper atmosphere increases with horizontal resolution, while the baroclinic stability of the lower troposphere decreases with increasing horizontal resolution. The interpretation of this signal is somewhat unclear and would certainly require a more throughout investigation. However, this is not in the scope of this thesis.

Note that all differences shown in Fig. 5.14 are statistically significant over large areas. This is clear evidence for the fact that resolution and lower boundary conditions alter the dynamics of the lower troposphere. Interestingly, the effects of increased horizontal resolution and altered SST are adverse concerning Eady growth rates in the lower troposphere, but for both experiments an increase in blocking frequency was found. Therefore, the connection between Eady growth rates and blocking frequencies remains unclear.

6. Summary and Conclusions

Atmospheric blocking in the European-Atlantic sector is still severely underestimated in state of the art climate models. It is shown that the Community Earth System Model is no exception and exhibits a considerable underestimation of blocking frequencies in the eastern Atlantic and around the British Isles. Although the misrepresentation of atmospheric blocking in climate models is a long-standing problem in climate modeling, the underlying reasons for this misrepresentation are not conclusively clear. This thesis aims at investigating the importance of horizontal resolution and accurate SST fields to blocking formation in climate models. A new approach to the problem is presented by using the regional climate model WRF to increase horizontal resolution over limited areas and by exchanging SST fields in the model boundaries.

A series of downscaling experiments with WRF is carried out in order to assess the impacts of different configurations of the model on blocking frequencies. Apart from ERASSTtVar, all simulations cover a thirty year period from June 1, 1970 to June 30, 2000, ERASSTtVar covers a 20 years period from June 1, 1979 to June 30, 2000. The boundaries are driven by the corresponding 30 year extracts from a transient CESM simulation from 850 to 2100 A.D., which is carried out at the Climate and Environmental Physics division by *Lehner et al.* [2015].

In total, seven different simulations are carried out, of which one (CoastN) is discarded as an updated version of it (CoastNtVar) is carried out later. The simulations can be divided into two subsets: One subset contains simulations with constant SST (NoN, RockyN, CoastN and BothN), in the other subset, the simulations are driven by time-varying SST (NoNVertPlus, CoastNtVar and ERASSTtVar). Note, that the experiments in the second subset also contain ten more vertical levels. Hence, the experiments within one subset are comparable, but shall not be compared to experiments of the other subset. In both subsets, the respective control runs (NoN and NoNVertPlus) exhibit similar blocking frequencies as are found in CESM. This leads to two inferences: First, increased vertical resolution did not alone lead to a substantially better representation of blocking frequencies. Second, NoN and NoNVertPlus are suitable control runs for the rest of the experiments.

Both subsets contain simulations which make use of WRF's two-way nesting option. The principle of nesting is that information can travel from a coarsely resolved outer domain to a better resolved nest. In two-way nesting, information from the nest is then also allowed to flow back to the coarse domain. This feature is used to investigate the impact of locally enhanced horizontal resolution over areas that are believed to be of importance to blocking formation, the Rocky Mountains and the American east coast. RockyN, BothN and CoastNtVar are simulations dedicated to different nesting experiments, while in ERASSTtVar, the basic idea is to incorporate more realistic SST fields without enhancing the resolution of the model itself. Note, that replacing SST fields introduces an

inconsistency between lower boundary conditions and lateral boundary conditions. However, the noise at the boundaries of the simulation is not found to be stronger than in the two-way nesting experiments.

A Lagrangian tracking algorithm (LAGTRACK) developed by *Blender et al.* [1997] and then adapted to track anticyclones on the 500 hPa level by *Buehler* [2008] is further developed such that it is now capable of counting events within a radius given by a Gaussian fit around the center of the anticyclone. This algorithm is then applied to our simulations after interpolating them to a common grid of $1.25° \times 0.9°$ (same as the CESM run). The output is a field with blocking frequencies (fraction of blocked timesteps to total timesteps) for each grid point. Blocking frequencies are also derived with a second, more simple algorithm (TIMO) introduced by *Scherrer et al.* [2006], which is based on a one-dimensional index first introduced by *Tibaldi and Molteni* [1990].

Overall, the LAGTRACK method captured the details of the spatial distribution in blocking frequencies better than the well-established TIMO method. Using LAGTRACK, blocking frequencies are found to be lower than in the literature. This may be due to a conservative estimation of spatial extent. Both methods agree reasonably well on the spatial distribution of blocking frequencies.

Although the results obtained from both indexes are statistically not significant, remarkable differences in blocking frequencies in the respective simulations are found. In the nesting experiments, the enhancement is found to be strongest, when simultaneously increasing horizontal resolution over the American east coast and over the Rocky Mountains (BothN). Even stronger impacts on blocking frequencies are found in the simulations with time-varying SST input. Here, a strong increase in blocking frequencies is observed when replacing the CESM SST fields with ERA-Interim SST fields for the same period. Additionally, for ERASSTtVar and CoastNtVar, a significant southward shift of blocking event latitude (as retrieved by the LAGTRACK algorithm) is found.

The distribution of low-level jet maxima [*Woollings et al.*, 2010] is found to deviate clearly from the respective control simulation for BothN and ERASSTtVar. For ERASSTtVar (BothN), the the northern (southern) tail of the distribution is heavier than in the respective control run. As, by definition, blocking events split or shift the maximum of the low-level jet, this result further supports the above finding that more blockings occur in BothN and ERASSTtVar. Again, the results are found to be statistically not significant.

Surprisingly, the typical NAO pattern [*Hurrell et al.*, 2003] in sea level pressure (SLP) is absent in the first principal component of the monthly SLP field. This is due to the fact that the PCA in this analysis is carried out over a different domain. The first two principal components explain most of the variance in all investigated simulations. The patterns in ERASSTtVar and CoastNtVar are found to be strikingly similar and differ clearly from the control run NoNVertPlus. The temporal behavior is also found to be different in the considered simulations. Combined with a slightly shifted climatology, it is argued that again ERASSTtVar is more often subject to high pressure over western Europe and the eastern Atlantic. This finding is in line with the enhanced blocking frequency in ERASSTtVar.

Composite analyses of blocking events are constructed with the information retrieved by the LAGTRACK algorithm. When investigating composites of blocking events restricted to a limited area over the eastern Atlantic and western Europe, two important differences between events in ERASSTtVar and NoNVertPlus are found. Firstly, it is shown, that the ERASSTtVar composite has a clear signature in the mid- to upper troposphere, while this is not the case for NoNVertPlus. Secondly, the events in ERASSTtVar go along with upstream cyclones and latent heating. Thereby, cause and effect could not be disentangled and it remained unclear whether the cyclone amplified the blocking or whether the blocking induced the upstream cyclone. However, one can speculate that probably both is true and the much stronger latent heating in ERASSTtVar may be connected to enhanced blocking frequencies as latent heating is identified as a key factor for blocking formation in the literature [*Pfahl et al.*, 2015]. The role of latent heating is further investigated in a case study, where the lifting of air masses downstream of a cyclone could be connected to a subsequent blocking event.

The importance of latent heating and advection of low PV air to the upper troposphere is then further illustrated in a case study. Combining horizontal PV and geopotential height fields with vertical cross-sections and the PV tendency equation[*Wu and Wang*, 2000], it is shown that there is substantial upward motion of air masses at the back of a strong cyclone located over the Atlantic. These air masses then entered an already present ridge in the upper troposphere and eventually caused anticyclonal Rossby wave breaking and a mature blocking event over western and central Europe.

The connection of latent heating and blocking events then led to the investigation of baroclinicity in the different simulations, where it is stated that all investigated simulations show significant differences from their control simulations in average Eady growth rates [*Lindzen and Farrell*, 1980]. It is concluded that both nesting and differences in the lower boundary conditions have an impact on the dynamics of the lower troposphere, however the differences in Eady growth rates could not be directly linked to blocking events.

In conclusion, increasing horizontal model resolution over key areas (Rocky Mountains, coast of Newfoundland) has a clear impact on the downstream dynamics and on blocking frequencies in the European Atlantic sector. Furthermore, changes in the SST fields have an even stronger impact on blocking frequencies and the related dynamical quantities. Even if the changes in blocking frequencies are found to be statistically not significant - probably due to large inter-annual variability - the overall picture found in this analysis, reveals that the representation of blocking events in climate model is closely connected to a correct representation of Atlantic SST. However, as both increased resolution and changes in SST fields lead to more realistic blocking frequencies in our experiments, it still remains unclear, how in practice, a better representation of atmospheric blocking can be achieved in climate models and further research is needed to find combinations of lower boundary conditions and horizontal resolution leading to a more realistic representation of atmospheric blocking in the Euro-Atlantic sector without requiring too much additional computational effort.

7. Outlook

We show that both increasing horizontal resolution and using more realistic SST fields in the lower boundary conditions lead to a slightly better representation of atmospheric blocking in climate models. As blocking events are relatively rare (consider e.g. Fig. 5.1, top panels) and probably not always captured with the two indices we used, long time series are needed to establish reasonable blocking climatologies. One obvious step is the extension of our simulations to 50 or even 100 years or to run ensembles with random perturbations in the boundary conditions. Given the relatively coarse resolution of our simulations, both could be achieved with reasonable computational effort. This step is particularly urgent for ERASSTtVar, which currently only covers a 20 year period. To obtain higher blocking frequencies, it is also conceivable to try different combinations of two-way nesting and altered SST forcing.

To get more confidence in the blocking frequencies retrieved by the LAGTRACK algorithm, it may be beneficial to compare it to other event-oriented indices based on potential vorticity (see e.g. [*Pelly and Hoskins*, 2003; *Schwierz et al.*, 2004]) rather than geopotential height. Although blocking indices based on different fields have been shown to be generally in good agreement (i.e. they capture similar spatial distributions of blocking frequencies) [*Scherrer et al.*, 2006], it is expected that a throughout comparison of the LAGTRACK algorithm to other approaches can further reveal its strengths and weaknesses. This may answer the question, why unrealistically low blocking frequencies are found with the LAGTRACK algorithm and how this shortcoming may be addressed.

As mentioned in section 3.4, WRF ARW is a mesoscale atmospheric model by design. Given the nonlinear scaling in many fluid dynamics systems, it is not clear, whether all chosen parameterizations are still suitable for planetary-scale motion. Note that this problem is currently being addressed in both climate modeling and numerical weather prediction (e.g. *Schemann et al.* [2013]), as a new generation of GCMs (e.g. ICON [*Wan et al.*, 2013]) are required to be capable of running simulations at a wide range of temporal and spatial scales. It would therefore be interesting, to use a GCM with nesting capabilities and repeat our experiments in such a setting. However, this approach would require a considerable computational effort. One could also think of a simpler experiment without nesting. Given the fact that Atlantic SST seem to play a crucial role to blocking formation in the European Atlantic sector, one could come up with an experiment, where a GCM is nudged with more realistic SST fields.

In Fig. 3.3, it is shown that the mean state of Atlantic SST in CESM differs substantially from mean SST in the ERA-Interim reanalysis data set. This does not necessarily imply that the model misrepresents Atlantic SST in general, as a part of Atlantic SST variability may certainly be attributed to internal variability of the Atlantic Ocean (e.g. to the Atlantic Multidecadal Oscillation

(AMO), [*Schlesinger and Ramankutty*, 1994]). The internal variability of the model and the actual climate system are thereby not necessarily in phase. Given the importance of Atlantic SST to blocking formation, a part of the underestimation of blocking frequencies may therefore also arise due to the misalignment of internal variability of the Atlantic Ocean. Thus, it would also be interesting to identify periods in a long coupled GCM simulation, where the SST pattern is closer to the one found in the reanalysis data and to check whether blocking frequencies are higher during this period. The idea that a misalignment of internal variability between model and actual climate system may lead to differences between observations and model projections has already lead to a study carried out by *Huber and Knutti* [2014], where the authors aimed at finding an "internal variability analogue" to the recent hiatus in a GCM.

In conclusion, many of the research ideas developed above can be tested with reasonable effort and the subject clearly requires further attention by the climate modeling community, as there is still a considerable bias of blocking frequencies in state-of-the-art GCMs.

A. WRF best practice

As WRF ARW is used extensively in this thesis, some of the pitfalls encountered are presented on the next few pages. By no means does this section aim at replacing parts of the WRF ARW tutorial. It is rather an (incomplete) description of problems that may arise when working with WRF. This document may serve WRF users as an additional source of information for running WRF with a special focus on simulations covering large domains with GCM input data. In this study, the used platform is the University of Bern Linux cluster for high performance computing (UBELIX).

A.1. Compilation on UBELIX

Prior to compiling WRF ARW, you will need to compile a few other libraries as WRF ARW relies on them. These libraries are (currently) listed on the WRF ARW user page. Make sure, you follow the instructions on this web page. As you will not be able to install the libraries in shared folders such as `usrlib`, `usrlib64`, etc., it is recommended that you create a folder in your home directory, where you install local versions of these libraries. Note that WRF ARW will not compile, if the libraries it depends on are not compiled with the same compiler. Therefore, you should stick to your choice of compilers (`Fortran`, `C`, `C++` and MPI accelerator). Some libraries may already be compiled on UBELIX, however, if you can not find out, with which compiler they were built, it is safer to install your own versions. Once all libraries are built, you will have to export the `netCDF` path variable. Additionally, you will have to double check and correct the library paths in the config files for both WRF and WPS.

Once all libraries are built and have passed the test on the above cited web page, you can proceed by compiling WRF and WPS. If you get error messages, always fix the first one that occurs and then restart the compilation, as subsequent error messages may arise due to the fact that modules further above could not be compiled. It is recommended that you compile WRF for distributed memory and WPS for serial use. In this study, we use PGI compilers for `Fortran`, `C` and `C++` and the OpenMPI parallel accelerator.

A.2. Hints for WPS

WPS is the WRF preprocessing software. Most of the available options can be set in `namelist.wps`, but for some additional options you may have to make changes in `METGRID.TBL`. I.e., the following problem may arise if you use course resolution input data (for a mesoscale model, any GCM input will be coarse resolution): WPS will generate a landmask (distinction between land and water grid points) based on the geographical data you download from the WRF ARW user page. However,

your input data may have a completely different landmask. Make sure you provide the landmask of your input data to the interpolation options (in `METGRID.TBL`) of your SST and soil fields as you will get unrealistic values otherwise. It should also be mentioned that omitting this step will not result in error messages from WPS, but either the vertical interpolation in real will crash or you will see unrealistic features in the WRF model output.

Take your time to properly set up a reasonable domain for your purposes, as it is always cumbersome to change the domain again once the model runs. Make sure to include as little complex topography in your boundaries as possible. If your outer domain has a relative course resolution, you can add a few grid points without worrying about model performance, as the main computational burden will arise in the highly resolved nests.

If it is not possible to exclude complex topography from the boundaries, you can apply four- to sixteen point average smoothing to the topography field. The smoothing option and the number of smoothing iterations can be set in `METGRID.TBL`. You may still run into troubles with metgrid, when you preprocess a large domain over several years. It is possible that the horizontal interpolation goes wrong at some point. In this case, first make sure your input data is fine, if this is the case, try to make adaptions to the interpolation options of the variables in `METGRID.TBL`

Make sure you use the right Vtable. This table serves as a dictionary between the Grib code of your input variables and the variable names, which will be set in ungrib. If you use CESM output, you will need to use a custom Vtable, for instance the one created by Juan - José Goméz Navarro, PhD.

Once you have run metgrid, carefully check the output `met_em` files. If they are corrupted, real or WRF will crash without giving you obvious hints on the source of your problems. Make sure your SST data does not have strange features close to coast lines, as this indicates that you are providing the wrong landmask to metgrid. After checking your `met_em` files, you can proceed with the vertical interpolation carried out by real.

A.3. Troubles arising in real

If real crashes, the reason is most likely not to be found in the settings for real, but it may be a hint that your `met_em` files are corrupted. Especially, if you get an error of the form “could not find trapping x values”, the reason will most likely be, that real is trying to extrapolate meteorological fields to sea level height, while in your `met_em` files, this grid point is over land and may have a non zero elevation. Again these kind of errors arise, when using the wrong landmasks. Vice versa, the same error arises, when real tries to process soil data, when in your `met_em` soil files, this grid point is in the sea.

A.4. Running WRF

One of the major challenges as a new WRF user is to deal with a large number of namelist options and to find out which namelist switches are important to your work and then which options you

should choose. Do not try to build a namelist from scratch. It is recommended that you start with an example given on the WRF ARW user page or that you use a namelist from an experienced WRF user. When doing the latter, carefully check it option by option as some options may be very specific to his/ her simulations. Furthermore, in some cases errors in WRF namelists may remain undiscovered, even after several simulations by different users. Once you set up a namelist, use it as a starting point, test it and then make adjustments along the way.

Some options that are found to be particularly useful in this work, include topography smoothing, vertical velocity damping and exponential relaxation at the boundaries. Amongst other factors, these options allowed for stably running WRF even with a large domain. Also, it is highly recommended that you use adaptive time stepping, as most instabilities will occur in summer, when the model has to handle strong convection and vertical velocities scratch the cfl limit. If you use adaptive time stepping, the model will run fast during most of the time and then slow down in the case of strong convection.

Start with short runs and take your time to check the WRF output. In particular, check that the surface fields provided in the input move forward in time (i.e. the SST field). If this is not the case, the problem will most likely be in your namelist. The `auxinput4` switch controls the time interval of your lower boundary conditions. Make sure it is set to a reasonable time interval. If you use any tricks to make your input fit the requirements of WPS (e.g. the interpolation of soil data to different levels), you should pay extra attention to the corresponding (and directly connected) output fields of WRF, even if they are not important to your work. Start with long or (and) expensive simulations, once you are sure that your output data is not corrupted.

A.5. Postprocessing

NCAR provides a wide range of NCL functions specifically designed to handle WRF output. WRF output does not follow the CF naming convention for variable and dimension names. If you use CDO, it will try to rename the WRF output variables such that they fit the CF naming convention. Hence, if you combine CDO with NCL WRF user functions, the variables will sometimes not be identified by either CDO or NCL. You can work around this problem, by implementing an NCL function which translates WRF variable names to CF naming conventions and vice versa. Note, that the WRF community is very active and new postprocessing software (i.e. new NCL and Python functions) appears on a regular basis. So, it is worthwhile checkin the internet for new software releases every once in a while.

B. Example WPS and WRF namelists

In the following, namelists controlling WPS and WRF for the simulation NoNVertPlus are attached as an example.

B.1. WPS namelist

```
 &share
 wrf_core = 'ARW',
 max_dom = 3,
 start_date = '1970-06-01_00:00:00', '1970-06-01_00:00:00',
              '1970-06-01_00:00:00', '1970-06-01_00:00:00',
 end_date   = '1975-06-30_18:00:00', '1975-06-30_18:00:00',
              '1975-06-30_18:00:00', '1975-06-30_18:00:00',
 interval_seconds = 21600,
 io_form_geogrid = 2,
 debug_level = 1,
/

&geogrid
 parent_id         = 1,1,1
 parent_grid_ratio = 1,3,3
 i_parent_start    = 1,35,8
 j_parent_start    = 1,28,50
 e_we          = 150,121,112,
 e_sn          = 90,52,103,
 geog_data_res = 'default','2m','2m',
 dx = 0.75,
 dy = 0.75,
 map_proj =  'lat-lon',
 ref_lat   = 60.0,
 ref_lon   = -33.0,
 pole_lat  = 30.0,
 pole_lon  = 180.0,
 stand_lon = 33.0,
 geog_data_path = '/home/ubelix/climate/dr08p023/DATA/GEODATA/geog',
```

```
 opt_geogrid_tbl_path = './geogrid/',
 ref_x = 90.0,
 ref_y = 50.0,
/

&mod_levs
 press_pa = 201300 , 200100 , 100000 ,
             95000 ,  90000 ,
             85000 ,  80000 ,
             75000 ,  70000 ,
             65000 ,  60000 ,
             55000 ,  50000 ,
             45000 ,  40000 ,
             35000 ,  30000 ,
             25000 ,  20000 ,
             15000 ,  10000 ,
              5000 ,   1000
/

&ungrib
 out_format = 'WPS',
 prefix = 'FILE',
/

&metgrid
 fg_name = 'FILE',
```

B.2. WRF namelist

```
 &time_control
start_year                          = 1970,    1970,    1970,  1970,
start_month                         = 06,      06,      06,    06,
start_day                           = 01,      01,      01,    01,
start_hour                          = 00,        00,        06,      06,
start_minute                        = 00,        00,        00,      00,
start_second                        = 00,        00,        00,      00,
end_year                            = 1975,    1975,    1975,  1975,
end_month                           = 06,      06,      06,    06,
end_day                             = 30,      30,      30,    30,
end_hour                            = 18,        18,        18,      18,
end_minute                          = 00,        00,        00,      00,
```

```
end_second                  = 00,       00,       00,     00,
interval_seconds            = 21600,
input_from_file             = .true.,  .true.,   .true., .false.,
history_interval            = 360,      360,       360,    60,
frames_per_outfile          = 120,     240,     240,  1000,
restart                     = .false.,
restart_interval            = 7200,
io_form_history             = 2,
io_form_restart             = 2,
io_form_input               = 2,
io_form_boundary            = 2,
debug_level                 = 0,
io_form_auxinput4           = 2,
auxinput4_inname            = "wrflowinp_d<domain>",
auxinput4_interval          = 360,
output_diagnostics          = 1,
io_form_auxhist3            = 2,
auxhist3_interval           = 360,360,360
/

&domains
time_step                   = 360,
time_step_fract_num         = 0,
time_step_fract_den         = 1,
max_dom                     = 1,
e_we                        = 150, 121, 112,
e_sn                        = 90, 52, 103,
e_vert                      = 48, 48, 48,
p_top_requested             = 5000,
num_metgrid_levels          = 15,
num_metgrid_soil_levels     = 4,
dx                          = 83383.11, 27794.37, 27794.37,
dy                          = 83383.11, 27794.37, 27794.37,
grid_id                     = 1, 2, 3,
parent_id                   = 1, 1, 1,
i_parent_start              = 1, 35, 8,
j_parent_start              = 1, 28, 50,
parent_grid_ratio           = 1, 3, 3,
parent_time_step_ratio      = 1, 3, 3,
feedback                    = 1,
use_levels_below_ground     = .false.,
```

```
smooth_option               = 1,
lagrange_order              = 1,
smooth_cg_topo              = .true.,
eta_levels                  = 1.0, 0.9965, 0.988, 0.9765,
                              0.962, 0.944, 0.9215, 0.8945,
                              0.8610358, 0.8231076, 0.7851793,
                              0.747251, 0.6943396, 0.65,
                              0.62, 0.59, 0.56, 0.53,
                              0.50, 0.48, 0.46, 0.44, 0.42,
                              0.40, 0.38, 0.36, 0.34,
                              0.32, 0.30, 0.28, 0.26, 0.24,
                              0.22, 0.20, 0.18, 0.16, 0.14,
                              0.12, 0.10, 0.08118097, 0.06555686,
                              0.05175705, 0.03956851, 0.02880313,
                              0.01929472, 0.01089652, 0.003478885, 0.0,
/


&physics
mp_physics                  = 95, 6, 6,
ra_lw_physics               = 1, 1, 1,
ra_sw_physics               = 1, 1, 1,
radt                        = 30, 30, 30,
sf_sfclay_physics           = 1, 1, 1,
sf_surface_physics          = 2, 2, 2,
bl_pbl_physics              = 1, 1, 1,
bldt                        = 0, 0, 0,
cu_physics                  = 1, 1, 1,
cudt                        = 5, 5, 5,
isfflx                      = 1,
ifsnow                      = 1,
icloud                      = 1,
sst_update                  = 1,
surface_input_source        = 1,
num_soil_layers             = 4,
sf_urban_physics            = 0, 0, 0,
maxiens                     = 1,
maxens                      = 3,
maxens2                     = 3,
maxens3                     = 16,
ensdim                      = 144,
```

```
/

&fdda
/

&dynamics
w_damping                 = 1,
diff_opt                  = 1,
km_opt                    = 4,
diff_6th_opt              = 1,
diff_6th_factor           = 0.12,
base_temp                 = 290.,
damp_opt                  = 3,
zdamp                     = 5000.,
dampcoef                  = 0.3,
smdiv                     = 0.1,
emdiv                     = 0.01,
epssm                     = 0.3,
khdif                     = 0,
kvdif                     = 0,
non_hydrostatic           = .false.,
moist_adv_opt             = 1,
scalar_adv_opt            = 1,
/

&bdy_control
spec_bdy_width            = 5,
spec_zone                 = 1,
relax_zone                = 4,
spec_exp                  = 0.33,
specified                 = .true.,
nested                    = .false.,.true.,.true.,
/

&grib2
/

&namelist_quilt
nio_tasks_per_group       = 0,
nio_groups                = 1,
/
```

List of Figures

2.1. Blocking event as found in a simulation for late December 1977. Potential vorticity (blue and red) and geopotential height (contours) on the 500 hPa isobaric surface. The anticyclonic flow regime is eminent in both fields. After its buildup, the center of the blocking is located over the British Isles. 5

2.2. Effect of stretching and shrinking of air parcels on relative vorticity. Potential vorticity is conserved for both cases. 8

3.1. WRF ARW vertical terrain following coordinates, in WRF ARW denoted with η, more commonly known as σ-coordinates. West-east cross-section along the Greenland ice sheet with several η-levels (dashed lines) and the surface (solid line). 19

3.2. Model domains used in this study. The embedded domains are resolved three times higher than the outer domain. 27

3.3. SST average (top) and variance (bottom) extracted from ERA-Interim (left) and CESM (right) datasets. 28

4.1. Tracked anticyclone in the ERASSTtVar simulation on November 5, 1979, 12:00. The local maximum in the geopotential height field detected by the LAGTRACK-algorithm is indicated with a black cross and all grid points inside the black circle were counted as blocked at that timestep. 34

5.1. Blocking frequencies as found with the LAGTRACK index (left) and the TIMO index (right) for (top to bottom) ERA-Interim, CESM, NoN, NoNVertPlus. For both indices, the unit is percentage of blocked time steps with respect to the total number of time steps. Regions, where terrain elevation exceeds 1000 m a.s.l. are not considered in the analysis and therefore shown in grey. 38

5.2. Blocking frequencies as found with the LAGTRACK index (left) and the TIMO index (right) for (top to bottom) RockyN, BothN, CoastNtVar, ERASSTtVar. For both indices, the unit is percentage of blocked time steps with respect to the total number of time steps. Regions, where terrain elevation exceeds 1000 m a.s.l. are not considered in the analysis and therefore shown in grey. 39

5.3. Boxplots of some event properties found in NoN, RockyN, BothN, NoNVertPlus, CoastNtVar and ERASSTtVar. The box contains the 25th to 75th percentile, the lines include the 5th to 95th percentile. Values outside this range are considered as outliers and shown as crosses. Considered are only events in a restricted area between 60°W to 40°E and 30°N to 75°N. Shown are event duration (top left), largest gaussian radius (top right), maximum intensity (bottom left) and event mean latitude (bottom right). 45

5.4. Difference in average zonal low level (925 to 700 hPa) wind speed between CESM and ERA-I. The low level wind speed is determined the same way as for the histograms in figure 5.6. 47

5.5. First EOF of extended winter daily mean sea level pressure from NoN and corresponding PC score time series. 48

5.6. Histogram plot for low level (925 to 700 hPa) jet maximum as retrieved by the Woollings algorithm [*Woollings et al.*, 2010]. The unit is absolute counts in the simulation (30 years). Magnitude and position of the northern peak and tail of the ERA-Interim histogram are highlighted in green. 49

5.7. Low level (925 to 700 hPa) jet maximum histogram plots as retrieved by the Woollings algorithm for ERASSTtVar (left) and BothN (right). The unit is absolute counts in each simulation. For convenience, magnitude and position of the northern peak and tail of the ERA-Interim histogram are again highlighted in green. 50

5.8. Top: Mean states (climatologies) in geopotential height at 500 hPa and sea level pressure for ERASSTtVar(left) and NoNVertPlus (right). Bottom: Difference in climatological sea level pressure between ERASSTtVar and the unnested control run NoNVertPlus. 51

5.9. First two EOFs of monthly SLP (left and middle) of ERASSTtVar, CoastNtVar and NoNVertPlus. Time series (right) for the projection of monthly SLP to the first EOF for NoNVertPlus. For NoNVertPlus (bottom) this corresponds directly to the first PC. 54

5.10. Composites of ERASSTtVar (left) and NoNVertPlus (right). The top two panels show the composite three days after the blocking onset. The lower six panels show the deviations of the composites from their respective climatologies. In these six panels, the temporal evolution is shown from top to bottom at days seven and two prior to the blocking onset and day three after its onset. 56

5.11. Average latent heating and geopotential height (contours) calculated from ERASSTtVar (left) and NoNVertPlus (right). Geopotential height contours are given in meters. . . 58

5.12. Synoptic situation during a blocking event found in ERASSTtVar. PV distribution on the $\theta = 315$ K surface and sea level pressure. The first three panels (top left to bottom right) show part of the evolution during the onset on April 5, from 00:00 UTC to 12:00 UTC in six hour steps. In the bottom right panel, the mature event is shown 30 hours later on April 6, 18:00 UTC. 59

5.13. Left: Vertical cross-section of potential vorticity and potential temperature along 50°N on April 5, 12:00 UTC. (top right panel) reveals the heating in the upper troposphere downstream to the cyclone located south of Greenland and the lifting of the dynamical tropopause. Right: Vertical PV advection to the $\theta = 330$ K surface which coincides roughly with the dynamical tropopause at around 15°W at that instance. 60

5.14. Top four panels: Eady growth rates for ERASSTtVar, BothN, NoNVertPlus and NoN, stippling indicates regions, where the atmosphere is unstably stratified ($N^2 < 0$). Bottom four plots: Differences (ERASSTtVar - NoNVertPlus, left) and (BothN - NoN, right) at 850 hPa and 300 hPa. Stippling indicates regions, where the differences are significant on a 95% significance interval (Two-sided Mann-Whitney-U test). Note that in the top four panels, the scales for left and the right panels are different. 61

References

Altenhoff, A. M., O. Martius, M. Croci-Maspoli, C. Schwierz, and H. C. Davies, Linkage of atmospheric blocks and synoptic-scale rossby waves: a climatological analysis, *Tellus A*, *60*(5), 1053–1063, 2008.

American Meteorological Society, A., Glossary of meteorology, cited 2017: Blocking, 2017.

Bailey, D., M. Holland, E. Hunke, B. Lipscomb, B. Briegleb, C. Bitz, and J. Schramm, Community Ice CodE (CICE) user's guide version 4.0 released with CCSM 4.0, *Tech. rep.*, Los Alamos National Library, 2011.

Barriopedro, D., R. García-Herrera, A. R. Lupo, and E. Hernández, A climatology of northern hemisphere blocking, *Journal of Climate*, *19*(6), 1042–1063, 2006.

Benzi, R., A. Speranza, and A. Sutera, A minimal baroclinic model for the statistical properties of low-frequency variability, *Journal of the Atmospheric Sciences*, *43*(23), 2962–2967, 1986.

Berckmans, J., T. Woollings, M.-E. Demory, P.-L. Vidale, and M. Roberts, Atmospheric blocking in a high resolution climate model: Influences of mean state, orography and eddy forcing, *Atmospheric Science Letters*, *14*(1), 34–40, 2013.

Berrisford, P., et al., The ERA-Interim archive version 2.0, Shinfield Park, Reading, 23 pp., 2011.

Blender, R., K. Fraedrich, and F. Lunkeit, Identification of cyclone-track regimes in the North Atlantic, *Quarterly Journal of the Royal Meteorological Society*, *123*(539), 727–741, 1997.

Buehler, T., Atmospheric blocking events and extreme temperatures in climate simulations and data, Master's thesis, Climate and Environmental Physics, University of Bern, 2008.

Buehler, T., C. C. Raible, and T. F. Stocker, The relationship of winter season north atlantic blocking frequencies to extreme cold or dry spells in the era-40, *Tellus A*, *63*(2), 212–222, 2011.

Charney, J. G., and A. Eliassen, A numerical method for predicting the perturbations of the middle latitude westerlies., *Tellus*, *1*, 38–54, 1949.

Chen, F., K. Mitchell, J. Schaake, Y. Xue, H.-L. Pan, V. Koren, Q. Y. Duan, M. Ek, and A. Betts, Modeling of land surface evaporation by four schemes and comparison with FIFE observations, *Journal of Geophysical Research: Atmospheres*, *101*(D3), 7251–7268, 1996.

Christensen, C. W., and A. Wiin-Nielsen, Blocking as a wave-wave interaction, *Tellus A*, *48*(2), 254–271, 1996.

Collins, M., et al., Long-term climate change: Projections, commitments and irreversibility., in *Climate Change 2013: The Physical Science Basis. Contribution of Working Group I to the Fifth Assessment Report of the Intergovernmental Panel on Climate Change*, edited by T. Stocker, D. Qin, G.-K. Plattner, M. Tignor, S. Allen, J. Boschung, A. Nauels, Y. Xia, V. Bex, and P. Midgley, Cambridge University Press, Cambridge, United Kingdom and New York, NY, USA., 2013.

D'Andrea, F., et al., Northern hemisphere atmospheric blocking as simulated by 15 atmospheric general circulation models in the period 1979-1988, *Climate Dynamics*, *14*(6), 385–407, 1998.

Davini, P., and F. D'Andrea, Northern hemisphere atmospheric blocking representation in global climate models: Twenty years of improvements?, *Journal of Climate*, 2016.

Davini, P., C. Cagnazzo, S. Gualdi, and A. Navarra, Bidimensional diagnostics, variability, and trends of northern hemisphere blocking, *Journal of Climate*, *25*(19), 6496–6509, 2012.

Dee, D. P., et al., The ERA-Interim reanalysis: Configuration and performance of the data assimilation system, *Quarterly Journal of the Royal Meteorological Society*, *137*(656), 553–597, 2011.

Dudhia, J., Numerical study of convection observed during the winter Monsoon experiment using a mesoscale two-dimensional model, *Journal of the Atmospheric Sciences*, *46*(20), 3077–3107, 1989.

Eady, E. T., Long waves and cyclone waves, *Tellus*, *1*(3), 33–52, 1949.

Eckhardt, S., A. Stohl, H. Wernli, P. James, C. Forster, and N. Spichtinger, A 15-year climatology of warm conveyor belts, *Journal of Climate*, *17*(1), 218–237, 2004.

Egger, J., Dynamics of blocking highs, *Journal of the Atmospheric Sciences*, *35*(10), 1788–1801, 1978.

Gao, C., A. Robock, and C. Ammann, Volcanic forcing of climate over the past 1500 years: An improved ice core-based index for climate models, *Journal of Geophysical Research: Atmospheres*, *113*(D23), 2008.

Gomez, J. J., C. Raible, and S. Dierer, Sensitivity of the WRF model to PBL parametrisations and nesting techniques: evaluation of wind storms over complex terrain, *Geoscientific model development (GMD)*, *8*(10), 3349–3363, 2015.

Grazzini, Frederico, The exceptional warm anomalies of summer 2003., *ECMWF Newsletter*, *99*, 2–8, 2003.

Holton, J. R., and G. J. Hakim, *An introduction to dynamic meteorology*, vol. 88, Academic press, 2012.

Hong, S.-Y., J. Dudhia, and S.-H. Chen, A revised approach to ice microphysical processes for the bulk parameterization of clouds and precipitation, *Monthly Weather Review*, *132*(1), 103–120, 2004.

Hong, S.-Y., Y. Noh, and J. Dudhia, A new vertical diffusion package with an explicit treatment of entrainment processes, *Monthly Weather Review*, *134*(9), 2318–2341, 2006.

Huber, M., and R. Knutti, Natural variability, radiative forcing and climate response in the recent hiatus reconciled, *Nature Geoscience*, *7*(9), 651–656, 2014.

Hurrell, J. W., Y. Kushnir, G. Ottersen, and M. Visbeck, An overview of the North Atlantic Oscillation, in *Geophysical Monograph Series*, vol. 134, edited by J. W. Hurrell, Y. Kushnir, G. Ottersen, and M. Visbeck, pp. 1–35, American Geophysical Union, Washington, D. C., 2003.

Hurrell, J. W., et al., The Community Earth System Model: A framework for collaborative research, *Bulletin of the American Meteorological Society*, *94*(9), 1339–1360, 2013.

Kain, J. S., The Kain-Fritsch convective parameterization: An update, *Journal of Applied Meteorology*, *43*(1), 170–181, 2004.

Kovats, S., T. Wolf, and B. Menne, Heatwave of August 2003 in Europe: Provisional estimates of the impact on mortality, *Eurosurveillance Weekly*, *8*(11), 11, 2004.

Laprise, R., The Euler equations of motion with hydrostatic pressure as an independent variable, *Monthly Weather Review*, *120*(1), 197–207, 1992.

Largeron, Y., and C. Staquet, Persistent inversion dynamics and wintertime PM10 air pollution in Alpine valleys, *Atmospheric Environment*, *135*, 92–108, 2016.

Lawrence, D. M., et al., Parameterization improvements and functional and structural advances in version 4 of the Community Land Model, *Journal of Advances in Modeling Earth Systems*, *3*(3), 2011.

Lean, J., G. Rottman, J. Harder, and G. Kopp, Sorce contributions to new understanding of global change and solar variability, in *The Solar Radiation and Climate Experiment (SORCE)*, pp. 27–53, Springer, 2005.

Lehner, F., F. Joos, C. C. Raible, J. Mignot, A. Born, K. M. Keller, and T. F. Stocker, Climate and carbon cycle dynamics in a CESM simulation from 850 to 2100 CE, *Earth system dynamics*, *6*(2), 411–434, 2015.

Lejenäs, H., and H. Økland, Characteristics of northern hemisphere blocking as determined from a long time series of observational data, *Tellus A: Dynamic Meteorology and Oceanography*, *35*(5), 350–362, 1983.

Lindzen, R. S., and B. Farrell, A simple approximate result for the maximum growth rate of baroclinic instabilities, *Journal of the Atmospheric Sciences*, *37*(7), 1648–1654, 1980.

Luo, D., A barotropic envelope Rossby soliton model for block–eddy interaction. part I: Effect of topography, *Journal of the Atmospheric Sciences*, *62*(1), 5–21, 2005.

Masato, G., B. J. Hoskins, and T. Woollings, Winter and summer northern hemisphere blocking in CMIP5 models, *Journal of Climate*, *26*(18), 7044–7059, 2013.

Masato, G., T. Woollings, and B. J. Hoskins, Structure and impact of atmospheric blocking over the Euro-Atlantic region in present-day and future simulations, *Geophysical Research Letters*, *41*(3), 1051–1058, 2014.

Matsueda, M., R. Mizuta, and S. Kusunoki, Future change in wintertime atmospheric blocking simulated using a 20-km-mesh atmospheric global circulation model, *Journal of Geophysical Research*, *114*(D12), 2009.

Merz, N., C. C. Raible, and T. Woollings, North Atlantic eddy-driven jet in interglacial and glacial winter climates, *Journal of Climate*, *28*(10), 3977–3997, 2015.

Miller, J. E., Cyclogenesis in the Atlantic coastal region of the United States, *Journal of Meteorology*, *3*(2), 31–44, 1946.

Mlawer, E. J., S. J. Taubman, P. D. Brown, M. J. Iacono, and S. A. Clough, Radiative transfer for inhomogeneous atmospheres: RRTM, a validated correlated-k model for the longwave, *Journal of Geophysical Research: Atmospheres*, *102*(D14), 16,663–16,682, 1997.

Monin, A., and A. Obukhov, Basic laws of turbulent mixing in the surface layer of the atmosphere, *Contrib. Geophys. Inst. Acad. Sci. USSR*, *151*(163), e187, 1954.

Neale, R. B., Description of the NCAR Community Atmosphere Model (CAM 4.0), *Tech. rep.*, NCAR, 2010.

O'Reilly, C. H., S. Minobe, and A. Kuwano-Yoshida, The influence of the Gulf stream on wintertime European blocking, *Climate Dynamics*, *47*(5-6), 1545–1567, 2016.

Pelly, J. L., and B. J. Hoskins, A new perspective on blocking, *Journal of the Atmospheric Sciences*, *60*(5), 743–755, 2003.

Pfahl, S., and H. Wernli, Quantifying the relevance of atmospheric blocking for co-located temperature extremes in the northern hemisphere on (sub-)daily time scales, *Geophysical Research Letters*, *39*(12), 2012.

Pfahl, S., C. Schwierz, M. Croci-Maspoli, C. M. Grams, and H. Wernli, Importance of latent heat release in ascending air streams for atmospheric blocking, *Nature Geoscience*, *8*(8), 610–614, 2015.

Quadrelli, R., M. Lazzeri, C. Cacciamani, and S. Tibaldi, Observed winter Alpine precipitation variability and links with large-scale circulation patterns, *Climate Research*, *17*, 275–284, 2001.

Randall, D., et al., Cilmate models and their evaluation., in *Climate Change 2007: The Physical Science Basis. Contribution of Working Group I to the Fourth Assessment Report of the Intergovernmental Panel on Climate Change*, edited by S. Solomon, D. Qin, M. Manning, Z. Chen, M. Marquis, K. Averyt, M. Tignor, and H. Miller, Cambridge University Press, Cambridge, United Kingdom and New York, NY, USA, 2007.

Rex, D. F., Blocking action in the middle troposphere and its effect upon regional climate, *Tellus*, *2*(4), 275–301, 1950.

Rossby, C. G., Planetary flow patterns in the atmosphere, *Journal of the Royal Meteorological Society*, *66*, 68 –87, 1940.

Scaife, A. A., T. Woollings, J. Knight, G. Martin, and T. Hinton, Atmospheric blocking and mean biases in climate models, *Journal of Climate*, *23*(23), 6143–6152, 2010.

Scaife, A. A., D. Copsey, C. Gordon, C. Harris, T. Hinton, S. Keeley, A. O'Neill, M. Roberts, and K. Williams, Improved atlantic winter blocking in a climate model, *Geophysical Research Letters*, *38*(23), 2011.

Schemann, V., B. Stevens, V. Grützun, and J. Quaas, Scale dependency of total water variance and its implication for cloud parameterizations, *Journal of the Atmospheric Sciences*, *70*(11), 3615–3630, 2013.

Scherrer, S. C., M. Croci-Maspoli, C. Schwierz, and C. Appenzeller, Two-dimensional indices of atmospheric blocking and their statistical relationship with winter climate patterns in the Euro-Atlantic region, *International Journal of Climatology*, *26*(2), 233–249, 2006.

Schlesinger, M. E., and N. Ramankutty, An oscillation in the global climate system of period 65 - 70 years, *Nature*, *367*(6465), 723–726, 1994.

Schmidt, G. A., et al., Climate forcing reconstructions for use in pmip simulations of the last millennium (v1. 0), *Geoscientific Model Development*, *4*(1), pp33–45, 2011.

Schoenberg Ferrier, B., A double-moment multiple-phase four-class bulk ice scheme. Part I: Description, *Journal of the Atmospheric Sciences*, *51*(2), 249–280, 1994.

Schraff, C., and R. Hess, A description of the nonhydrostatic regional COSMO-model, part III: Data assimilation, *Tech. rep.*, Consortium for Small Scale Modelling, 2012.

Schwierz, C., M. Croci-Maspoli, and H. Davies, Perspicacious indicators of atmospheric blocking, *Geophysical research letters*, *31*(6), 2004.

Skamarock, W., J. Klemp, J. Dudhia, D. Gill, D. Barker, M. Dudha, X. Huang, W. Wang, and Y. Powers, A description of the advanced research WRF version 30. NCAR technical note, *Tech. rep.*, NCAR/TN-475, 2008.

Smith, R., et al., The parallel ocean program (POP) reference manual, *Los Alamos National Lab Technical Report*, *141*, 2010.

Staniforth, A., Regional modeling: A theoretical discussion, *Meteorology and Atmospheric Physics*, *63*(1), 15–29, 1997.

Tibaldi, S., and F. Molteni, On the operational predictability of blocking, *Tellus A*, *42*(3), 343–365, 1990.

Trenberth, K., et al., Observations: Surface and atmospheric climate change., in *Climate Change 2007: The Physical Science Basis. Contribution of Working Group I to the Fourth Assessment Report of the Intergovernmental Panel on Climate Change*, edited by S. Solomon, D. Qin, M. Manning, Z. Chen, M. Marquis, K. Averyt, M. Tignor, and H. Miller, Cambridge University Press, Cambridge, United Kingdom and New York, NY, USA, 2007.

Vardoulakis, S., and P. Kassomenos, Sources and factors affecting PM10 levels in two European cities: Implications for local air quality management, *Atmospheric Environment*, *42*(17), 3949–3963, 2008.

Vieira, L. E. A., and S. K. Solanki, Evolution of the solar magnetic flux on time scales of years to millenia, *Astronomy & Astrophysics*, *509*, A100, 2010.

Waller, J. A., S. L. Dance, A. S. Lawless, N. K. Nichols, and J. R. Eyre, Representativity error for temperature and humidity using the Met Office high-resolution model: Representativity error for the Met Office model, *Quarterly Journal of the Royal Meteorological Society*, *140*(681), 1189–1197, 2014.

Walter, K., U. Luksch, and K. Fraedrich, A response climatology of idealized midlatitude thermal forcing experiments with and without a storm track, *Journal of Climate*, *14*(4), 467–484, 2001.

Wan, H., et al., The ICON-1.2 hydrostatic atmospheric dynamical core on triangular grids - Part 1: Formulation and performance of the baseline version, *Geoscientific Model Development*, *6*(3), 735–763, 2013.

Wang, L., et al., The impact of cold spells on mortality and effect modification by cold spell characteristics, *Scientific Reports*, *6*(1), 2016.

Weijenborg, C., H. de Vries, and R. J. Haarsma, On the direction of Rossby wave breaking in blocking, *Climate Dynamics*, *39*(12), 2823–2831, 2012.

Wiedenmann, J. M., A. R. Lupo, I. I. Mokhov, and E. A. Tikhonova, The climatology of blocking anticyclones for the northern and southern hemispheres: Block intensity as a diagnostic, *Journal of Climate*, *15*(23), 3459–3473, 2002.

Wilks, D. S., *Statistical methods in the atmospheric sciences*, no. v. 100 in International Geophysics Series, 3rd ed., Elsevier/Academic Press, Amsterdam, Boston, 2011.

Woollings, T., A. Hannachi, and B. Hoskins, Variability of the North Atlantic eddy-driven jet stream, *Quarterly Journal of the Royal Meteorological Society*, *136*(649), 856–868, 2010.

Wu, L., and B. Wang, A potential vorticity tendency diagnostic approach for tropical cyclone motion, *Monthly Weather Review*, *128*(6), 1899–1911, 2000.

Acknowledgements

First and foremost I thank Christoph Raible for his supervision and especially for his constructive criticism and the time and energy he invested in discussing both technical and stylistic aspects of this thesis. Thanks to Juan José Goméz Navarro for his Co-supervision and especially for helping me to set up the experiments.

Special thanks to Martina Messmer for her support with technical issues and also for the moralistic support of despairing master students in office B16. Thanks to the regional modeling crew Pato, Cevahir and Deniza and my former office mates Michu and Sandro for all the discussions on and off topic. It has been a wonderful time at CEP and I can sincerely say that I will miss this institute and its members. I will not forget all the Pizza days, spontaneous Bouldering sessions and FABs.

I am grateful that I always had and still have the full support of my parents Veronika and Peter. Thank you to my roommates Aurich, Ellen, Mohammed and Beju for not being to strict with the housekeeping duties during the last weeks of my thesis and to Basho for occasionally dropping into my office with chocolate and drinks, when I was working overtime. Nicole you always encourage me to keep my head up and look forward!

Declaration

under Art. 28 Para. 2 RSL 05

Last, first name: Regenass, Daniel

Matriculation number: 08-066-763

Programme: MSc in Climate Sciences
with a special qualification in Atmospheric Science

Bachelor ☐ Master ☒ Dissertation ☐

Thesis title: Investigating atmospheric blocking in a series of downscaling experiments with the regional climate model WRF ARW

Thesis supervisor: Prof. Dr. Christoph C. Raible

I hereby declare that this submission is my own work and that, to the best of my knowledge and belief, it contains no material previously published or written by another person, except where due acknowledgement has been made in the text. In accordance with academic rules and ethical conduct, I have fully cited and referenced all material and results that are not original to this work. I am well aware of the fact that, on the basis of Article 36 Paragraph 1 Letter o of the University Law of 5 September 1996, the Senate is entitled to deny the title awarded on the basis of this work if proven otherwise. I grant inspection of my thesis.

Bern, June 6, 2017

Signature

D. Regen